



# Investigation of Contact Pressure Distribution on Sheet Metal Stamping Tooling Interfaces: Surface Modeling, Simulations, and Experiments

Item Type	thesis
Authors	Sah, Sripati
DOI	<a href="https://doi.org/10.7275/355648">10.7275/355648</a>
Download date	2024-11-27 07:15:59
Link to Item	<a href="https://hdl.handle.net/20.500.14394/47523">https://hdl.handle.net/20.500.14394/47523</a>

INVESTIGATION OF CONTACT PRESSURE DISTRIBUTION ON SHEET  
METAL STAMPING TOOLING INTERFACES:  
SURFACE MODELING, SIMULATIONS, AND EXPERIMENTS

A Thesis Presented  
by

SRIPATI SAH

Submitted to the Graduate School of the  
University of Massachusetts Amherst in partial fulfillment  
of the requirements for the degree of

MASTER OF SCIENCE IN MECHANICAL ENGINEERING

September 2007

Mechanical Engineering

© Copyright by Sripati Sah 2007  
All Rights Reserved

INVESTIGATION OF CONTACT PRESSURE DISTRIBUTION ON SHEET  
METAL STAMPING TOOLING INTERFACES:  
SURFACE MODELING, SIMULATIONS, AND EXPERIMENTS

A Thesis Presented

by

SRIPATI SAH

Approved as to style and content by:

---

Robert X. Gao, Chair

---

Ian Grosse, Member

---

Rui Wang, Member

---

Mario Rotea, Department Head  
Department of Mechanical and Industrial Engineering

## ACKNOWLEDGMENTS

I would like to express my sincere gratitude to Professor Robert Gao, for his guidance and support during the course of my M.S. study at the University of Massachusetts, Amherst. His drive for scientific rigor and perfection in all aspects of research has been a great source of inspiration for me. It is his deep understanding of the nature of the technical challenges that has enabled me to focus on what was essential and critical towards the successful completion of my M.S. degree study. With his help, I have not only improved my research capabilities, but also my way of thinking and communicating. I believe the training I have received under his direction will greatly benefit my future career.

I would also like to thank Professor Ian Grosse, Professor Rui Wang, and Professor Jian Cao (Northwestern University) for serving on my thesis committee and providing valuable feedback on my research work.

I am grateful to my colleagues Tristan Boscardin and Dr. Ruqiang Yan for their discussion and friendship. I would also like to extend my gratitude to my other colleagues at the Electromechanical Systems Laboratory, for their kindness and cooperation as a wonderful team. Special thanks to Oliver Pabst (Technical University of Berlin) and Eduardo Pinto (Umass Amherst) for help in collecting experimental data and to Alan Rakouskas and Rick Winn in fabricating and running the stamping test bed.

Finally I would like to gratefully acknowledge funding provided to this research by the National Science Foundation under grant DMI-0620957.

## ABSTRACT

# INVESTIGATION OF CONTACT PRESSURE DISTRIBUTION ON SHEET METAL STAMPING TOOLING INTERFACES: SURFACE MODELING, SIMULATIONS, AND EXPERIMENTS

SEPTEMBER 2007

SRIPATI SAH

B. Tech. ME, INSTITUTE OF TECHNOLOGY, BANARAS HINDU UNIVERSITY,  
INDIA  
M.S. ME, UNIVERSITY OF MASSACHUSETTS AMHERST

Directed by:  
Professor Robert X. Gao

In stamping operations, sheet metal is formed into a desired shape by pressing it in a hydraulic or mechanical press between suitably shaped dies. As a predominant manufacturing process, sheet metal forming has been widely used for the production of automobiles, aircraft, home appliances, beverage cans and many other industrial and commercial products.

A major effort till date on stamping processes monitoring has been focused on investigating variations in the press force. Given that the press force itself is an integral of the contact pressure distribution over the die and binder contact interfaces, it is conceivable that defects may be better identified by analyzing the contact pressure distribution directly at the tooling-workpiece interface, instead of measuring the press

force, which is less reflective of the localized forming process due to its nature as a secondary effect. It is thus desirable that a new, integrated sensing method capable of directly assimilating forming pressure distribution in the tooling structure be devised for improved stamping process monitoring. Designing such a distributed sensing scheme and analyzing the feasibility of its structural integration into a stamping tooling structure is the objective of this reported work. In this context, four research tasks have been identified and examined during the course of this work:

1) Devising a New, Embedded Sensing Method

The new sensing method monitors stamping processes by means of an array of force sensors structurally integrated into the stamping tooling. The ability to directly measure local forming events by means of such an integrated and distributed sensing provides a new means of performing defect detection and process monitoring. Such a distributed sensing system overcomes the limitations of traditional tonnage and acceleration sensing systems which are focused on the measurement of indirect, global parameters. The new method is based on the evaluation of spatially continuous pressure surfaces from spatially discrete sensor measurements that are directly related to the local events at the stamping interface. To evaluate the effectiveness of this method, a panel stamping test bed equipped with an array of embedded force sensors has been designed, modeled and fabricated. Data obtained from experiments conducted on the test bed indicates that the new sensing method can be highly effective in process monitoring of stamping operations.

## **2) Reconstruction of Spatio-Temporal Distribution of Contact Pressure**

Structurally integrating sensors under tooling surfaces reduces the surface rigidity of the tool, thus limiting the number of sensors and the locations at which they can be embedded. This in turn affects the reconstruction of contact pressure distribution on the tooling surface. Numeric surface generation methods, such as Bezier surfaces and Thin Plate Spline surfaces offer a method for estimating the contact pressure distributions on the tooling surfaces from a sparse distribution of sensors.

The concept of interpolating force distributions using surfaces has been investigated by researchers previously. However, selection of the surface generation method has remained largely an *ad hoc* process. The work presented here addresses this issue by using tooling interface contact pressure distribution information obtained from FE simulations as the basis for evaluating the accuracy of two commonly employed surface methods mentioned above. In order to reach a generic conclusion, the mathematical background of these schemes has been examined in light of the purpose at hand. The results indicate that an interpolative scheme such as the Thin Plate Spline surfaces (TPS), which can estimate the contact pressure distributions more accurately in a multi-sensor environment. The local and global accuracies of the Thin Plate Spline surface modeling technique have been experimentally evaluated using a sensor embedded stamping test bed designed for the purpose.

## **3) Modeling of Contact Pressure Distribution at the Sheet Metal-Tooling Interface**

Information about the contact pressure distribution at the tooling interface is critical to identifying the accuracy of numeric schemes that estimate by interpolation or

approximation the contact pressure at any point on the tooling surface, based on a limited number of spatially distributed sensors. Furthermore, such knowledge is valuable in identifying operational parameters for the sensors to be integrated into the stamping tooling structure. In the absence of a tractable analytic method of determining the contact pressure distribution on stamping tooling surfaces, Finite Element models of a stamping operation have been created. Furthermore the drilling of sensor cavities under the working surfaces of the dies adversely affects the working life of stamping dies and their strength. The accuracy of analytic fatigue failure mechanics in evaluating the effect of parameters, such as embedding depth and sensor rigidity, on the operational life of the die, suffers from uncertainty in the estimation of stress concentrations around sharp geometric features of the sensor cavity. This shortcoming has been circumvented by the creation of FE models of the sensor cavity for more accurate estimation of stress concentrations around sharp geometries. The effect of different embedding materials on the sensitivity of embedded sensors has also been evaluated based on these models.

#### 4) Defect Detection in Stamping Operation

The ultimate goal of this thesis research was to study the feasibility of identifying defects in a stamping process based on the contact pressure distribution surfaces. This was achieved in this reported work by spatio-temporal decomposition of ‘parameters’ derived from the contact pressure distribution surfaces. Here ‘parameters’ refers to quantities such as the minimum, maximum, and mean contact pressures. These parameters have a time-varying spatial location as well as magnitude value associated

with them. The feasibility of defect detection in stamping operations based on such parameters has been investigated.

In addition to these focal areas, the design and implementation of a stamping test bed equipped for distributed contact pressure sensing has also been researched. This test bed was utilized for experimental verification of the developed theories and numerical models. Design of the proposed test bed required research into additional topics like the design of a protective package for embedded sensors and the effect of sensor embedding depth on contact pressure measurements. These issues have been addressed in this work, culminating in the experimental demonstration of the embedded pressure sensing system for process monitoring in the sheet metal stamping processes.

## TABLE OF CONTENTS

<b>ACKNOWLEDGMENTS .....</b>	<b>iv</b>
<b>ABSTRACT .....</b>	<b>v</b>
<b>LIST OF TABLES .....</b>	<b>xii</b>
<b>LIST OF FIGURES .....</b>	<b>xiii</b>
<b>CHAPTER</b>	
<b>1 INTRODUCTION.....</b>	<b>1</b>
1.1 Background on Stamping Process .....	1
1.2 Present Stage of Knowledge .....	3
1.2.1 Sensing Techniques for Stamping .....	3
1.2.2 Embedded Sensing.....	6
1.2.3 Spatio-Temporal Contact Pressure Reconstruction .....	11
1.3 Motivation for Embedded Contact Pressure Sensing .....	13
<b>2 MODELLING OF CONTACT PRESSURE DISTRIBUTION .....</b>	<b>15</b>
2.1 Models, Element Selection & Materials .....	15
2.2 Kinematic Constraints & Application of Loads.....	19
2.3 Two Dimensional Simulation Results .....	20
2.4 Three Dimensional Simulation Results .....	25
<b>3 SPATIO-TEMPORAL CONTACT PRESSURE RECONSTRUCTION.....</b>	<b>28</b>
3.1 Snake Skeleton Graphs .....	28
3.1.1 Approximation Based on Bezier Curves.....	29
3.1.2 Approximation Based on 3D Bezier Surfaces .....	32
3.2 Sensor Surface Map .....	35
3.2.1 Interpolation Based on Cubic Splines.....	35
3.2.2 Interpolation Based on Thin Plate Spline .....	39
3.3 Contact Pressure Estimation in SSG and SSM Methods .....	40
3.3.1 Approach.....	40

3.3.2	2D Bezier Approximations vs. Cubic Interpolations.....	40
3.3.3	Bezier Surfaces vs. Thin Plate Splines .....	41
<b>4 EXPERIMENTAL EVALUATION.....</b>	<b>43</b>	
4.1	Sensing Package.....	43
4.1.1	Sensing Element.....	43
4.1.2	Sensing Package Designs.....	44
4.1.3	Sensing Package Prototypes .....	47
4.2	Effect of Embedding Depth on Sensitivity .....	48
4.3	Experiments on a Contact pressure Sensor Array.....	52
4.4	Stamping Test Bed.....	55
4.4.1	Experimental Setup.....	55
4.4.2	Contact Pressure Surfaces - Normal Process .....	57
4.4.3	Accuracy of Contact Pressure Estimation.....	62
4.4.4	Contact Pressure Surfaces - Corner Failure .....	66
<b>5 MODELING OF WORKING STRESSES IN DIES .....</b>	<b>70</b>	
5.1	Impact of Embedding Sensors on Die Tool Failure.....	70
5.1.1	Finite Element Model of Sensor Cavity .....	70
5.1.2	Analysis of Stress Distribution in Die Cavity.....	72
5.1.3	Effect of Rigidity of Sensing Element.....	74
5.1.4	Fatigue Life Analysis of Sensor Cavity.....	76
5.2	Effect of Die Material on Embedded Sensor Measurements .....	80
<b>6 CONCLUSION .....</b>	<b>81</b>	
6.1	Summary .....	81
6.2	Intellectual Contribution .....	84
6.3	Future Work .....	86
6.3.1	Sensor Package .....	86
6.3.2	Self Energized Wireless Sensing .....	87
6.3.3	Computational Efficiency of Surface Generation Methods.....	88
6.3.4	Structured Defect Detection.....	88
<b>APPENDIX: ELEMENT FORMULATION .....</b>	<b>89</b>	
<b>BIBLIOGRAPHY .....</b>	<b>94</b>	

## LIST OF TABLES

Table	Page
2.1 Material properties used in simulation.....	17
3.1 Control points used in generating Bezier surface .....	34
4.1 Mesh element sizes for Finite Element model (mm) .....	46
4.2 Correlation between applied load and sensor measurement.....	51
4.3 Test bed materials and properties .....	56
5.1 Material properties used in sensor cavity simulation.....	72
5.2 Safety factor for different surface loads and embedding depths.....	76
5.3 Life expectancy (Number of product stamped) .....	79

## LIST OF FIGURES

Figure		Page
1.1	Stamping setup.....	1
1.2	Sensor placement .....	4
1.3	Segments of a tonnage signal.....	4
1.4	Accelerometer signal .....	4
1.5	Use of proximity sensors in detecting uneven closure.....	5
1.6	A stamping product and its thermal image .....	6
1.7	Ceramic rod.....	7
1.8	Shear normal gauge.....	7
1.9	Die shoulder force transducer .....	8
1.10	Measurements of pulling force .....	8
1.11	Static load test & results .....	9
1.12	Moving Load Test & Results.....	10
1.13	Embedded sensing setup for upset forging .....	10
1.14	Snake Skeleton Graph.....	12
2.1	Model components .....	15
2.2	Mesh details and model constraints .....	16
2.3	Punch & binder trajectories .....	19
2.4	von Mises stress (PSI) distribution at different time instants .....	21
2.5	Plastic strain intensity in workpiece at different time instants .....	23
2.6	Contact pressure at T=0.25 secs.....	24
2.7	Temporal variation of contact pressure .....	24
2.8	Contact pressure distribution on punch at different time instants.....	26
2.9	Contact pressure on working interface .....	27
3.1	Control polygon & Bezier curve.....	32
3.2	3 <sup>rd</sup> order Bernstein functions.....	32
3.3	Example of Bezier surface, control points and polygon net .....	34
3.4	Four point blending functions for Cubic spline .....	39
3.5	Bezier contact pressure approximation .....	41
3.6	Cubic interpolation of contact pressure .....	41
3.7	SSG approximated contact pressure .....	42

3.8	SSM interpolated contact pressure.....	42
3.9	Estimated maximum contact pressure and FE reference value .....	42
4.1	FlexiForce sensor.....	43
4.2	Calibration of sensing element.....	44
4.3	Exploded view of first sensing package.....	45
4.4	Top and front in-situ view of first package.....	45
4.5	Finite element model and pressure distribution on sensing area .....	46
4.6	In-situ view of second sensor package.....	47
4.7	Sensor package prototypes .....	47
4.8	Sensor embedding components.....	48
4.9	Quasi-static loading results .....	49
4.10	Ramp loading by 14mm cylinder.....	50
4.11	Impulse loading by 14mm cylinder .....	51
4.12	Experimental setup.....	53
4.13	TPS estimated contact pressure (Normal Case).....	53
4.14	Measured vs. integrated force .....	54
4.15	TPS estimated contact pressure (Defect Case) .....	54
4.16	CAD drawing of test bed and sensor installation.....	56
4.17	Experimental test bed, sensor positions, and driver circuit .....	57
4.18	Sensor measurements from binder and within die cavity .....	58
4.19	Contact pressure surfaces for sensors within die cavity and on binder ....	59
4.20	Pressure extreme within die cavity and point of action (POA) chart .....	61
4.21	Contact pressure extreme on binder and point of action (POA) chart.....	61
4.22	Comparison of TPS contact pressure estimate with measurement .....	62
4.23	Contact pressure estimate calculated with and without extra sensors .....	63
4.24	Comparison of TPS contact pressure estimates with measurements .....	64
4.25	Integrated punch and binder forces.....	65
4.26	Comparison of press force with net surface integrated force .....	66
4.27	Image of panel with corner defect .....	67
4.28	Contact pressure surfaces for sensors within die cavity and on binder ....	68
4.29	Contact pressure extremes on binder and point of action (POA) chart ....	69
4.30	Pressure extremes on die cavity and point of action (POA) chart .....	69
5.1	Model of sensor installation and FE mesh.....	71

5.2	Maximum von Mises stress in 2mm deep die cavity .....	73
5.3	Maximum von Mises stress in 4mm deep die cavity .....	74
5.4	Maximum von Mises stress in 2mm deep die cavity .....	75
5.5	Maximum von Mises stress in 4mm deep die cavity .....	76
5.6	Simulated sensor measurements .....	80
5.7	Concept sketch for hemispherical top cap .....	86

# CHAPTER 1

## INTRODUCTION

### 1.1 Background on Stamping Process

The physical setup of a sheet metal stamping operation consists of three main components: the die, the binder, and the punch [1, 2] (Figure 1.1). The setup is mounted on a hydraulic or mechanical press with a force rating estimated from the size, material and shape of the desired product. During a stamping operation, the periphery of the sheet metal workpiece is held between the binder and die flange. The contact force between the binder and workpiece is referred to as the binder force. As the punch moves down, the workpiece is pressed into the die, causing plastic deformation in the workpiece material. During the operation the flow of workpiece material into the die is regulated by the binder force [3-5].

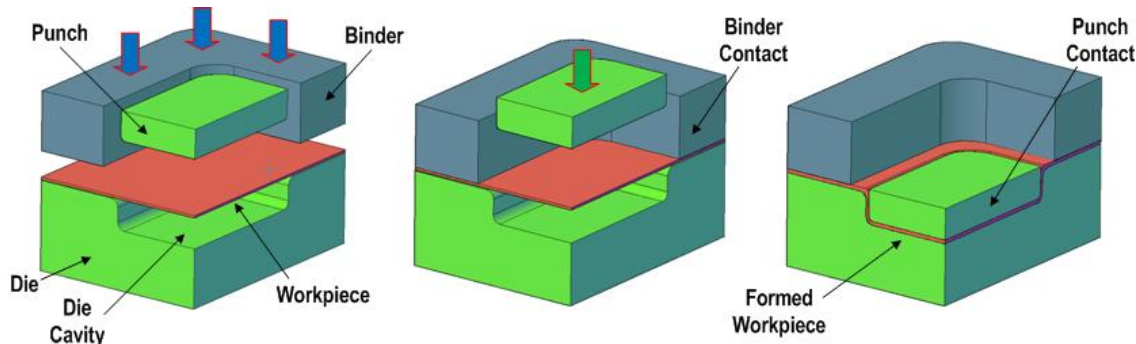


Figure 1.1 - Stamping setup

There are a large number of operational conditions that in parts affect and can help characterize the stamping process [6]. These include, e.g., die surface condition, binder contact pressure distribution, slide parallelism, shut height variation, punch contact pressure distribution, workpiece draw-in, etc. Variations in these conditions could lead to changes in the quality of the stamped product. Some of these parameters, such as

slide parallelism and binder contact pressure distribution, may change with each stamping cycle while other parameters, such as die surface condition, may change only gradually. These parameters also interact with each other, introducing a compounding effect on the process. For example, an increase in binder contact pressure distribution restricts the flow of workpiece material into the die, causing an increase in the required punching force. However such relations are in most cases unquantifiable. Due to the large number of operating parameters, their inherent nature and the difficulty of measuring them, it is not feasible to measure all the parameters individually, and their combined significance with respect to process outcome (product quality) is a matter of conjecture. Thus production defects like wrinkling, tearing and dimensional variation in product geometry are not uncommon in stamping [7]. Due to such conditions designing a reliable process monitoring system for stamping operations has been a subject of continuing investigation.

## **1.2 Present Stage of Knowledge**

In general a process monitoring system includes three main phases of operation: in the first phase sensors collect information from the physical process by direct measurement, in the second phase the recorded measurements undergo low level signal processing like noise filtering and signal amplification this produces useful information out of the raw data. Finally, decision making models which make judgments about the process status, act on this information. The following sections review the state of art research in these subject areas.

### **1.2.1 Sensing Techniques for Stamping**

Tonnage sensing is the most common technique for monitoring stamping processes [8, 9]. Estimation of the operational press force by measurement of strain ( $\epsilon = \Delta l/l$ ) induced in the structure of the stamping press is referred to as tonnage sensing. Strain sensors are generally mounted at points of the press frame (Figure 1.2) where the strain is highest this is generally on support columns of the press and binder columns. The strain signal is segmented corresponding to different forming actions of the press (Figure 1.3).

The utility of tonnage sensing is limited because it considers press strain, which is a cumulative effect of all the forces acting in the machine setup. Hence, tonnage sensing can not detect, or spatially localize, small localized disturbances in the sheet forming process. The sensitivity of press mounted strain gauges to forming events also suffers because of the distance of the sensing site from the actual site where the deformation action is taking place. As the forming forces pass through the die, die base and work table, there is a considerable amount of structural damping, causing the loss of high

frequency components of the measurement. Thus press strain provides an incomplete representation of the actual forming action.

At high operating speeds, presses exhibit dynamic effects such as changes in shut height and slide parallelism under influence of stamping speed, press tonnage and other operational conditions [10]. As these changes are not directly correlated with the tonnage, the effectiveness of tonnage based process monitoring system for high speed stamping is limited.

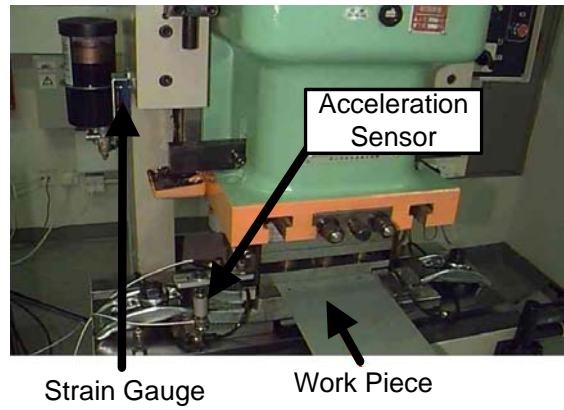


Figure 1.2 – Sensor placement [10]

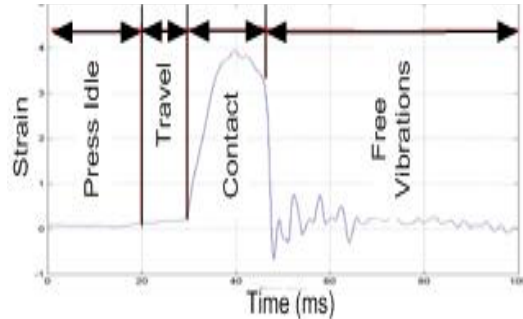


Figure 1.3 – Segments of tonnage signal [10]

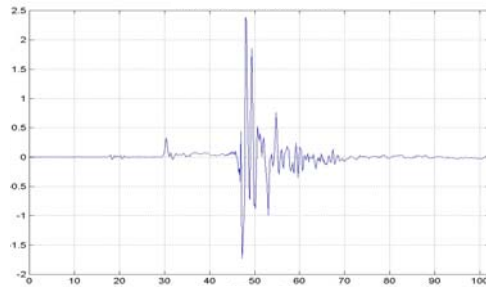


Figure 1.4 – Accelerometer signal [11]

Vibration measurements have also been researched for process monitoring in stamping operations [11]. This technique is based on measuring vibrations in stamping dies by acceleration sensors placed on the edges or backside of the tooling die. Vibration signals require noise filters, because of their inherently high noise

susceptibility. It has certain advantages over tonnage sensing, like the ability to detect slugs and variations in workpiece thickness. However, vibration sensing not unlike tonnage based techniques, by basic design is incapable of spatially localizing disturbances in sheet metal forming. In addition there is no information feedback from vibration sensing that could aid in improvement of die designs or FE process models.

It is noted that in addition to measuring the tonnage, some stamping machines are equipped with proximity sensors to measure the die closure gap. An uneven or larger than normal die closure gap is indicative of the presence of slugs within the die. Figure 1.5 shows how the presence of slugs affects die closure in small to medium sized dies. As the presence of slugs induces large localized forces, it is possible that the proposed embedded contact pressure sensor based process monitoring system will be capable of detecting slugs however this is conditional to the presence of an embedded contact pressure sensor in the vicinity of the slug.

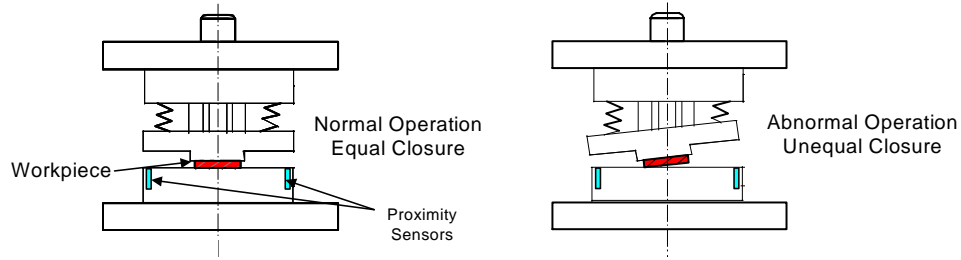


Figure 1.5 – Use of proximity sensors for detecting uneven closure [10]

Recently efforts have been made to detect defects in stamping products using image processing [12]. These techniques utilize either visible spectrum images or infrared images. Figure 1.6 shows a small stamped product and the thermal distribution on its surface as it exits the die. The occurrence of high temperature (hot spots) regions on the surface of a workpiece is connected to higher friction in the region this is attributed to the localized action of normal forces larger than the design value. It is supported that

such systems can be used for defect detection in the stamping process. However, vision based systems require elaborate setups and staging areas which are not practical for high volume industrial production purposes.

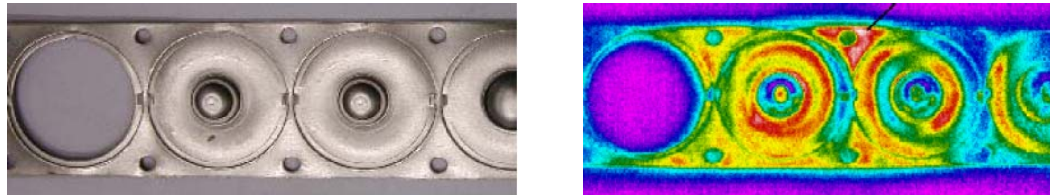


Figure 1.6 – A stamped product and its thermal image [12]

### 1.2.2 Embedded Sensing

Two sensing devices for measuring shear and normal tool forces in sheet metal forming operations are known to have been developed [13]. In the first device, the surface of a ceramic rod 25 mm in diameter was embedded with sensors (piezoelectric disks) 1.5 mm in diameter and 1 mm thick (Figure 1.7). The piezo disks were sensitive to loads parallel to their circular faces. A strip of metal was pulled across the surface of the ceramic rod and the frictional forces measured. It was found that in most experiments the sensor output was unstable even for constant pulling force. It was concluded that direct measurement of surface friction through small piezo-electric shear force sensors is impractical due to the difficulties in sensor element fixation. The second device (SN Gauge) consisted of a series of five adjacent wedges comprising part of a cylindrical surface (Figure 1.8). Each wedge was connected to the cylinder through piezoelectric disks. The geometry of the wedge and disk arrangement was such that the sensors measured only normal loads. Trigonometric considerations allow for the calculation of tangential frictional forces from the normal force measurements. The frictional force measurements from this device matched well with the theoretically estimated values.

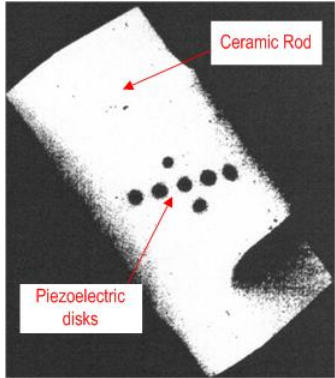


Figure 1.7 – Ceramic rod [13]

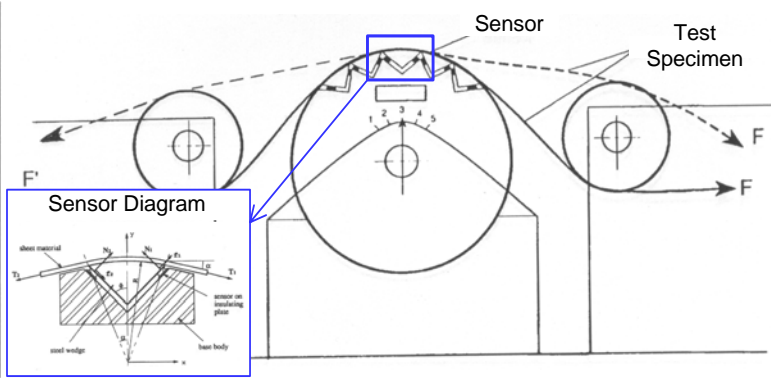


Figure 1.8 – Shear normal gauge [13]

This work is significant to the present thesis because its findings indicate that placing sensors flush with tool surfaces leads to unreliable measurement conditions, as well as substantial wearing of the sensors. Another contribution of this work is the analytic method used for calculating the frictional forces from normal force measurements. This method can be used to find friction conditions in a stamping die.

A transducer design for stamping operations intended for measuring tension in the sheet metal workpiece was reported [14]. The transducer is installed on the die shoulder between the punch and binder it consists of a roller over which the workpiece passes. The roller is mounted on steel webbings to which strain gauges have been attached (Figure 1.9). During the stamping operation the sheet metal workpiece gets pulled over the transducer roller, inducing deformation in the webbings which is measured by the strain gauges. The tension in the sheet metal is then calculated from the strain measurements. Experiments were conducted in which the punch and binder forces were calculated from the tension measurements. It was found that the pulling force (sheet tension) determined by the transducer was in good agreement with measurements made with an externally attached reference sensor. The ratio of the two values, which should ideally be one, is shown in Figure 1.10a. The effect of varying draw bead height on the

required pulling force was also studied through experiments. Figure 1.10b shows the variation of pulling force as function of the draw bead position. The significance of this work is that it represents the initial efforts in embedding sensors within a stamping die, the findings of this study act as a helpful guide.

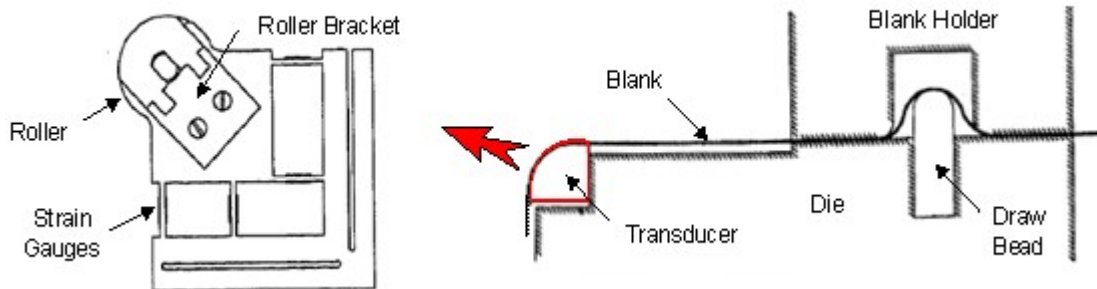
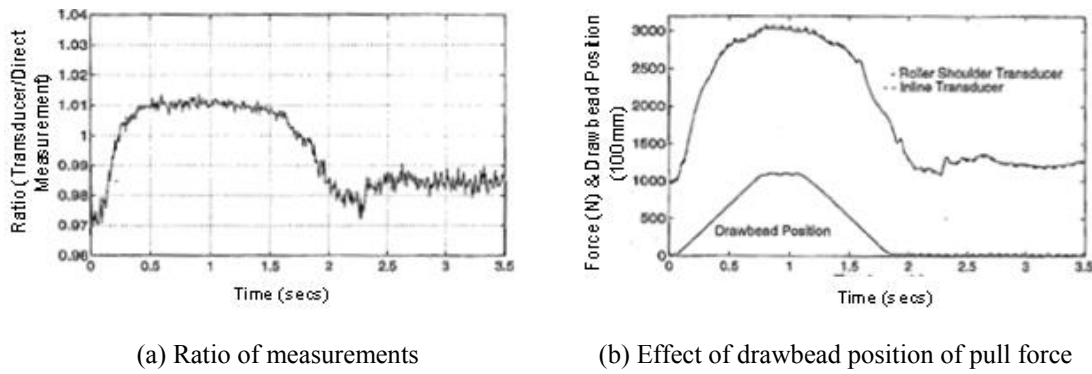


Figure 1.9 – Die shoulder force transducer [14]



(a) Ratio of measurements

(b) Effect of drawbead position of pull force

Figure 1.10– Measurements of pulling force [14]

One of the reported works, directly related to the present research is on the use of embedded piezoelectric force sensors for measuring interface forces [15]. In this work the response of piezo-electric force sensors embedded below a test surface to static and moving loads was experimentally studied. Cylindrical Lead-Zirconate-Titanate (PZT) piezoelectric sensors with a diameter of 3 mm and 2 mm thick were cast into a ceramic filled epoxy test bed Figure 1.11a. The study reports that sensors embedded at smaller depth (less than 1 mm) have a highly linear response to loads applied normally to the

embedding surface, whereas sensors at larger depths have a comparatively less linear response. From the point of view of signal processing, a linear response is desirable as it reduces the computational effort required for signal processing. The sensors were also demonstrated to be sensitive to the spatial location of the sensor with respect to the point at which load is applied Figure 1.11b.

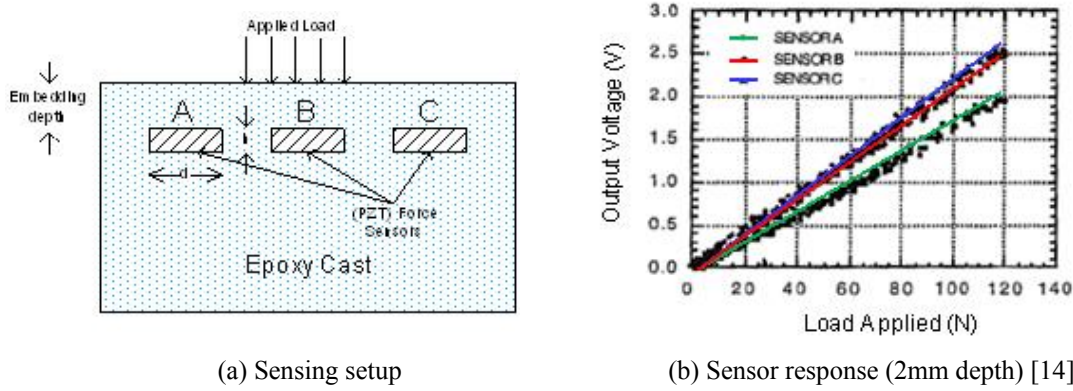
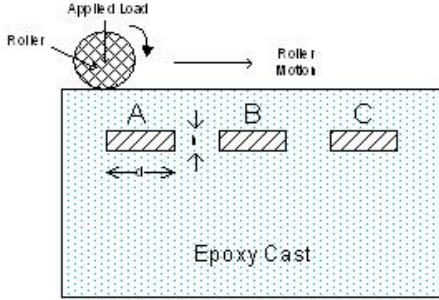
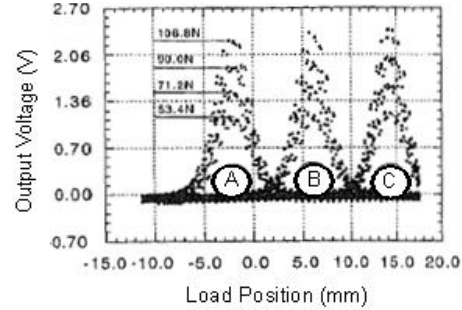


Figure 1.11 – Static load test & results

To study the response of the embedded sensors to moving loads a second experimental setup (Figure 1.12a) was used. In this setup a roller was rolled at a constant speed over the sensor embedded surface, the sensor measurements show (Figure 1.12b) high spatial resolution, indicating the possibility of detecting localized process variations in a stamping operation. The findings of this work are useful for determining the spatial arrangement for a embedded contact pressure sensor array to be designed for process monitoring in stamping operations. The work used FE models in order to simulate the embedding depth effects however there was an amount of disagreement in the experimental and simulated results. With improvement in FEM techniques in the intervening period it is expected that more accurate FE models can be developed for such sensor systems now.



(a) Sensing setup

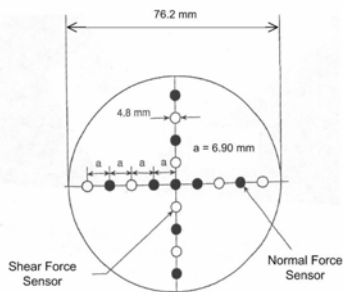


(b) Sensor response (2mm depth) [14]

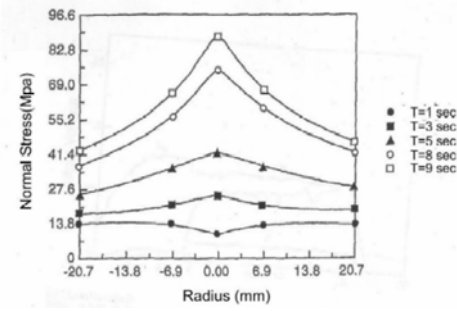
Figure 1.12 – Moving load test & results

The measurement of interface stresses in upset forging has also been attempted [16].

A ceramic flat face upset die 76.2 mm in diameter and 20 mm thick was constructed with normal and shear force sensors set on its surface. The sensors were cylindrical Lead-Zirconate-Titanate (PZT) elements with a diameter of 4.8 mm. These sensors were embedded in a “plus” shaped configuration under the working surface of the die (Figure 1.13a). In experiments conducted the die was used to compress various metals and non metals at varying rates of deformation. Installing sensors on working surfaces of a stamping die will lead to rapid wear and undesirable changes in product quality, but trends in contact surface contact pressures reported in this work (Figure 1.13b) are useful for identifying optimum sensor locations in the present work.



(a) Sensor array



(b) Time variation of stress distribution

Figure 1.3 – Embedded sensing setup for upset forging [16]

Stamping operations are generally performed in hostile working environment. In such an environment connecting cables to and from sensors would be in high risk of

being damaged. An ideal sensing technique for stamping process would have wireless, self powered sensors. A wireless sensing system exists for measuring cavity contact pressure in the injection molding process [17]. It consists of wireless, self powered piezo-electric contact pressure sensors embedded in the mold. Sensors communicate with a receiver set on the outer surface of the mold by means of ultrasonic sound waves. The system uses inverse piezo-electric effect to make a piezo-electric crystal generate ultrasonic sound waves. Application of this principle in a process monitoring system for stamping operations would require extending the system to measure a force signal which is not necessarily monotonous in nature. Furthermore the affect of the physical structure of the die and binder on the behavior of ultrasonic waves will also need to be studied.

### **1.2.3 Spatio-Temporal Contact Pressure Reconstruction**

Embedding sensors under tooling surfaces reduces the surface rigidity of the tool and may cause deterioration of product quality. This limits the number of sensors and the locations at which they can be embedded. Therefore it is required that the contact pressure distribution on the tooling surface be reconstructed from a limited number of spatially distributed sensors. A straight forward method of estimating contact pressure distribution on the workpiece-die interface is by a time indexed series of 3D surfaces, each surface representing the contact pressure distribution on the workpiece-die interface at a particular time instant. Such a method called the Snake Skeleton Graph was proposed recently [18]. The skeleton graph consists of a number of force distribution profiles each representing the spatial force distributions over the workpiece at different instances of time. The force distribution at a time instant is represented by a

3D surface generated by the Bezier surface generation scheme. Subsequently, the center of gravities of surfaces at consecutive time instances is connected, producing a diagram that is called the skeleton graph. The process is illustrated in Figure 1.14. In addition the work presents a defect detection approach based on visual inspection of the XZ, YZ projections of the Snake Skeleton Graph. The fundamental approach of the surface estimation method used in this work is very interesting from the point of view developing contact pressure estimates from an embedded contact pressure sensor array and will be examined in detail in this thesis.

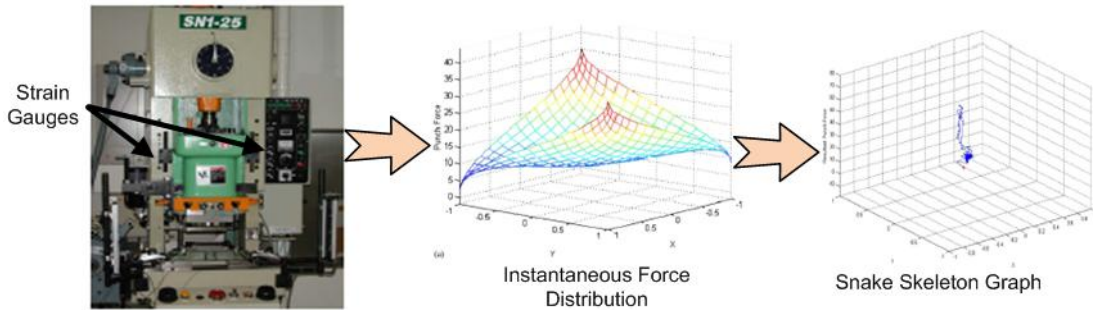


Figure 1.14 - Snake Skeleton Graph [18]

### **1.3 Motivation for Current Research**

The effectiveness of prevalent sensing techniques for stamping process monitoring is limited by their inherent spatial insensitivity. The dependence on spatially aggregated parameters (press force or vibration) makes these techniques insensitive to localized forming events. It is thus desirable that a new sensing technique capable of assimilating localized forming information in the tooling structure (e.g. stamping die) be introduced for improved process monitoring. It is known that most stamping process defects affect the spatio-temporal contact pressure distribution on the workpiece-tooling interface. Conceivably, these effects may be identified by analyzing information gathered by a contact pressure sensing array embedded within the tooling structure. Designing such a distributed sensing scheme and analyzing the feasibility of its structural integration into a stamping tooling structure is the motivation for this work, and the ultimate goal of this work is to improve the observability and diagnosability of the stamping operation through integrated sensing.

Barring variations in material/geometric properties of the workpiece, consistency in the product quality is solely dependent on the repeatability of the contact interaction. As long as there is no variation in the nature of the contact interaction (between the tooling and the workpiece) the product quality will be consistent. However, the contact interactions in the stamping process are inherently dependent on a number of parameters such as die parallelism, consistency of surface lubrication, shut height variation, and variations in workpiece thickness to name just a few. Some of these parameters are difficult if not impossible to control. Variations in the contact interaction are hence inevitable, leading to deviations in product quality and undesirable economic repercussions. Theoretically the contact interaction between a workpiece and tooling

surface can be classified as being perpendicular to surface (contact pressure) or along the surface (frictional). In a stamping process these effects are distributed over a 3D space which is the surface of the workpiece-die contact area. In addition these effects are also dynamic in nature. This seems to indicate that most abnormal variations in a stamping operation, such as die misalignment, flange wrinkling, punch over/under travel, or deviations in slide parallelism will in some manner affect the dynamic contact pressure distribution on the workpiece-die interface.

The review of the available literature indicates that, though the issue of embedding force/contact pressure sensors under working surfaces is well researched, there are important topics which still need attention. For instance, increase of the sensor embedding depth increases the spatial sensing range at the same time decreasing the spatial resolution of the measurement, as well as attenuating the physical measurement. In addition the spatially and temporally rich data from arrays of such sensors requires special processing techniques. Preliminary investigations into the SSG method indicate that the convex hull property and smoothing characteristics of the Bezier mathematics introduce significant differences in the estimated contact pressure value from the actual distribution.

To extend the state-of-knowledge in these fields, and to investigate the feasibility of process monitoring for stamping process using embedded contact pressure sensing this thesis will investigate the topics of embedded contact pressure sensing, surface generation methods, and defect detection on the basis of finite element models and experiments simulating the stamping process.

## CHAPTER 2

### MODELING OF FORMING CONTACT PRESSURE DISTRIBUTION

#### 2.1 Models, Element Selection & Materials

In order to evaluate the suitability of the different surface schemes in interpolating the contact pressure distribution across the workpiece-tooling interface, it is essential to initially develop a model of the expected temporal and spatial forming contact pressure distribution. Given the complexity of the transient plasticity problem involved in the stamping process a numerical approach has been taken to assist in the calculation of the contact pressure. For this purpose a segment of a stamping die was simulated using the finite element (FE) software package ANSYS/LSDYNA. The study was done using the explicit dynamics FEA package because the short event period and the high impulsive forces involved are best modeled using explicit time integration. The tooling components under consideration include: the die, punch, binder, and the workpiece. Both 2D and 3D analysis were carried out. The 2D and 3D models of the stamping setup are shown in Figure 2.1.

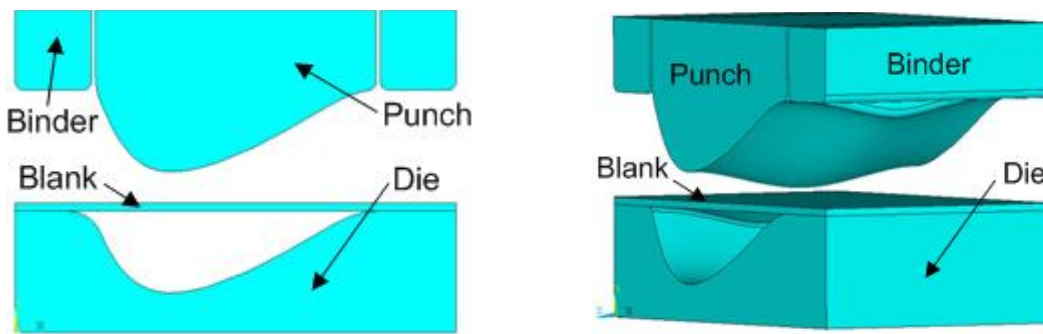


Figure 2.1- Model components

The profile of the punch and the die in the 2D model is a 7 point B-Spline. The profile was chosen to be unsymmetrical in order to evaluate the contact pressure

distribution in relation to the die surface curvature. In addition, sharp edges and corners were avoided as these need to be meshed with small element sizes and increase the computation time significantly. The 3D model is an extrusion of the 2D profile along a 5 point B-Spline path. The extrusion is symmetric about the central plane. The 2D and 3D models were generated using parameterized code which enabled easy modification of geometry by manipulating of geometric parameters. The 3D die base is 7"x11", the punch base is 7"x7", and the surface area of each binder is 2"x 7". The maximum depth of curvature for the die and punch is 3".

The 2D model utilized planar element meshing. A 4 node planar element was used. It has 6 DOF at each node: translations, velocities and accelerations in the nodal X and Y directions. The 3D model was meshed using Belytschko-Lin-Tsay shell elements with the Belytschko-Wong-Chiang improvement for warpage consideration (Figure 2.2). This particular element formulation has been chosen because of it requires much less computational time as compared to other shell element formulations with equivalent results. The element has 4 nodes with 12 DOF at each node. These are translations, accelerations, and velocities in nodal X, Y and Z directions and rotations. The details of the element formulation are provided in Appendix – A.

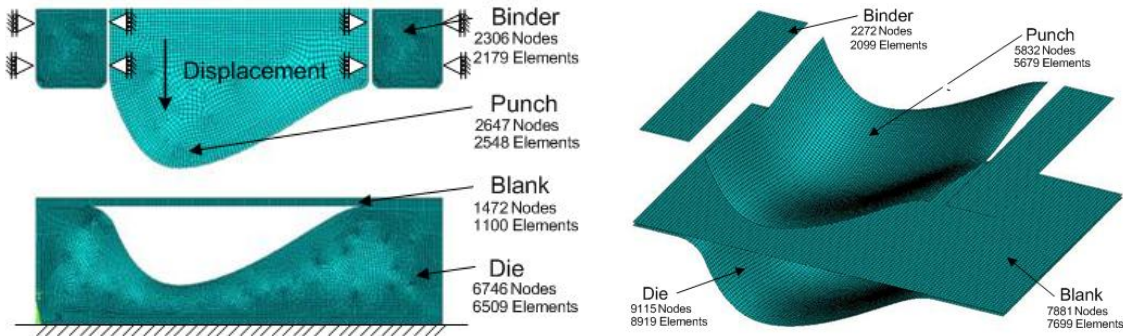


Figure 2.2 - Mesh details and model constraints

The punch and die materials have been chosen to be linear elastic isotropic materials. This choice was made because the amount of plastic deformation in forming surfaces is negligible. The workpiece material on the other hand undergoes plastic deformation. The workpiece material has been hence modeled to be bi-linear elastic-plastic and isotropic. This material model uses two slopes to represent elastic and plastic stress-strain behavior of a model. The workpiece material model is strain rate and temperature independent. The die, punch and binders have the physical properties of steel. The workpiece is 0.1" thick Aluminum AA1000. The choice of material properties was based on commonly used materials in the sheet metal stamping industry. The coefficient of friction (static & dynamic) between all the materials is taken to be 0.15. The material properties used are listed in Table 1.

Table 2.1. Material properties used in simulation

<b>Material</b>	<b>Density (lb/in<sup>3</sup>)</b>	<b>Poisson's Ratio</b>	<b>Elastic Modulus (PSI)</b>	<b>Yield Strength (PSI)</b>
<b>AA1000</b>	0.098	0.33	$1.1 \times 10^7$	15230
<b>Steel</b>	0.28	0.27	$2.9 \times 10^7$	-

Contact interactions of the die, punch, and binder with the workpiece are simulated on the basis of a stiffness relationship. This relationship is implemented in the FE package by applying a resisting force on any node of a body that penetrates the surface of another body. This resisting force is calculated as:

$$F = k \cdot \delta \quad (2.1)$$

Here, F is the resisting force,  $\delta$  is the amount of penetration and k is the contact stiffness defined for shell elements as:

$$k = \frac{f_s \times A \times K}{D_m} \quad (2.2)$$

Here,  $f_s$  is the user defined penalty factor,  $A$  is the area of contact segment,  $K$  is the bulk modulus of the contacted element and  $D_m$  is the minimum diagonal of the shell element. It is realized that the nature of the contact relationship is highly dependent on the value of this parameter. If this value is chosen to be too small the resisting force is too small and the bodies end up penetrating each other before the resisting force becomes large enough to oppose their motion. For this work a value of 0.08 was used. In the future, experimental measurement of contact pressure by the sensing scheme under study will provide a physical basis for the selection of the penalty factor.

## 2.2 Kinematic Constraints & Application of Loads

In order to closely replicate actual boundary conditions no explicitly defined constraints were applied to the workpiece. The punch and the binders only had vertical freedom all other degrees of freedom were restricted. All displacement freedoms of the die were restricted.

Two possible options for applying loads were investigated. In the first option a sinusoidal force-time history load was applied to the punch. It was found that this kind of loading led to unrealistic stresses in the components. The reason for this is that different workpiece geometries have characteristically different variation of stamping force with time which can not be substituted with another press force type without affecting the accuracy of the results. The second option was to apply a displacement vs. time trajectory to the punch. A sinusoidal displacement against time mapping was applied to the punch and binders. These mappings are typical for double action toggle joint presses [1]. The displacement history for the binder and punch motion is shown in Figure 2.3. At the lowest approach both the punch and the binders are at a predetermined distance from the die similar to the workpiece holder gap (BHG) referred to in some works [19]. The duration of the process is 0.5 seconds. The binder is in contact with the workpiece for approximately 0.3 seconds, the punch for 0.1 seconds. The punch and the binder have a 22% and 60% dwell times respectively.

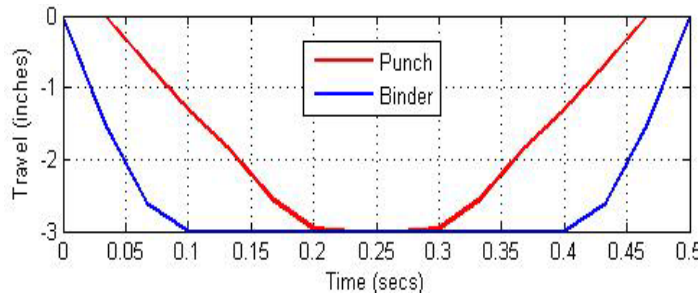


Figure 2.3 - Punch & binder trajectories

### 2.3 Two Dimensional Simulation Results

Examination of the von Mises stress distribution within the punch and die is a convenient starting point for analyzing the dynamic stress distributions in the process. Figure 2.4 shows the von Mises stress distribution in the setup at different time instants. The von Mises is non directional and only gives a qualitative idea of what the contact pressure measurements at any point would be. It is seen that the stress distributions within the die and the punch are quite small (less than 3 PSI) until the punch begins to dwell at around  $T=0.22$  secs. During this period the workpiece has already undergone significant plastic deformation (Figure 2.5). Therefore it is no surprise that the von Mises stress within the workpiece is already well beyond the yield stress.

At  $T=0.22$  sec large stress concentration develop on the right side die-workpiece contact surface. This is the first point where the gap between the punch and die surfaces becomes equal to the local workpiece thickness in the lateral direction. The possibility that the location of first contact might be affected by mesh coarseness was eliminated by successive mesh refinements. It is noted that at  $T=0.27$  when the punch starts returning the stress in the region is the last to decrease. The punch surface is an exact offset of the die surface with an offset 1.2 times the workpiece thickness [1, 2] hence the point of first contact is determined by the local workpiece thickness. In an actual stamping operation the point of first contact will be determined by the consistency of workpiece thickness and the over all product geometry. Variations in the alignment of the die/punch will be likely to affect the region of first contact. This can be utilized to ascertain proper die/punch alignment. After  $T= 0.21$  secs the region of first contact grows rapidly and high stresses develop over most of the die surface.

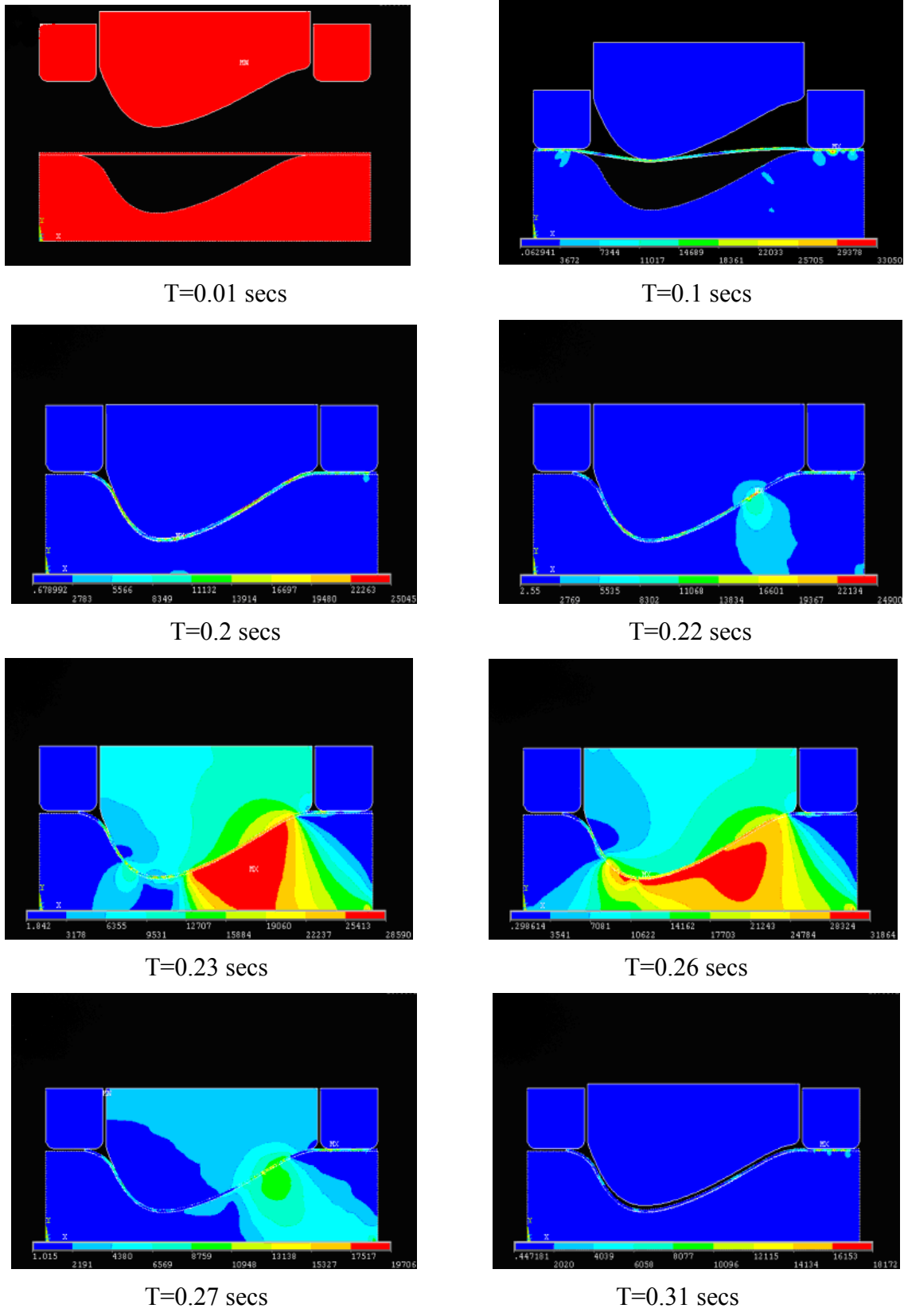


Figure 2.4 - von Mises stress (PSI) distribution at different time instants

Between times  $T=0.23$  secs and  $T=0.26$  secs the punch is dwelling and the stress state is stable. The working contact pressure during this period is closely associated with the prediction of wrinkle formation and workpiece thinning. Wrinkles can form in different modes depending on the normal contact pressure [20]. The sensors need only be installed in regions in which wrinkles are expected e.g. flanges and side walls [21]. The formation of wrinkles and the accompanying contact pressure patterns are a topic for future research. In Figure 2.5 it is noted that the plastic strain state in the workpiece attains its final state at around  $T=0.24$  secs and there is no further plastic deformation of the workpiece in the process.

Though von Mises stress is a useful overall indicator of the process state it is not possible to measure it directly by use of sensors. Embedded contact pressure sensors will measure the contact pressure on the working surfaces. Thus it is of interest to study the normal working contact pressure between the punch and workpiece at different instants during the stamping process. For this purpose the 2D model was meshed with element sizes varying from  $0.5''$  to  $0.0625''$  in steps of half and the stress results on the punch surface used to determine the normal contact pressure on the punch-workpiece boundary. In Figure 2.6 the contact pressure on the punch surface at the instant when the punch is at the lowest point of its trajectory (corresponding to  $T=0.25$  secs) for different element sizes is superposed on the punch profile. It is observed that the evaluated contact pressure distributions are very similar to each other for element sizes smaller than  $0.25''$ . The results from  $0.0125''$  and  $0.0625''$  meshes are consistent to within 10% of the  $0.0625''$  mesh results. i.e. the contact pressure solution is numerically converged.

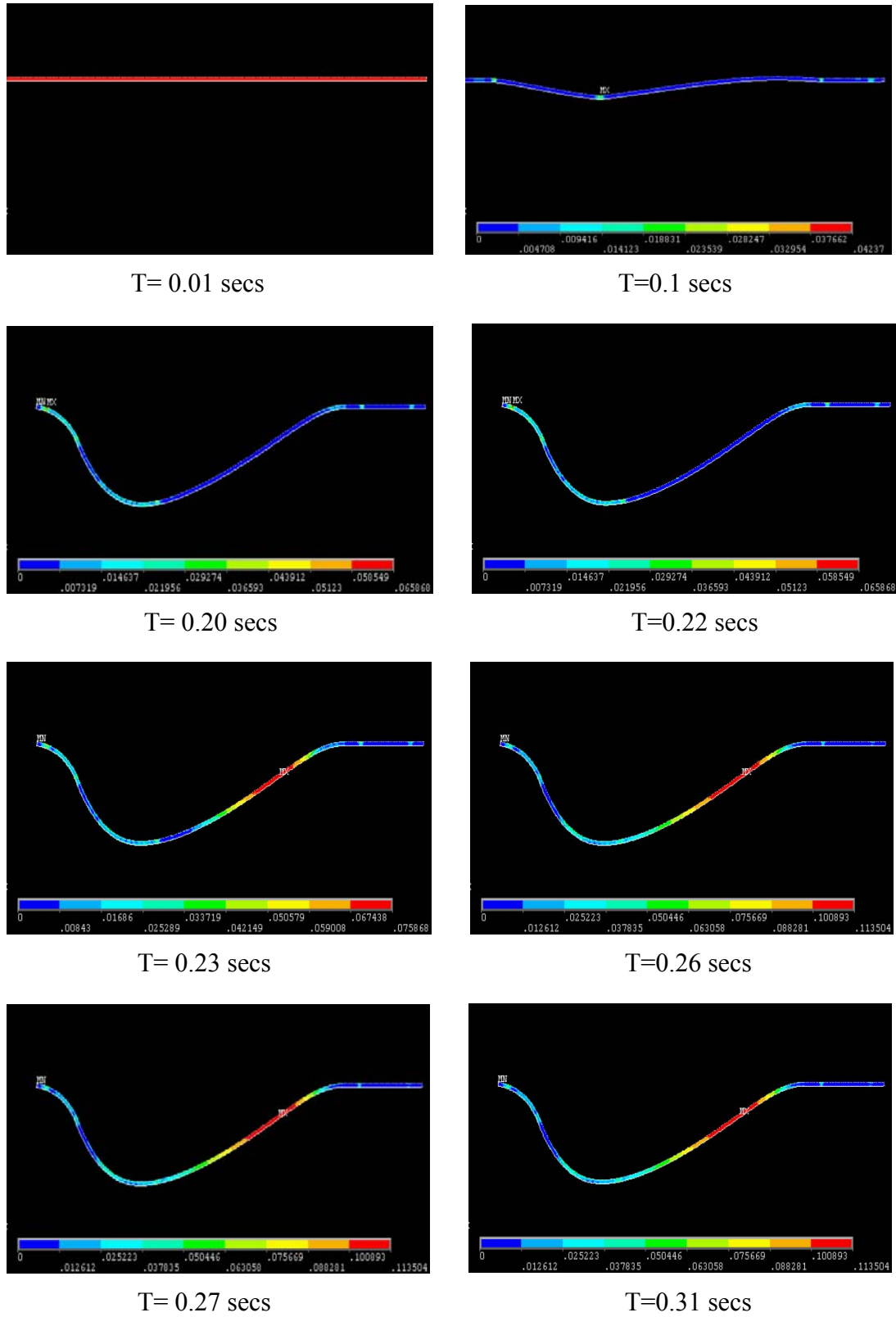


Figure 2.5 - Plastic strain intensity in workpiece at different time instants

It is thought that most manufacturing defects such as wrinkling and tearing come into existence just before the punch reaches its lower limit. The contact pressure distribution during this period is thus of prime interest. Figure 2.7 shows the normal contact pressure distribution on the punch at different time instants. The three time instants represented in the figure are  $T= 0.23, 0.25$  and  $0.27$  sec.

At  $T=0.09$  sec the punch makes initial contact with the workpiece. Due to the geometry of the model the initial contact is at the tip of the punch. As the sheet is not supported on the under side by the die, the localized stresses around the point of contact are very small as compared to the later stages of the process. At  $T=0.23$  sec the bottom side of the sheet comes in contact with the die, as seen from the von Mises stress analysis and the region of maximum contact pressure is towards the right side of the punch. There is also a small region of high working contact pressures at the punch tip. At  $T=0.25$  sec the punch starts its return stroke, at this instant the working contact pressures are the largest. During  $T=0.25$  sec to  $0.50$  sec the punch and the binders retreat to their original positions and the energy stored in the workpiece and the die as strain is released.

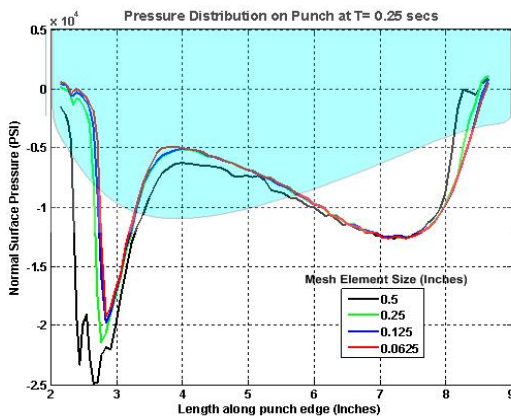


Figure 2.6 - Contact pressure at  $T=0.25$  secs

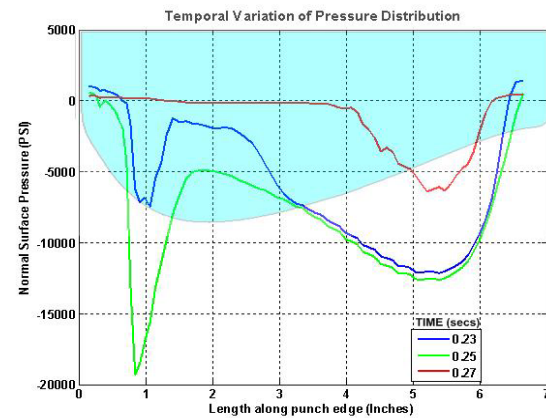


Figure 2.7 - Temporal variation of pressure

## 2.4 Three Dimensional Simulation Results

The normal stresses on the punch surface for the 3D model are shown in Figure 2.8. Since the contact model does not account for adhesive forces between surfaces the positive stresses are due to the internal mechanics of the punch. Physically positive stresses (Red) indicate regions where the punch loses contact with the workpiece. At  $T=0.01$  secs the stress distribution is shown superposed over the punch outline, as there is no contact between the punch and workpiece, there is no contact pressure. At  $T=0.1$  secs the punch comes into contact with the workpiece and small stresses develop all over the punch surface. As the punch proceeds downwards large contact pressures develop at the punch tip. At  $T=0.22$  secs the punch is at its bottom dead center and the whole surface is under compressive contact pressure. The exceptions are the three points where the contact pressure is positive, this could be due to numerical errors or possibly the punch loses contact with the workpiece due to local geometric affects. Between  $T=0.23$  secs and  $T=0.27$  secs the contact pressure distribution is steady. It is believed that reduction in the magnitude or duration of this dwell period can lead to spring back in the workpiece material.

Evaluation of the FE results leads to the conclusion that the manner in which contact pressure distribution changes over time is unique to each stamping product and can be utilized to identify process defects. For example, deviations in die/punch alignment can be detected by observing the pattern of contact pressure distribution. A misalignment would make the punch contact the workpiece unevenly leading to uneven loading on the punch surface. Deviations in shut height would lead to variations in the magnitude of the contact pressure causing spring back and workpiece thinning.

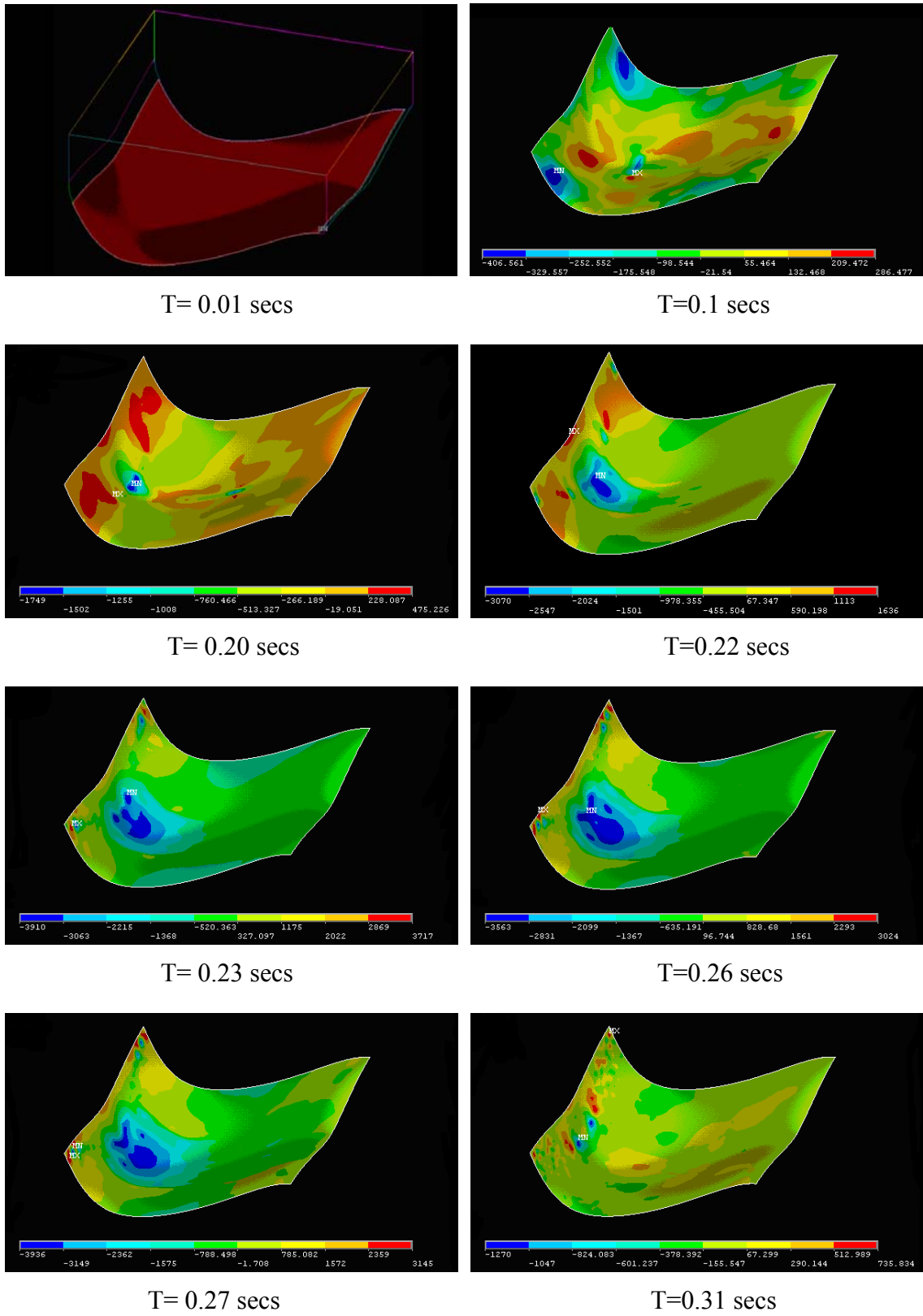


Figure 2.8 - Contact pressure distribution on punch at different time instants

In Figure 2.8 the contact pressure distribution had been plotted as contours over the curved punch surface. The objective of the FE simulations was the calculation of contact pressure estimations using numeric surface generation schemes, the nature of the surface generation schemes requires the contact pressure information to be expressed in the terms of two dimensional coordinates. Towards this purpose the contact pressure information was mapped into 2D coordinates, the reformatted representation at three instants ( $T=0.09$ ,  $0.21$ , and  $0.25$  sec) is shown left to right in Figure 2.9.

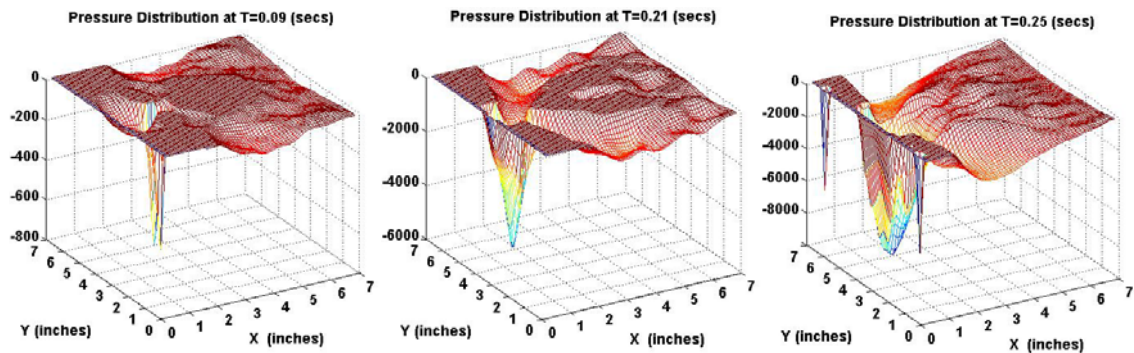


Figure 2.9 - Contact pressure on working interface

In Chapter 3 the contact pressure information obtained from the finite element analysis is used to evaluate the accuracy of interpolation/approximation based numeric surface generation schemes.

## CHAPTER 3

### SPATIO-TEMPORAL CONTACT PRESSURE RECONSTRUCTION

Embedding sensors under tooling surfaces reduces the surface rigidity of the tool and may cause deterioration of product quality. This limits the number of sensors and the locations at which they can be embedded. Hence it is required that the contact pressure distribution on the tooling surface be reconstructed from a limited number of spatially distributed sensors by using surface generation methods. The concept of interpolating contact pressure or force distributions using surface mathematics has been investigated by other researchers previously. However, selection of the surface generation method has remained largely an *ad hoc* process. In this section the tooling interface contact pressure distribution information obtained from the FE simulations is used as the basis for evaluating the Snake Skeleton Graph method [18] and the Sensor Surface Map method.

#### 3.1 Snake Skeleton Graphs

The Snake Skeleton Graph method evaluates contact pressure distribution over a surface at selected instants by using Bezier surfaces. The mathematics of Bezier curves and surfaces is a well researched topic [22, 23]. Bezier is a mathematical tool developed in the 1970's to produce curves which appear smooth at any level of viewing. Mathematically the Bezier curves are a unique case of cubic Hermite interpolation. As opposed to Hermite polynomials which are based on the derivatives at endpoints, Bezier curves are based on Bernstein polynomials, in which the interpolating polynomials depend only on a set of control points. The mathematical basis for Bezier curves is

extended to create Bezier surfaces which have similar properties. Bezier surfaces are widely used in CAD/CAM packages for generating aesthetically appealing surfaces. Consequently a large number of products designed or manufactured by CAD/CAM packages have Bezier generated surfaces, e.g. aircraft fuselages, marine hulls, and automobile body panels.

### 3.1.1 Approximation Based on Bezier Curves

A Bezier curve is defined in terms of the parameter,  $t$  in the following form [24, 25]:

$$\vec{P}(t) = \sum_{i=0}^n \vec{B}_i J_{n,i}(t) \quad (0 \leq t \leq 1) \quad (3.1)$$

Here,  $\vec{P}(t)$  is the position vector of the Bezier curve in terms of  $t$  and  $n$  is the order of the Bernstein basis function  $J_{n,i}(t)$ , which is defined as:

$$J_{n,i}(t) = \binom{n}{i} t^i (1-t)^{n-i} \quad (3.2)$$

The symbol  $\vec{B}_i$  is the position vector corresponding to the  $i^{\text{th}}$  control point from which the curve is evaluated. The degree of the defining Bernstein basis is always one less than the number of control points. For faster computation and programming purposes, the defining equations are expressed in matrix form. The defining equation for Bezier curves expressed in matrix form is:

$$\vec{P}(t) = [F] [\vec{G}] \quad (3.3)$$

Here  $[F]$  is a scalar function of parameter  $t$  comprising of Bernstein basis functions and is independent of the control points:

$$[F] = [J_{n,0} \ J_{n,1} \ J_{n,1} \ J_{n,2} \ \dots \ J_{n,n}] \quad (3.4)$$

Each element of  $[\vec{G}]$  is a position vector of a control point from which the Bezier curve is evaluated.

$$[\vec{G}]^T = [\vec{B}_0 \ \vec{B}_1 \ \vec{B}_2 \ \dots \ \vec{B}_n] \quad (3.5)$$

In order to highlight the properties of Bezier curves, an example of a four point (third order) Bezier curve is shown with its control points in Figure 3.1. The line joining the control points is referred to as the defining polygon. The control points used for the example are:

$$B_0 = (0.00, 0.10) \quad B_1 = (0.05, 0.16) \quad B_2 = (0.45, 0.12) \quad B_3 = (0.50, 0.10)$$

It is of interest to note the following in Figure 3.1:

1. The first and last points of the Bezier approximation curve are *always* coincident with the first and last points on the defining polynomial. This is because the Bernstein functions (Figure 3.2) corresponding to the first and last point ( $t=0$  and  $t=1$  in Eqn. 3.1) have the following constraints:

$$\begin{aligned} J_{3,0}(0) &= 1 & \& \quad J_{3,1}(0) = J_{3,2}(0) = J_{3,3}(0) = 0 \\ J_{3,3}(1) &= 1 & \& \quad J_{3,1}(1) = J_{3,2}(1) = J_{3,0}(1) = 0 \end{aligned} \quad (3.6)$$

2. Tangent vectors at the curve's end points are the same as for the end points of the defining polynomial. This implies that if there is a need to approximate data outside the defining polygon the approximation will just be a linear extension of the defining polygons outer most segments. This property is of practical importance because contact pressure sensors can not be placed on the edges of the working surfaces of a stamping die.

3. The curve is *always* contained within the convex hull of the defining polynomial.

This can introduce underestimations errors when attempting to generate a Bezier approximation with few control points. If on the other hand, there are a large number of control points the estimation error will be smaller. This property is attributed to the division-of-unity property of Bernstein functions stated as [26]:

$$\sum_{i=0}^n J_{n,i}(t) = 1 \quad (3.7)$$

4. The curve shown in Figure 3.1 was generated by evaluating for 50 different values of  $t$ . Bezier curves can be evaluated at any number of desired points. A thousand points on the Bezier curve could be found by simply evaluating Eqn. 3.1 at a thousand values of  $t$ .
5. Another property of Bezier curves is of weak local control. Weak local control refers to the fact that if one of the control points ( $B_i$ ) is changed then the Bezier curve is maximally affected in the region of the curve near  $t = i/n$ . Even though the entire Bezier curve is affected, the magnitude of change diminishes as the parameter  $t$  moves away from this value. This phenomena is attributed to the fact that each Bernstein basis function has a maxima at  $t = i/n$  and its value diminishes to zero as the value of  $t$  increases or decreases from this value.. Figure 3.2 shows the third order Bernstein function ( $n=3$ ). It can be seen that each Bernstein function  $B_i$  has a single maxima at  $t = i/n$ .

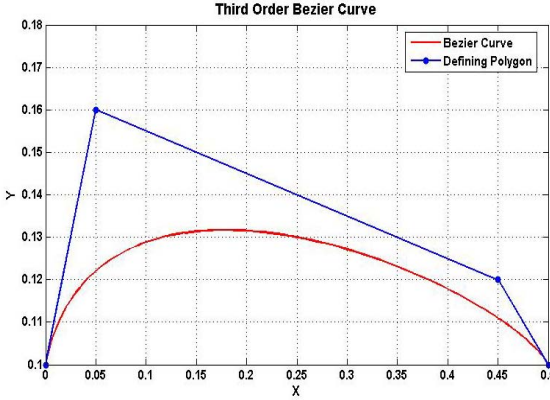


Figure 3.1 – Control polygon & Bezier curve

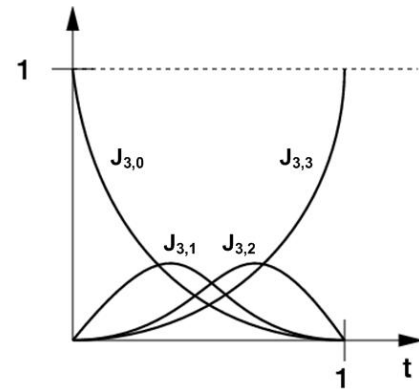


Figure 3.2 – 3<sup>rd</sup> order Bernstein functions

### 3.1.2 Approximation Based on 3D Bezier Surfaces

After examining the Bezier curves the next step is to look at the mathematical background of the Bezier surfaces and its fundamental properties. A Bezier surface is defined in the terms of two orthogonal parametric directions in the following form [24, 25]:

$$\vec{P}(u, w) = \sum_{i=0}^n \sum_{j=0}^m \vec{B}_{i,j} J_{n,i}(u) K_{m,j}(w) \quad (0 \leq u, w \leq 1) \quad (3.8)$$

Here  $u$  and  $w$  are the parametric directions which define the Bezier surface,  $n$  and  $m$  are constants that are one less than the number of control points in the  $u$  and  $w$  directions respectively. The symbol  $\vec{B}_{i,j}$  represents the control points,  $J_{n,i}(u)$ ,  $K_{m,j}(w)$  are Bernstein functions defined as:

$$J_{n,i}(u) = \binom{n}{i} u^i (1-u)^{n-i} \quad (3.9)$$

$$K_{m,j}(w) = \binom{m}{j} w^j (1-w)^{m-j} \quad (3.10)$$

For numeric computation Bezier surfaces can also be expressed in the following matrix form [24]:

$$P(u, w) = [U][N][B][M]^T [W]^T \quad (3.11)$$

Here  $[U]$ ,  $[W]$  are functions of the parametric space and are defined as:

$$\left. \begin{array}{l} [U] = \begin{bmatrix} u^n & u^{n-1} & u^{n-2} & \dots & 1 \end{bmatrix} \\ [W] = \begin{bmatrix} w^m & w^{m-1} & w^{m-2} & \dots & 1 \end{bmatrix} \end{array} \right\} \quad (3.12)$$

$[B]$  is the matrix of the control points. In context of generating a contact pressure surface from sensor measurements the  $(i, j)^{th}$  value in matrix  $[B]$  will be the measurement from the sensor at the  $(i, j)^{th}$  position in the sensor matrix.

$$[B] = \begin{bmatrix} B_{0,0} & \dots & B_{0,m} \\ \vdots & \ddots & \vdots \\ B_{n,0} & \dots & B_{n,m} \end{bmatrix} \quad (3.13)$$

In context of generating a contact pressure surface from sensor measurements the elements of  $[N], [M]$  will solely depend on the dimensions of the sensor array i.e. ‘m’ and ‘n’.

$$\left. \begin{array}{l} [N]_{i+1,j+1}^n = \begin{cases} \binom{n}{j} \binom{n-j}{n-i-j} (-1)^{n-i-j} & 0 \leq i+j \leq n \\ 0 & \text{else} \end{cases} \\ [M]_{i+1,j+1}^m = \begin{cases} \binom{m}{j} \binom{m-j}{m-i-j} (-1)^{m-i-j} & 0 \leq i+j \leq m \\ 0 & \text{else} \end{cases} \end{array} \right\} \quad (3.14)$$

In order to highlight the properties of Bezier surfaces, an example of a  $4 \times 4$  Bezier surface is shown with its control points in Figure 3.3. The mesh joining the control points is referred to as the defining polygon net. The control points used for the example are:

Table 3.1 – Control points used in generating Bezier surface

	$B_{0,j}$	$B_{1,j}$	$B_{2,j}$	$B_{3,j}$
$B_{i,0}$	0	15	15	0
$B_{i,1}$	15	15	15	15
$B_{i,2}$	15	15	15	15
$B_{i,3}$	0	15	15	0

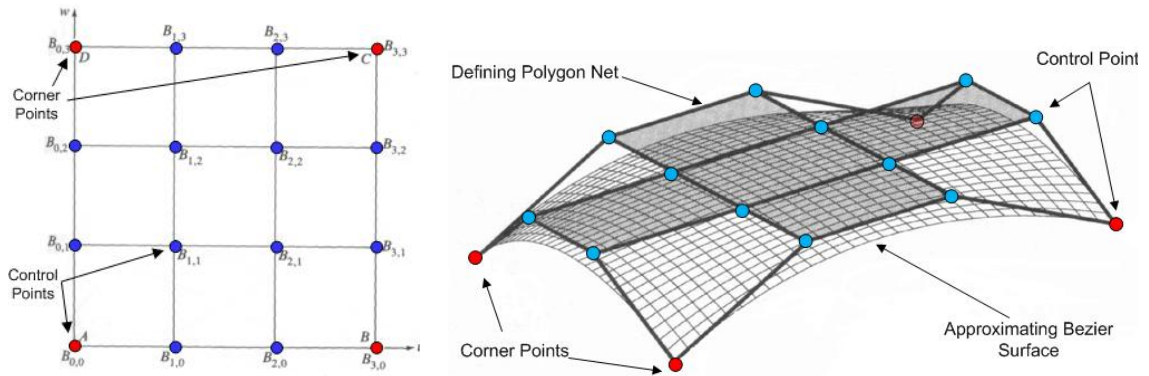


Figure 3.3 – Example Bezier surface, control points and polygon net [24]

The properties of interest for a Bezier surface are: The corner points of the surface coincide with the convex hull. This property is inherited from Bezier curves. For quadrilateral surfaces the defining polygon net should have the same number of vertices within rows and columns. However, a Bezier surface does not need to be a square. For example the defining polygon can have 20 x 30 vertices in the u and w directions. As in the case of the Bezier curves the surface is contained within the convex hull of the defining polygon net. This comes from the extension of Eqn 3.1 to two dimensions [24]:

$$\sum_{i=0}^n \sum_{j=0}^m J_{n,i}(u) K_{m,j}(w) = 1 \quad (0 \leq u, w \leq 1) \quad (3.15)$$

### 3.2 Sensor Surface Map

Initial investigations into the mathematical background of the Snake Skeleton Method indicate that the convex hull property of Bezier surfaces may cause the contact pressure distributions calculated from this technique to be inaccurate. This provides a reason to investigate interpolative surface schemes as an alternative to the Bezier scheme. Interpolative schemes generated surfaces satisfy all given control points. The same is not true for Bezier surfaces which are approximate in nature. The suitability of cubic splines and thin plate splines (T.P.S.) for representing dynamic working contact pressure distributions has been examined here. The method of estimation of punch-workpiece contact pressure using interpolation schemes and their application in defect detection will henceforth be referred to as the Sensor Surface Map (SSM).

#### 3.2.1 Interpolation Based on Cubic Splines

The cubic spline equation has its roots in deformation mechanics of materials. Cubic splines are the deformation solutions for multi support beams. Mathematically a cubic spline is a third degree polynomial interpolation of the form:

$$\vec{P}(t) = \sum_{i=1}^4 \vec{B}_i t^{i-1} \quad t_1 \leq t \leq t_2 \quad (3.16)$$

Here  $B_i$  are the control points and  $t$  the parameter used to define the curve.  $t_1$   $t_2$  are the end point values of parameter  $t$  for each segment. The value  $t_1$  is assumed to be zero without loss of generality. The value of  $t_2$  needs to be selected for each segment. Generating a cubic spline is equivalent to fitting a cubic polynomial through the given control points i.e. a minimum of 4 non-coincident control points are required to determine a non trivial cubic equation satisfying all the four control points. From basic

calculus it is known that a cubic polynomial can have a maximum of two stationeries. This implies that a cubic polynomial can not fit an arbitrary number of control points. One of the techniques for circumventing this problem involves using a series of piecewise cubic interpolations [24]. In this method each cubic interpolation only spans two points, but by using a series of two point cubic interpolations joined end to end, it is possible to fit a cubic interpolation to any number of control points. To formulate a cubic spline segment from just two points (instead of the minimum requirement of four) a different mathematical formulation has to be defined. In order to derive the piecewise formulation the defining equation (Eqn. 3.16) is differentiated with respect to  $t$  and the slope of parametric equation is found:

$$P'(t) = \sum_{i=2}^4 (i-1)B_i t^{i-2} \quad t_1 \leq t \leq t_2 \quad (3.17)$$

Eqn 3.17 allows for defining a cubic interpolation based on just two points, the lack of two defining point is made up for by maintaining second order continuity across joints and defining the slope at the spline end points. However the slope at the two end points of the series of two point cubic interpolations is an unknown quantity. There are a number of schemes which allow for a selection of the end point slopes. The not-a-knot condition was used in the study here. This condition determines the end point slopes by merging the first two and the last two polynomial segments in the cubic spline. For computational purposes the defining equation for a cubic spline defined by  $(n-1)$  cubic segments to fit  $n$  data points is restated in matrix form [24]. The parameter  $\tau$  varies from 0 to 1 within each segment.  $P_k$  are the control points where  $k$  varies from 1 to  $(n-1)$ .

$$P_k(t) = [F_1(\tau) \ F_2(\tau) \ F_3(\tau) \ F_4(\tau)] \begin{bmatrix} P_k \\ P_{k+1} \\ P'_k \\ P'_{k+1} \end{bmatrix} \quad \begin{cases} 0 \leq \tau \leq 1 \\ 1 \leq k \leq n-1 \end{cases} \quad (3.18)$$

Here  $F_i(\tau)$  are weighting functions of  $\tau$  and  $t_{k+1}$  defined as:

$$\left. \begin{array}{l} F_{1k}(\tau) = 2\tau^3 - 3\tau^2 + 1 \\ F_{2k}(\tau) = -2\tau^3 + 3\tau^2 \\ F_{3k}(\tau) = \tau(\tau^2 - 2\tau + 1)t_{k+1} \\ F_{4k}(\tau) = \tau(\tau^2 - \tau)t_{k+1} \end{array} \right\} \quad (3.19)$$

The value of  $t_k$  can be selected by two computationally inexpensive methods. The first method is to let the value of  $t_k$  be unity for each segment. The other method takes the value of  $t_k$  to be equal to the chord length between the two control points for that segment of the cubic interpolation. Though the slopes at the end points  $P'_1 \ P'_n$  are known, slope at any intermediate  $P'_k$  is an unknown and is determined from the second order continuity condition imposed on each joint. The mathematical implementation of this condition provides this recursive equation for calculating  $P'_k$  [24]:

$$[P'] = [M]^{-1}[R] \quad (3.20)$$

$[P']$  is a vector consisting of slopes of the cubic spline at the control points and  $[R]$  is a vector function of the slopes at the end of the series of cubic interpolations  $(P'_1, P'_n)$ , the control points  $P_i$  and  $t_k$  the values of which are selected as described before.

$$[P'] = \begin{bmatrix} P_1' \\ P_2' \\ \vdots \\ P_{n-1}' \\ P_n' \end{bmatrix} \quad (3.21)$$

$$[R] = \begin{bmatrix} P_1' \\ \frac{3}{t_2 t_3} \{t_2^2 (P_3 - P_2) + t_3^2 (P_2 - P_1)\} \\ \frac{3}{t_3 t_4} \{t_3^2 (P_4 - P_3) + t_4^2 (P_3 - P_2)\} \\ \vdots \\ \frac{3}{t_{n-1} t_n} \{t_{n-1}^2 (P_n - P_{n-1}) + t_n^2 (P_{n-1} - P_{n-2})\} \\ P_n' \end{bmatrix} \quad (3.22)$$

$[M]$  is dependent only on value of  $t_k$ . Its matrix expression is:

$$[M] = \begin{bmatrix} 1 & 0 & \dots & \dots & \dots & \dots & \dots & \dots \\ t_3 & 2(t_2 + t_3) & t_3 & 0 & \dots & \dots & \dots & \dots \\ 0 & t_4 & 2(t_3 + t_4) & t_3 & 0 & \dots & \dots & \dots \\ 0 & 0 & t_5 & 2(t_4 + t_5) & t_4 & 0 & \dots & \dots \\ \dots & \dots \\ \dots & \dots \\ \dots & \dots & \dots & \dots & 0 & t_n & 2(t_n + t_{n-1}) & t_{n-1} \\ \dots & \dots & \dots & \dots & \dots & \dots & 0 & 1 \end{bmatrix} \quad (3.23)$$

The blending functions of Eqn 3.18 are plotted against parameter  $t$  in Figure 3.3. It is seen that  $F_1(\tau)$   $F_2(\tau)$  are monotonic while  $F_3(\tau)$   $F_4(\tau)$  each have a maxima and minima respectively. The significance of this is:

1. The first and last points are coincident with the first and last points of defining polynomial. This feature insures that the curve passes through all the data points.
2. Since  $F_1(\tau)$   $F_2(\tau)$  have the dominating magnitudes the nature of curve is more influenced by the value of end points as compared to the prescribed slopes.

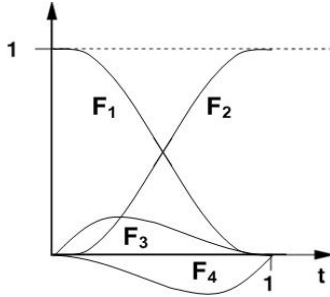


Figure 3.4 - Four point blending functions for Cubic spline

### 3.2.2 Interpolation Based on Thin Plate Spline

The 3D equivalent of Cubic Spline is the Thin Plate Spline (TPS) surfaces. The Thin Plate Spline method derives its name from the fact that the shape of the surfaces generated by this method are visually similar to a thin metal sheet constrained at certain points. The Thin Plate Spline surface is mathematically defined as the function  $z = P(x, y)$  which minimizes the following function [27, 28]:

$$R(P) = \iint_{R^2} (P_{xx}^2 + 2P_{xy}^2 + P_{yy}^2) dx dy \quad (3.24)$$

The solution of which is of the following form:

$$z = P(x, y) = \sum_{j=1}^n a_j E(x, y) + b_0 + b_1 x + b_2 y \quad (3.25)$$

$a_j, b_0, b_1, b_2$  are constants which are found applying interpolation conditions on Eqn. 3.26

and ‘n’ is the total number of control points and the function  $E(x, y)$  is defined as:

$$\left. \begin{aligned} E(x, y) &= J(\|(x - x_j, y - y_j)\|) \\ J(v) &= v^2 \log(v^2) \\ \|\cdot\| &= \text{length of vector} \end{aligned} \right\} \quad (3.26)$$

Having setup the mathematical background for the Bezier and Thin Plate Spline methods, Section 3.3 uses the contact pressure information obtained from FE simulations in Chapter 2 for comparing the accuracy of the two methods.

### **3.3 Contact Pressure Estimation in SSG and SSM Methods**

#### **3.3.1 Approach**

In this Section the accuracy of pressure estimation by SSG and SSM methods is compared based on known pressure distributions on the punch-workpiece interface, which were determined by finite element modeling in Chapter 2. To accomplish this, contact pressure data from a fixed set of locations on the punch face is processed using SSG and SSM methods to estimate the pressure distribution on the punch-workpiece interface. To evaluate the accuracy of the surface schemes the SSG/SSM estimated pressure distributions are compared with the FE calculated contact pressure distribution.

#### **3.3.2 2D Bezier Approximation vs. Cubic Interpolations**

The FE calculated contact pressure data was sampled at three locations. The locations of these data sampling points are 1", 3", and 5" from the left edge of the punch. The fact that contact pressure on the corners of the punch tends to zero was used to add two extra control points by assuming zero contact pressure at 0" and 7". These sampled data was used to develop SSG and SSM contact pressure approximations. Fig 3.5 shows the pressure distribution at T=0.25 secs, the controlling polygon and the associated Bezier approximation. Because of approximate nature of the technique the Bezier estimated pressure curve does not pass through the control points. It is seen that the two local pressure maximums are undetectable in the Bezier representation. In comparison Figure 3.6 shows the pressure distribution at the same instant evaluated using Cubic Spline. On comparing with the Bezier approximation in Figure 3.5 it is obvious that the local stationeries are better represented by the interpolative technique.

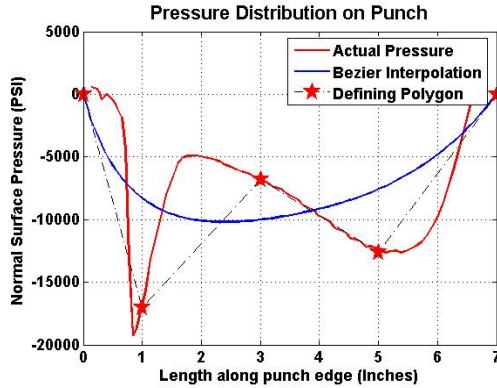


Figure 3.5 - Bezier pressure approximation

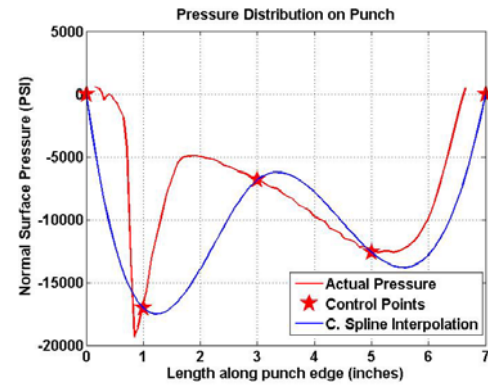


Figure 3.6 - Cubic interpolation of pressure

### 3.3.3 Bezier Surfaces vs. Thin Plate Splines

The equations required to develop the SSG and SSM contact pressure estimates were coded in Matlab. These programs were used to calculate the numeric surfaces approximating the contact pressure distribution on the FE simulated die-workpiece interface. 20 surfaces were generated between  $T=0$  to 500 ms, the surfaces being calculated every 10 ms between  $T=200$  ms and  $T=300$  ms because the maximum forming action happens at this period, at other times 100ms intervals were used. Each numeric surface was computed at 4900 data points spread over its surface. The control point data (contact pressure values) used to generate the surfaces was sampled from the FE model at 9 uniformly distributed points on the punch working surface. Figure 3.7 shows the Bezier surface (Blue) developed at  $T=250$  ms superposed over the FE contact pressure data it was generated from, and the coordinates of the control points. It is seen in the figure, the Bezier surface underestimates the FE reference contact pressure. This is attributed to the Bezier surfaces property of being contained in the convex hull of the control points. Figure 3.8 shows the TPS surface (Blue) developed at  $T=250$  ms superposed over the FE reference contact pressure. The control points used to develop the surface are same as in the case of the Bezier surface.

The accurate estimation of the maximum contact pressure is vital for process monitoring, because its position and value are directly affected in defects such as die misalignment and shut height variation. In addition if the maximum pressure exceeds a limit die fracture may occur. The maximum contact pressure curve during the FE simulated process is given in Figure 3.9, as a comparison the Bezier and TPS estimated curves are included. From the curves it is clear that the convex hull property of the Bezier limits its accuracy in estimating the maximum contact pressure. The average accuracy in estimating the maximum contact pressure is 91% for TPS, in comparison the accuracy for Bezier is 45%. The accuracies were calculated as the average of 10 points between  $t=0.2\sim0.3$  because this period is most relevant in the forming process.

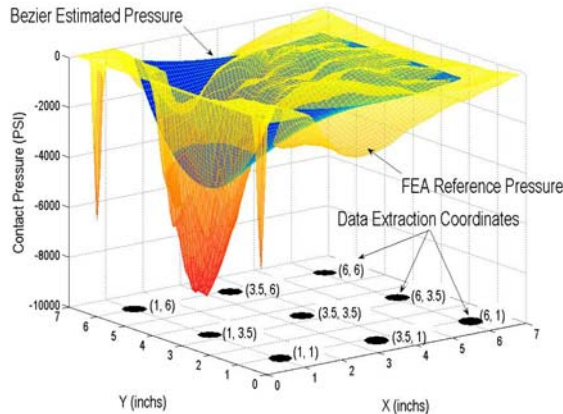


Figure 3.7 - SSG approximated pressure

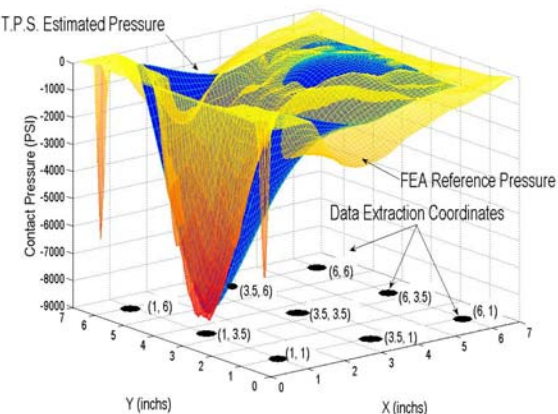


Figure 3.8 - SSM interpolated pressure

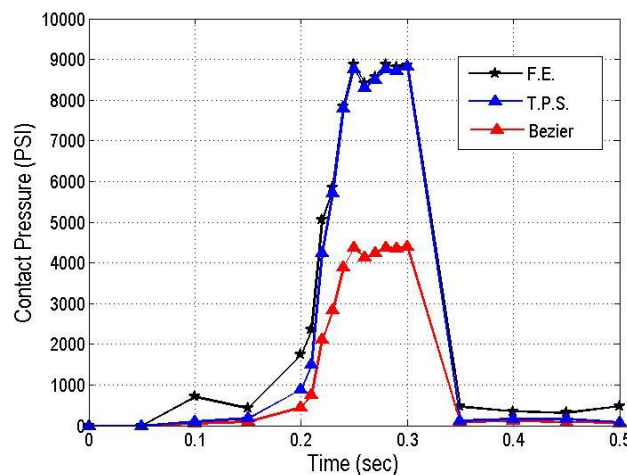


Figure 3.9 – Estimated maximum contact pressure and FE reference value

## CHAPTER 4

### EXPERIMENTAL EVALUATION

#### 4.1 Sensing Package

##### 4.1.1 Sensing Element

In order to conduct experiments for measuring the contact pressure on tooling interfaces it was required to develop a sensor package for accurately measuring contact pressure. In addition it was required that the package be convenient to embed into metallic mediums. It was decided to design the sensor package around a thin-film sensing element. The sensing element used in the initial studies is Tecktronic's FlexiForce sensor (Figure 4.1). Its small footprint, low profile and flexibility make it suitable for the purpose. However, the sensor is a force sensing element, in order to use the force sensing element for contact pressure sensing purposes the sensor packages were designed to distribute the force on the package uniformly over the circular sensing area of the element.



Figure 4.1 - FlexiForce sensor

The force applied to the sensing element affects the resistance of the element. The change of conductance (inverse of resistance) is linearly related to the force applied. Figure 4.2a shows the calibration chart supplied by the manufacturer. A driver circuit

has to be used to convert the linear conductance property into a linear voltage output for measurement and recording purposes. The sensing element was calibrated to verify the manufacturer claims the calibration chart is shown in Figure 4.2b.. The sensing element was determined to have a sensing range of 0-900 PSI, better than 5% linearity, and a response time less 5  $\mu$ s.

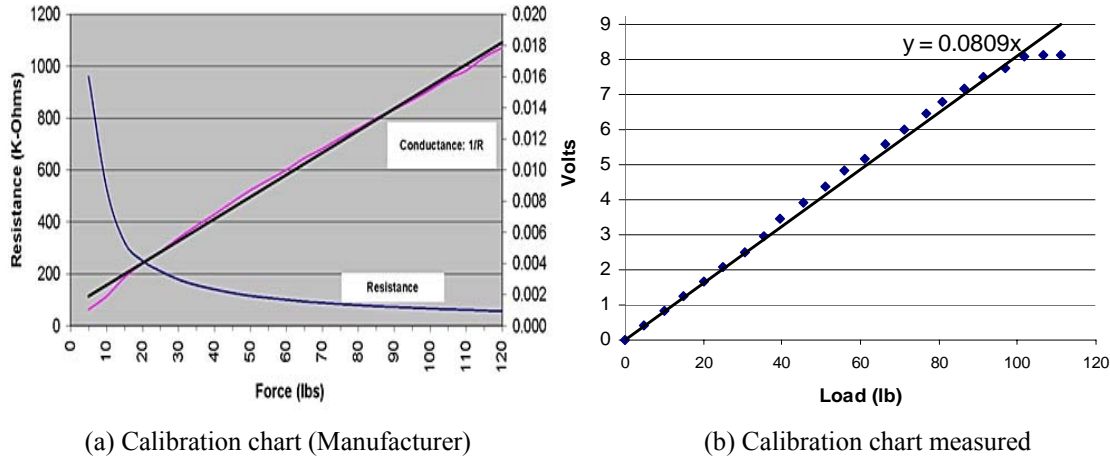


Figure 4.2 – Calibration of sensing element

#### 4.1.2 Sensor Package Designs

Two separate sensor installations are currently under consideration. In the first design the sensing element is sandwiched between a cap and a support bar (Figure 4.3, 4.4) and inserted into a blind hole drilled from the back side of the metal surface (referred to as metal medium) on which the contact pressure needs to be measured. A back plate bolted to the metal medium is installed behind the support bar to hold the assembly. A setscrew allows for adjusting sensor preload.

The purpose of the top cap is to insure a uniform contact pressure distribution over the sensing area of the element. The cap design was studied using finite element techniques to determine the contact pressure distribution over the sensing element. The 2D FE was loaded with an axisymmetric load over the center axis of the sensing

element. The contact pressure distribution over the sensing area as determined by different mesh sizes (Table 4.1) was found to be uniform (Figure 4.5). The material choice for the sensor cap and support bar is a research issue which will be studied using finite element simulations. All material models are isotropic and elastic. The sensor cap, metal medium and support bar have the structural properties of Aluminum Alloy (Al-6061) and the sensor has the structural properties of poly-ethylene.

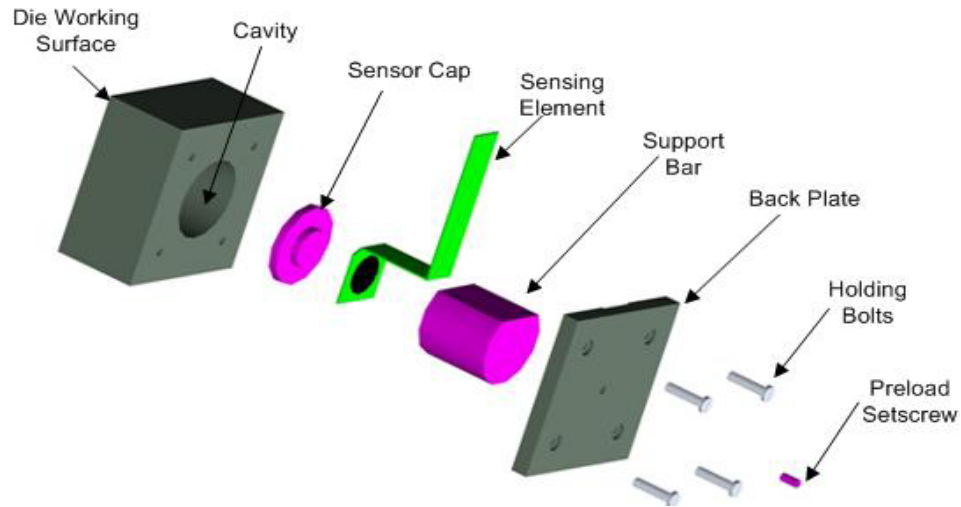


Figure 4.3 – Exploded view of first sensing package

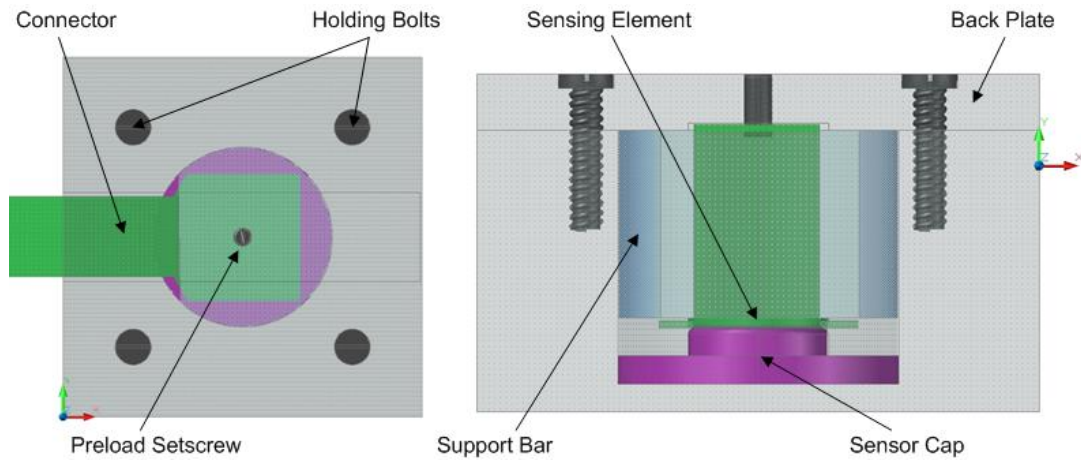


Figure 4.4 – Top and front in-situ view of first package

The second design involves packaging the sensor into a small cylindrical capsule (Figure 4.6). To install the capsule into the metal medium a blind hole is drilled from

the back side of the die and the capsule is inserted into it. Once the capsule is in place the sensor is hooked up with a monitoring device and the cavity is injected with an epoxy resin. The resin is rammed before curing to attain desired preload on the sensor. The sensing capsule consists of three components, the sensing element, the top cap and the back plate. The back plate is grinded to a smooth finish and its purpose is to provide a good contact surface for the sensor. The design of the top cap is similar to the one in the first package.

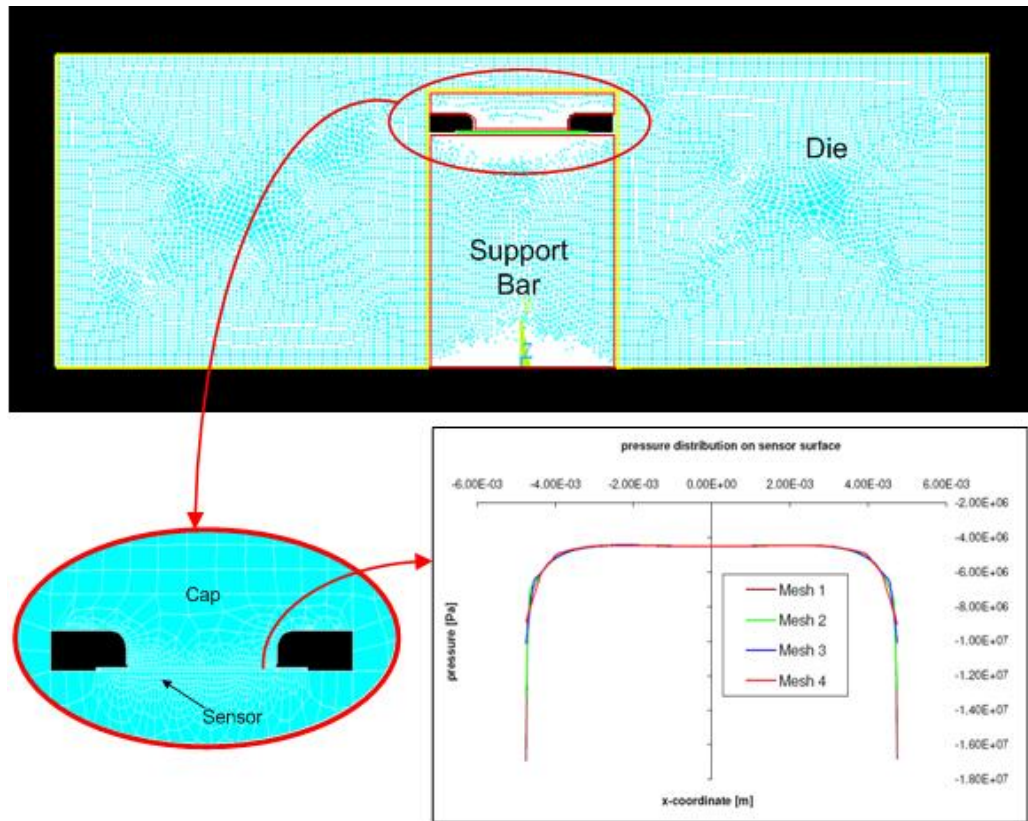


Figure 4.5 – Finite element model and contact pressure distribution on sensing area

Table 4.1 – Mesh element size for finite element model (mm)

	<b>Mesh 1</b>	<b>Mesh 2</b>	<b>Mesh 3</b>	<b>Mesh 4</b>
<b>Die</b>	0.05	0.1	0.2	0.4
<b>Sensor</b>	0.005	0.01	0.02	0.04
<b>Cap</b>	0.005	0.01	0.02	0.04
<b>Bar</b>	0.02	0.05	0.1	0.2

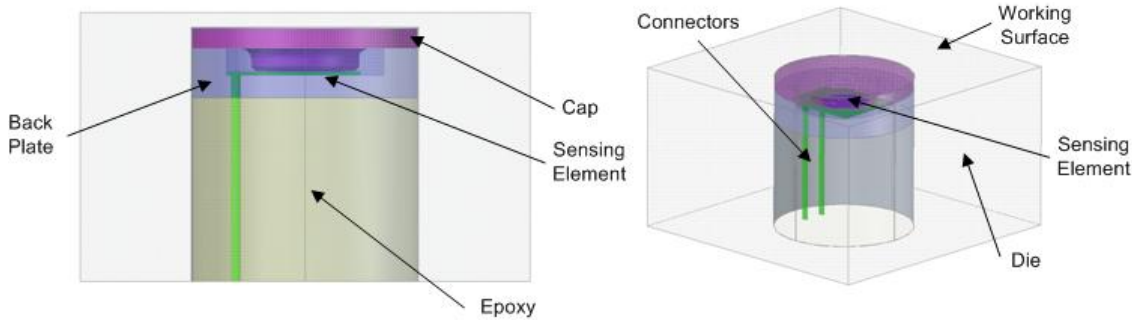
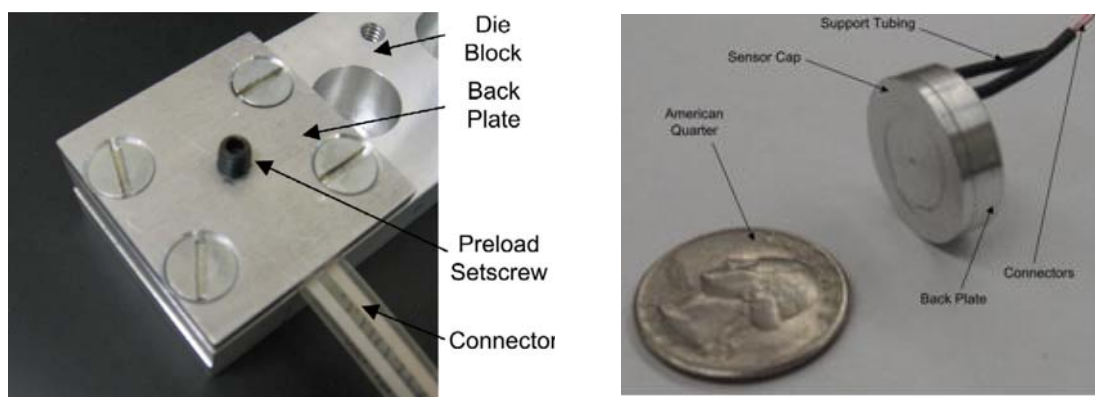


Figure 4.6 – In-situ view of second sensor package

#### 4.1.3 Sensing Package Prototypes

One prototype of each design has been fabricated for testing purposes. The prototype of the first design is shown in Figure 4.7a. The prototype of the second sensor package design is shown in Figure 4.7b. The prototype of the second sensor package design is much more difficult to fabricate as compared to the first design. One of the main difficulties is in trimming the factory connector on the sensor and installing out-of-plane enamel insulated copper connectors on the trimmed connectors. Since the original connector is a very thin layer (0.09mm) of silver laminated between two plastic strips it is not possible to solder or wire bond the connectors. Currently conductive epoxy is being utilized for the purpose. As a result the package construction is not very robust and is prone to failure during test loading. The failure is either due to detachment of the copper connectors or due to shorting of the two output terminals of the sensor.



(a) Prototype of first package  
(b) Prototype of second package

Figure 4.7 – Sensor package prototypes

## 4.2 Effect of Embedding Depth on Sensitivity

Several experiments were conducted to quantify the response of metal embedded sensors to different embedding depths and loading conditions. Specifically, the effects of embedding depth, loading area and dynamic loading have been studied using the first sensor package prototype. Figure 4.8 shows the sensor embedding setup and its components. The test block material in which the sensor was embedded is Al6061. Test loads were applied directly over the center of the sensing element.

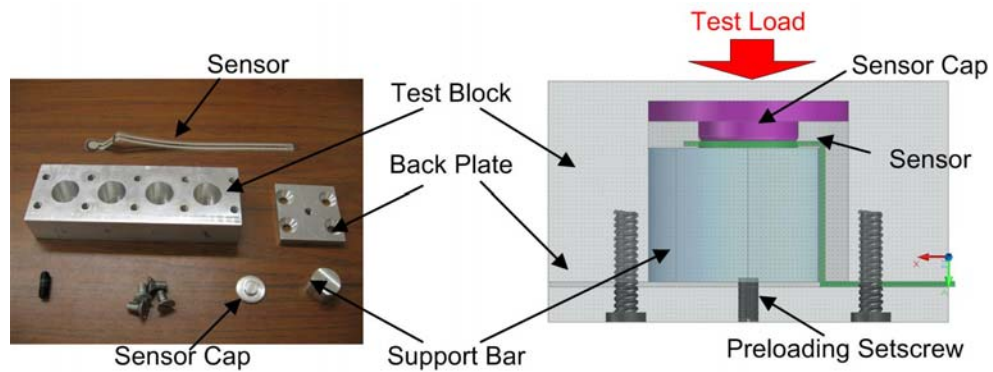


Figure 4.8 – Sensor embedding components

The experiments conducted can be classified on the basis of loading technique as quasi-static or dynamic. In the former, load was applied at a very slow rate (10 lbf/min) avoiding any transitional effects. In the latter the loading rate was much higher (100 lbs/sec to 30 klf/sec). In each class of experiment load was applied through a (ball) point contact and two cylinders of different radii. Even when the same load was applied, differences in the contact areas lead to different stress distributions and consequently large variations in the sensor measurements. The results for the quasi-static loading experiments are summarized in Figure 4.9. Examining the sensitivity curve for point contact load (Red), it is seen that the sensitivity of the embedded sensor decreases exponentially for small embedding depths but approaches a minimum value between 6

to 8 mm. This seems to indicate that embedded sensors are highly sensitive to strongly localized loads near the sensing axis. In an actual stamping operation such load localizations might arise from slugs or wrinkles in the workpiece material, thus presenting a method to distinguish slugs/ wrinkles from other possible forming defects.

Distributed loads like in the case of circular contact loads (Blue & Green) are more representative of expected loading conditions in a stamping tooling structure. It is seen that measurement sensitivity for distributed loads is less affected by embedding depth in the 2mm to 8 mm range and approaches a minimum value in a manner similar to sensitivity of concentrated loads. The asymptotic behavior of sensitivity is attributed to St. Venant's Principle, as the sensor is located farther and farther away from event site the stress field in the block attains uniformity. At this time lack of experimental data in the 0 mm to 2 mm embedding depth range prevents definitive conclusions as to the behavior of measurement sensitivity at very small depths. Still the precedent of the concentrated loading case seems to indicate likelihood of an exponential increase of measurement sensitivity at very small embedding depths.

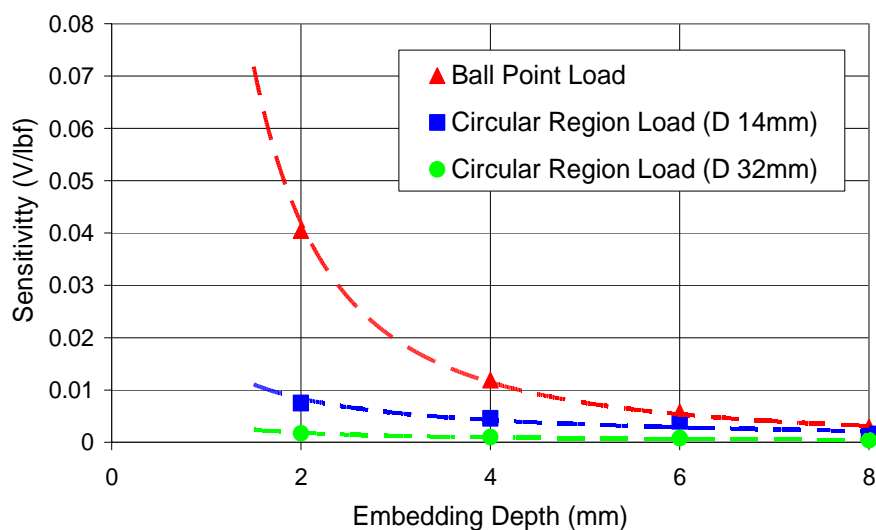


Figure 4.9 – Quasi-static loading results

The dynamic experiments consisted of tests with ramped and impulse loads. The load was ramped at 100lbs/sec, Figure 4.10 shows the response to the same ramped load applied through the 14mm diameter cylinder for sensors embedded at different depths. The applied load recorded externally by a standard load cell is shown in Red superposed over the sensor responses. As expected amplitude of the sensor response decreases nonlinearly with increase in depth such that the response for 6mm and 8mm depths is almost the same. However an aspect of the sensor response is the initial non-linear sensor response to applied load for 2mm and 4 mm depths. It is speculated that the reason for this is the difference in the material properties of the sensing element and the embedding medium. Different elasticity constants of the embedding medium and the sensor cause them to respond differently and the combined response becomes non-linear at high loading rates.

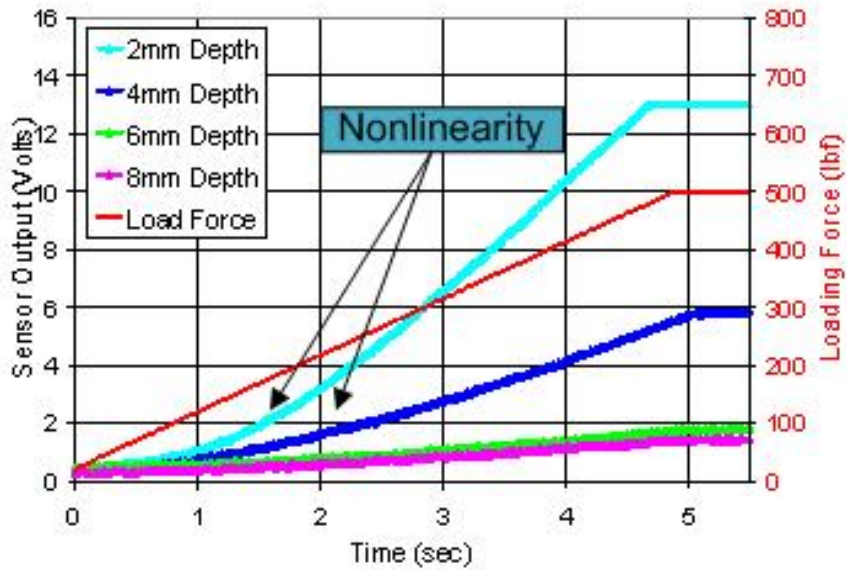


Figure 4.10 – Ramp loading by 14mm cylinder

In the impulse loading dynamic experiments, a load lasting 500 milliseconds was applied to the sensing setup. Figure 4.11 shows the sensor measurements of an identical

impulse load (Red) applied through the 14mm diameter cylinder to sensors embedded at different depths. The press used for applying the impulse force had an over shoot and recovery characteristic of most load control systems installed in stamping presses (magnified box), this feature has been utilized here to correlate the applied load to the sensor measurement. The sensor outputs from different depths and loading conditions have been correlated with the applied force signal. The results are listed in Table 4.2. It is seen that the correlation between sensor output and applied load decreases with increasing embedding depth, in addition distributed loads are less correlated as compared to concentrated loads. Some correlation values are unavailable because of sensor output saturation.

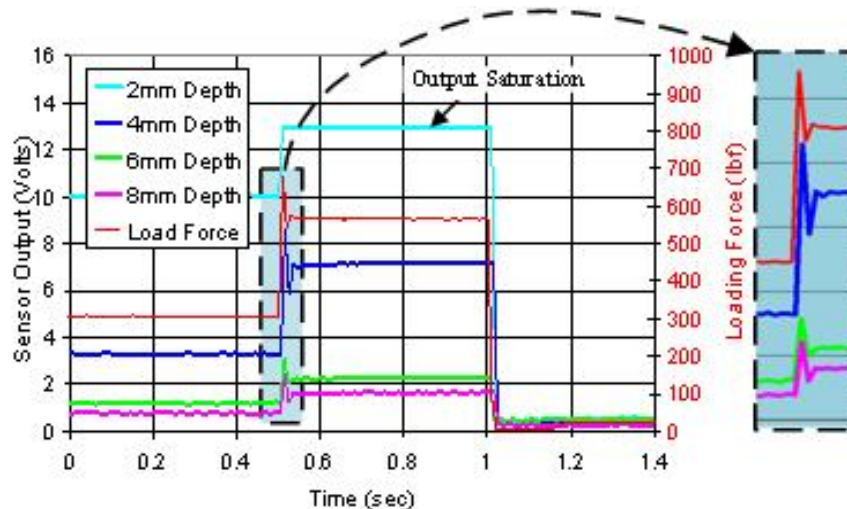


Figure 4.11 – Impulse loading by 14mm cylinder

Table 4.2 – Correlation between applied load and sensor measurements

Depth\Load	Ball Load	14mm Cylinder	32mm Cylinder
<b>2</b>	N.A.	N.A.	0.9612
<b>4</b>	N.A.	0.9880	0.9355
<b>6</b>	0.9808	0.9639	0.9168
<b>8</b>	0.9323	0.9810	0.8807

### 4.3 Experiments on a Contact pressure Sensor Array

To further evaluate the TPS contact pressure estimation method, a set of contact pressure sensors was incorporated into an experimental test setup. The test setup consists of two 6" x 8" mating plates of AL6061, each 1.5" thick with an average surface roughness of  $22 \mu\text{ in}$ . The bottom plate has a 3"x 5" through slot cut in the center to aid in sensor placement, in addition a mechanical alignment controller has been incorporated into its design. The role of the alignment controller is to control the parallelism of the two mating surface. While the top plate or the impact plate is passive the bottom plate has been embedded with an array of eight sensors. The setup is mounted on an Instron hydraulic press installed with a calibrated loaded cell rated for 10Klbf. The test setup, sensor placement, and an example of acquired contact pressure signals are shown in Figure 4.12. The measurements were recorded by a program written in Labview and through a driver circuit, at a sampling rate of 100 Hz. The instantaneous press force was also measured from the load cell. The test setup was subjected to sinusoidal, triangular and impulsive loading of different amplitudes and the measurements from the sensor array were used to estimate the contact pressure distribution using the TPS scheme.

Figure 4.13 shows the TPS estimated contact pressure for the case of a half sinusoid press force of amplitude 500 lbf and time duration of 1 second. Each distinct surface represents the TPS calculated estimate of the contact pressure distribution at a time instant. For visual clarity only 10 surfaces are shown here. As expected the contact pressure distribution on the surface first increases with time, reaching a maximum at  $T=2.2$  secs and then decreasing. From a spatial perspective the mid part along the length

of the die ( $x=4''$ ) is subjected to the highest contact pressures. This is attributed to the shape of the alignment controller which supports the sensor plate only in the middle, leading to higher compressive stresses in that region.

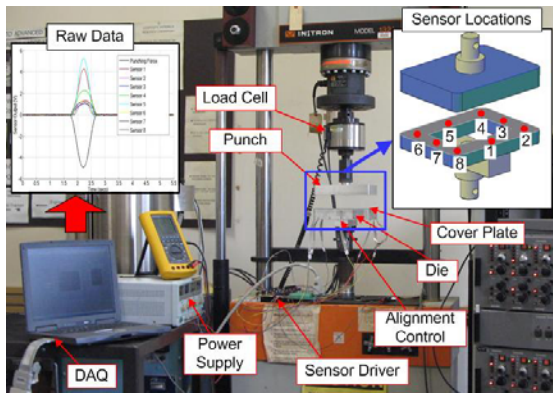


Figure 4.12 – Experimental setup

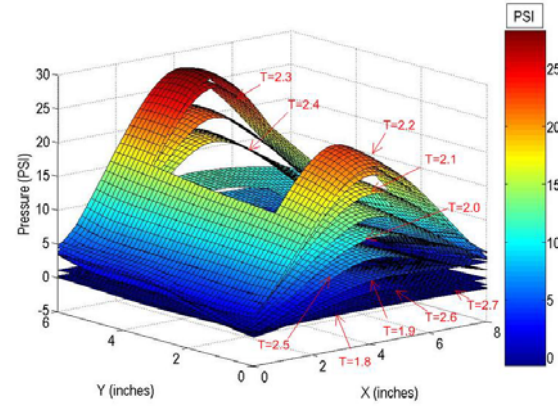


Figure 4.13 – TPS estimated contact pressure

To evaluate the accuracy of the contact pressure estimation scheme the estimated contact pressure was numerically integrated over the surface of the sensor plate to determine the net force acting on the interface. As long as the acceleration of the plates is negligible, the net force would ideally be equal to the load cell measurement. When compared over many time instants the difference between the two values would be indicative of the variation in estimation error with time. Figure 4.14 shows the press force measured from the load cell plotted with the integral of the TPS calculated contact pressure distribution over the plate surface. It is found that the error is largest when the press force is at its peak. In addition the surface calculated press force lags behind the load cell measured press force by approximately 0.1 secs during increasing load, there is no such phase lag during load removal. The same was found to be true for triangular and impulsive press forces too.

In order to demonstrate the feasibility of using embedded contact pressure sensing in process defect detection, the alignment controller built into the experimental setup

was used to simulate deviations in slide parallelism. Slide parallelism is the maximum out of plane alignment of the stamping punch with the die bed as it travels the press slides. It is measured in units of length. Typical its value should be a few thousands of an inch, defects may occur if the value increases due to any reasons.

The setup has been used to identify the affects of deviations in slide parallelism on contact pressure. The deviations were introduced through the alignment controller built into the sensor plate. Figure 4.15 shows the TPS pressure distribution calculated from the sensor measurements when an angular deviation of  $0.286^\circ$  was introduced along the width of the plate, corresponding to a  $0.030"$  error in slide parallelism. The applied press force was the same as before. It can be seen that the small deviation in slide parallelism leads to a significant redistribution of the contact pressure. As expected the highest contact pressures occur on the area where the impact plate and the sensor plate impact first. The saturation of the sensor output in that location cause the TPS estimated contact pressure distributions from time 2.1 to 2.4 secs to converge in that region.

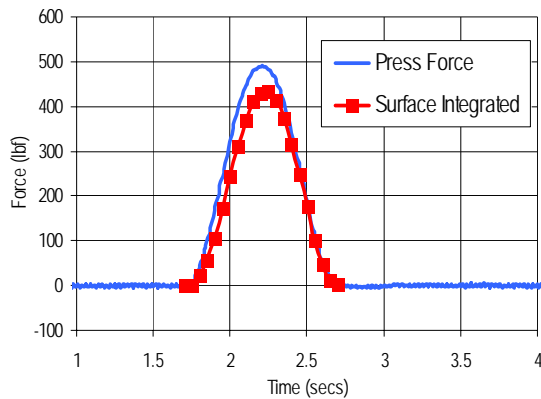


Figure 4.14 –Measured vs. integrated force

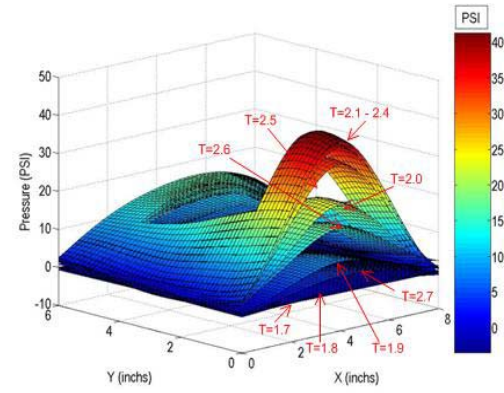


Figure 4.15 – TPS estimated contact pressure

Examining the estimated contact pressure distributions visually is appealing to die designers and for those trying to understand the fundamental mechanics of the process and the concomitant defects.

## 4.4 Stamping Test Bed

### 4.4.1 Experimental Setup

In order to evaluate the proposed sensing scheme, panel stamping tests were performed on a hydraulic stamping test bed. The test bed utilizes a 45kN Instron hydraulic press equipped for simultaneous load and stroke monitoring. It is designed to stamp out a 10 mm deep Aluminum panel from a 20cm x 15cm sheet metal workpiece 0.51mm thick. Figure 4.16(a) shows the tooling set up, the binder is mounted on four die springs each having a spring constant of 51 N/mm to mimic the forming action of a single action stamping press. Slight adjustments to the binder force are possible by addition of spacers in series to the die springs. The clearance between the punch and die cavity walls is 0.60 mm.

The array of force sensors is installed in the stamping die. Installation of sensors in the die permits measurement of binder and punch contact pressure without machining the punch and binder. Figure 4.16(c) describes the components in a sensor installation. Each sensor is over a steel bar (support bar) located over a centrally located setscrew for controlling the sensor preload. Figure 4.16(b) shows the interface between the die and die shoe with the support bars and preload setscrews. Since the sensor was originally designed for force measurements in order to measure contact pressure a sensor cap was used to redistribute the active loads uniformly over its sensing area. The sensitivity of sensors embedded at different depths to surface loading has been determined by prior experimentation.

The fully assembled test bed mounted on the Instron press is shown in Figure 4.17. The top-right inset shows the reference numbers for the 18 sensor locations. Out of the

18 possible locations for the sensors, up to 16 can be used simultaneously. The materials used in the construction of the test bed and their physical properties are listed in Table 4.3.

Table 4.3: Test bed materials and properties

Part	Material/ Temper	Density (kg/m <sup>3</sup> )	Poisson's Ratio	Elastic Modulus (GPa)	Hardness (Brinell)	Yield Strength (MPa)
<b>Die / Punch / Binder</b>	AA6061/T6	2700	0.33	69	95	241
<b>Die &amp; Punch Shoe</b>	Steel	7860	0.30	210	-	690
<b>Workpiece</b>	AA1100/0	2710	0.33	65	23	34

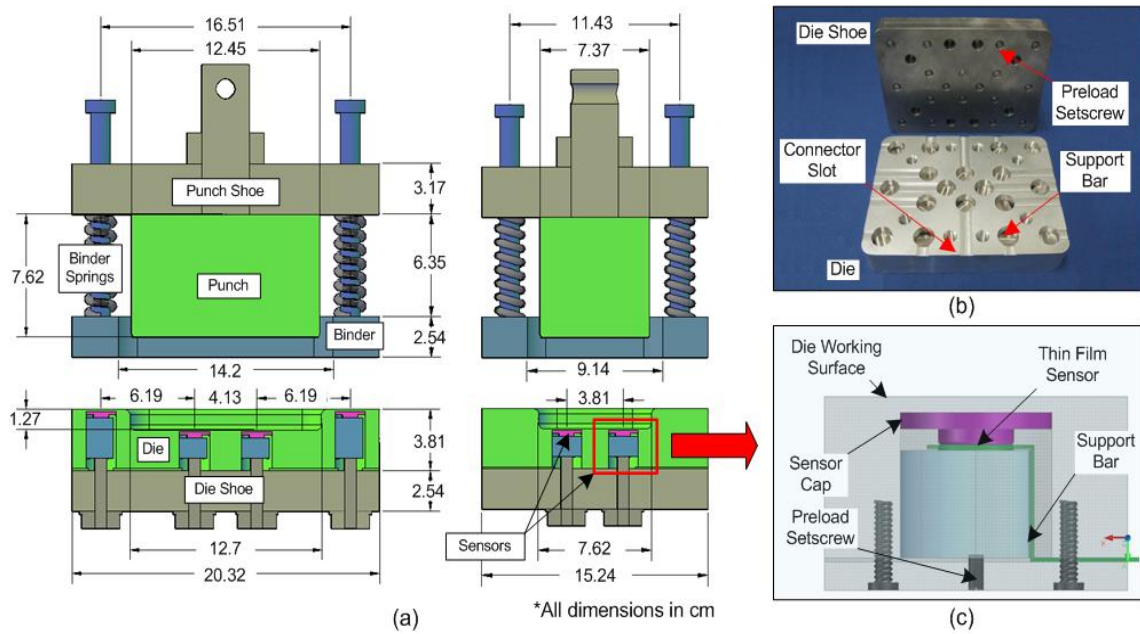


Figure 4.16 - CAD drawing of test bed design and sensor installation

The Instron machine was programmed for a half sinusoidal stroke having a rise time of 10 seconds. In each test the shut height was maintained at 0.6 mm. Before each test the die surface was evenly sprayed with 1120 straight oil lubricant. The sensor measurements, press force, and stroke were recorded through a Labview program by

means of an electronic driver circuit (see inset sensor driver in Figure 4.17), at a sampling rate of 100 Hz. The following section describes the contact pressure surfaces developed in the stamping of a defect free panel formation.

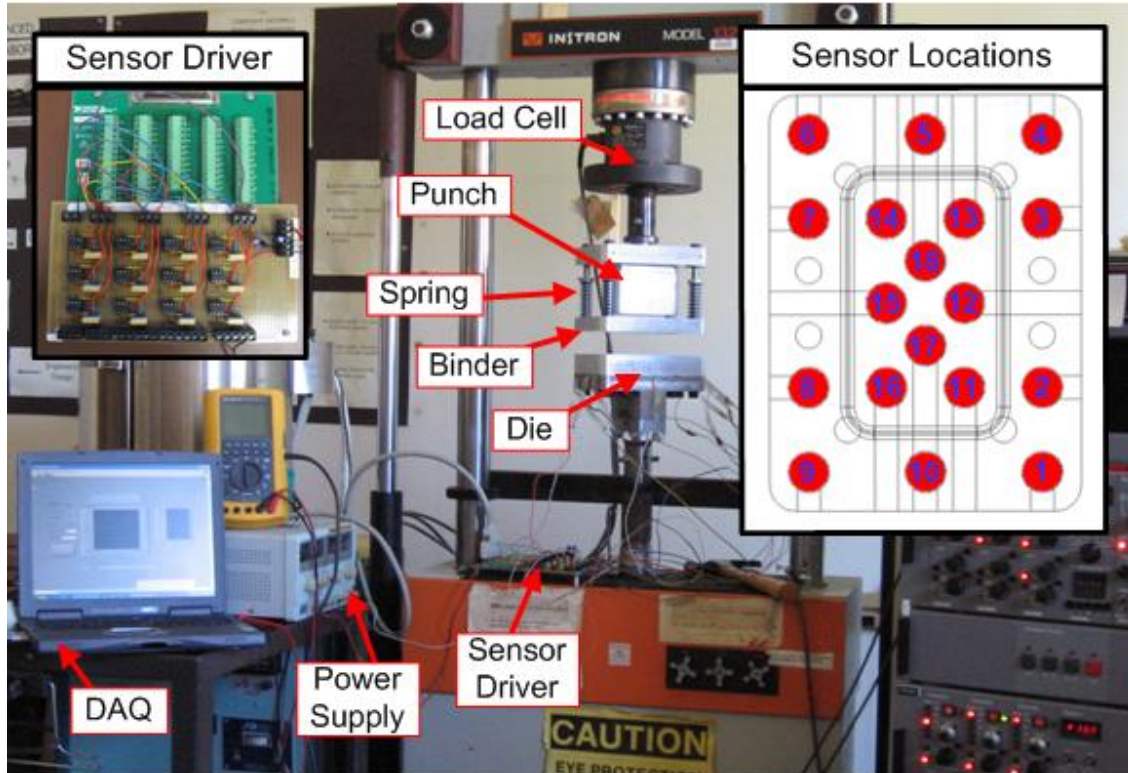


Figure 4.17 - Experimental test bed, sensor positions, and driver circuit

#### 4.4.2 Contact Pressure Surfaces – Normal Process

During the following test 14 sensors were embedded in the die. The sensors embedded in the binder contact region were at locations 1, 2, 4, 6, 7, and 9 (see inset sensor locations in Figure 4.17). Sensors 11 through 18 located under the die cavity were also active. Based on measurements from these sensors, contact pressure surfaces for the binder and die cavity areas were generated. To achieve this, the equations for the TPS surface technique presented in Section II were coded into a Matlab program. The sensor measurements from the sensors in the binder and die cavity are shown in Figure 4.18(a) and 4.18(b) respectively. There were 40 contact pressure surfaces developed for

the die cavity contact region and 80 for the binder region. Figure 4.19(a) shows the contact pressure surfaces corresponding to the die cavity region between time T=7 to T= 17 seconds and Figure 4.19(b) shows the contact pressure surfaces for the binder contact region between T=4 to T=22 seconds. For visual clarity only 10 contact pressure surfaces are shown here. The surfaces have been calculated on a grid of 50 row and 50 columns, leading to a total of 2500 grid points.

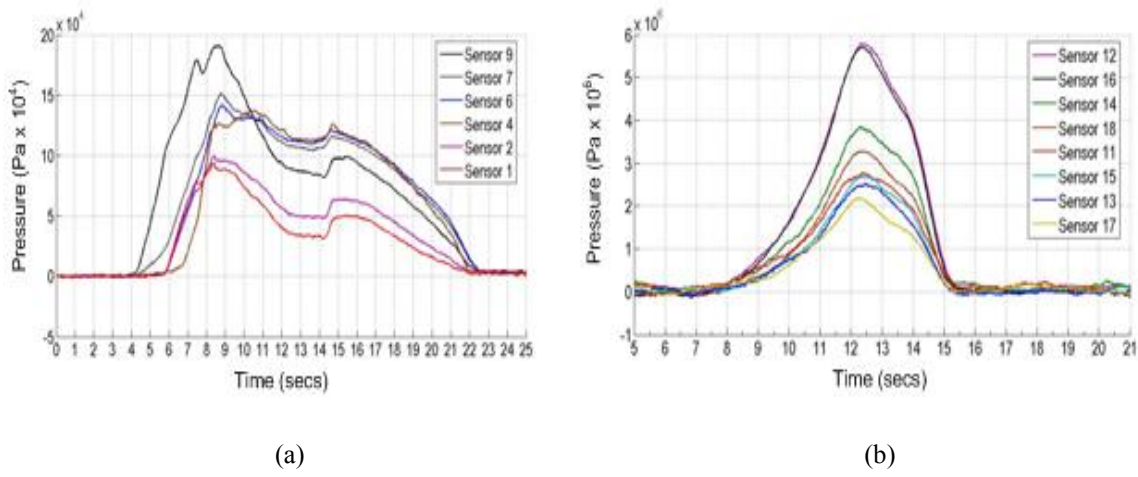


Figure 4.18 - Sensor measurements from binder (a) and within die cavity (b)

In Figure 4.19(a) and 4.19(b) the binder contact pressure is seen to reverse trend at around T=9 secs. This is caused by a redistribution of the contact pressure between the binder and die cavity region, the increasing contact pressure within the die cavity causes the binder contact pressure to decrease. Previous research has shown that lowered binder contact pressure can lead to flange wrinkling, this could account for the frequent cases of wrinkling encountered during testing. From the die cavity contact pressure surfaces it is observed that even though the forming tools and product are symmetric the contact pressure distribution is observably non-symmetric. Furthermore, the presence of large contact pressure at the die corner and edge can lead to formation of defects. Repeated testing has revealed that the shape of contact pressure surfaces changes each

time the die is removed and reinstalled on the Instron press. This indicates that the surface shape is highly sensitive to clearances between the die and the punch. A process monitoring system could use this property of contact pressure surfaces to automatically maintain optimum tooling clearances during stamping operations.

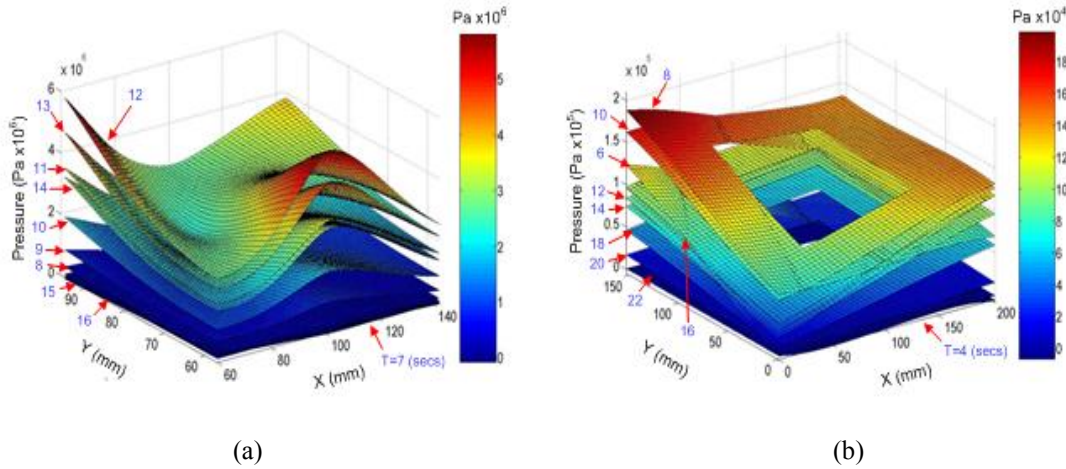


Figure 4.19 - Contact pressure surfaces for sensors within die cavity (a) and on binder (b)

The application of embedded contact pressure sensing technique to high volume production necessitates a method for automatic evaluation of contact pressure surfaces by a process monitoring system. One possible manner in which this can be achieved is by encapsulating useful information present in the contact pressure surfaces in a set of parameters. To study the feasibility of this approach it was attempted to characterize the contact pressure surfaces developed from the experimental results through the following three parameters: the minimum, maximum, and mean contact pressure determined from the contact pressure surfaces. The parameters have been selected because of their inherent physical relevance to the stamping process. By examining temporal variations of these parameters in addition to the spatial variation of their point of action it is sought to characterize the contact process between the workpiece and the die. Figure 4.20(a) shows the temporal variation of the parameters for contact pressure surfaces in the die

cavity region. The maximum contact pressure in the process occurs when the punch is at the lowest point of its stroke, at this instant the contact pressure at different points within the die cavity varies from 6.1 MPa to 2.2 MPa. This is a range of 3.9 MPa. As discussed in the following Section changes in this contact pressure range can be an indicative of process defects.

Evaluating the point of action (POA) of the three parameters in a stamping process can pinpoint the location of process deviations and aid in isolating the cause of the deviation. POA refers to the spatial location where a parameter acts, such as the location of maximum contact pressure on the punch surface etc. The POA of maximum and minimum contact pressure are determined by numerical sorting of the TPS evaluated pressure surfaces. POA of mean pressure is determined in a manner similar to the calculation of center of mass for a solid body. The equations used in its calculation are:

$$x_m = \frac{\int (\int P(x, y) dy) x dx}{\iint P(x, y) dx dy} \quad y_m = \frac{\int (\int P(x, y) dx) y dy}{\iint P(x, y) dx dy} \quad (4.1)$$

When the press force is less than 10% of the full scale value, the significance of the points of action is negligible. Hence, POA have been calculated only at time instants at which the press force is greater than 5% of full scale. This prevents noising of useful data with unnecessary data from the pre-forming stage. Figure 4.20(b) shows the POA for the three parameters. It is observed that the POA of mean contact pressure is concentrated in the center of the range while the POA of maximum pressure acts on the bottom edge and top left corner. Figures 4.21(a) and 4.21(b) show the same information for the binder contact region. The decrease in binder contact pressure caused by increasing punch force is reflected in Figure 4.21(a). Interestingly the POA for binder

mean contact pressure is off centered and traverses towards the corner. Since the maximum contact pressure within the die cavity also acts on the same corner it leads to the conclusion that the clearance between the die and binder-punch arrangement was least in this corner. Under repeated testing the high contact pressure region on this corner becomes much severe and is accompanied by the formation of a crack in that region (corner failure). The details are discussed later in this thesis. The following section discusses the accuracy of contact pressure estimations made by TPS surface method.

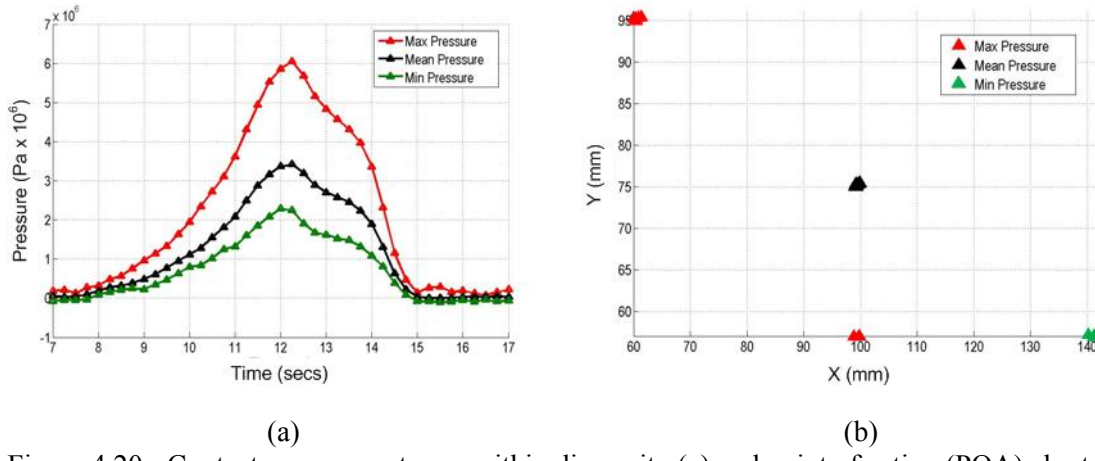


Figure 4.20 - Contact pressure extreme within die cavity (a) and point of action (POA) chart (b)

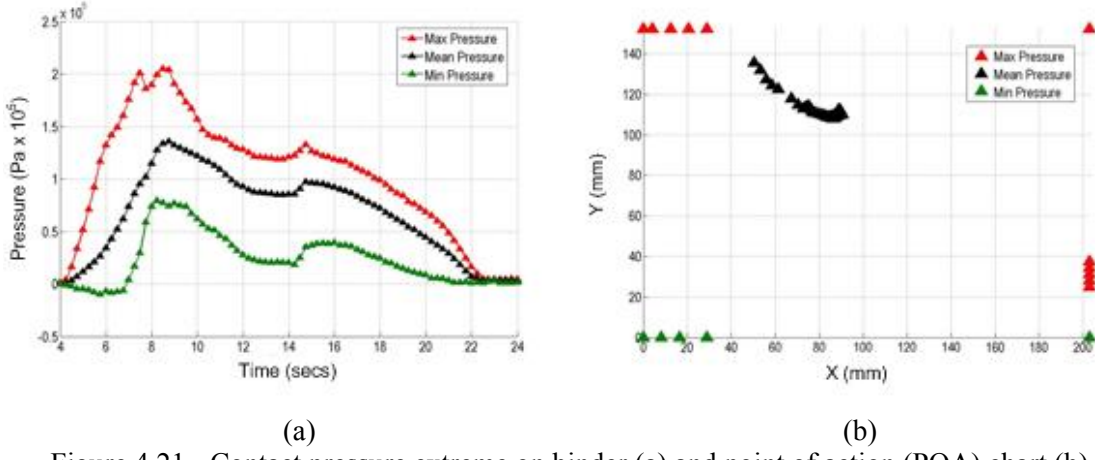


Figure 4.21 - Contact pressure extreme on binder (a) and point of action (POA) chart (b)

#### 4.4.3 Accuracy of Contact Pressure Estimation

The accuracy of TPS surface method in estimating workpiece-die interface contact pressure from spatially discrete sensor measurements has been evaluated by using TPS generated surfaces to predict the contact pressure at sensor sites which did not participate in the surface calculation. To achieve this contact pressure surfaces for the die cavity region were calculated using only measurements from sensors at locations 11, 12, 13, 14, 15, and 16. The contact pressure at the sensor locations 18 and 17 has been estimated using the TPS generated contact pressure surfaces and is compared with the actual sensor measurements, shown in Fig 4.22(a) and 4.22(b) respectively.

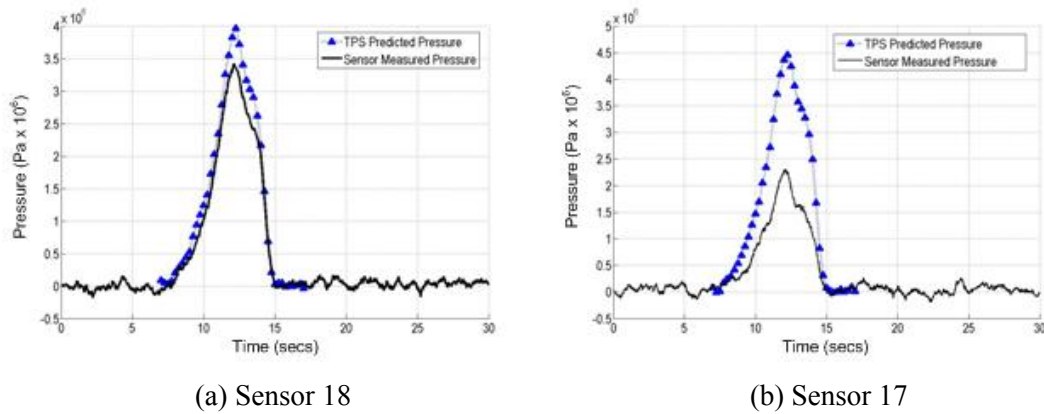


Figure 4.22- Comparison of TPS contact pressure estimate with actual measurements

It is found that at location 18 the estimation error is less than 8% however, at location 17 the estimation error is approximately 54%. This difference is explained based on the location of the sensors with respect to the local extremes in the contact pressure. Figure 4.23(a) and 4.23(b) show the TPS interpolated contact pressure distribution at T=12 seconds calculated with and without including measurements from sensors at location 17 and 18. In the absence of a sensor at location 17 (located at X=81mm, Y=76mm), the TPS surface interpolation scheme estimates a high contact pressure in that region based on the local edge and corner contact pressure maxima

(Figure 4.23(a)). In reality the sensor reading indicates that the contact pressure in that location is much smaller (Figure 4.23(b)). In contrast the contact pressure at sensor location 18 is much more accurately estimated as there is only a single contact pressure maximum in its vicinity. These findings indicate that the estimation error will be greater in the vicinity of local contact pressure maxima or minima. In other words better estimation accuracy can be attained by having smaller sensor interspacing in regions expected to have local contact pressure extremes.

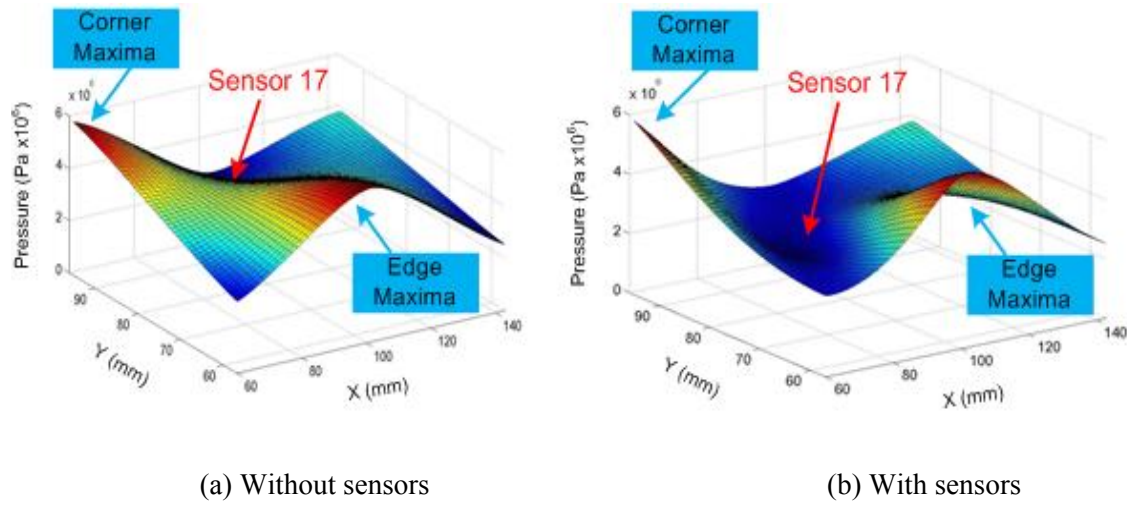


Figure 4.23 - Contact pressure estimate at  $T=12$  secs calculated with and without extra sensors

The accuracy of contact pressure estimation in the binder region has also been evaluated. Contact pressure surfaces for the die cavity region were calculated using only measurements from sensors at locations 1, 4, 6, and 9. The comparison of estimated and actual contact pressure at the sensor locations 2 and 7 is shown in Fig 4.24(a) and 4.24(b) respectively. It is found that the estimation error for sensor locations 2 and 7 is less than 5% and 3% respectively. The improvement in estimation accuracy in contrast to the die cavity contact pressure estimates is explained by the fact that the contact pressure surface for the binder unlike the die cavity contact pressure surfaces has only

one contact pressure maxima. As stated earlier the lack of multiple contact pressure extremes is conducive of more accurate estimates.

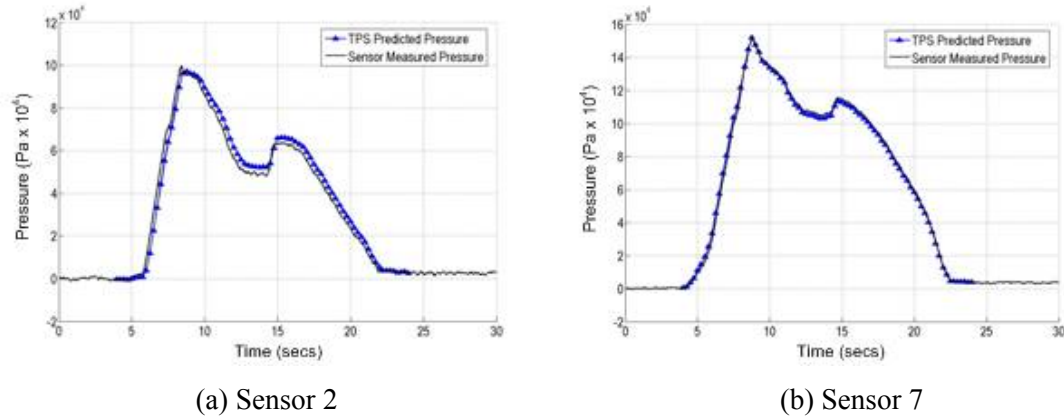


Figure 4.24 - Comparison of TPS contact pressure estimates with sensor measurements

The combined global accuracy of the sensing system and the TPS contact pressure estimation technique vis-à-vis the net binder and die cavity force, has been evaluated by numerically integrating the estimated contact pressure over the contact surface of the binder and the die cavity. This enabled the calculation of the net force acting on the two contact regions at any time. The surface integrated force is determined by the numeric integration of the following expression:

$$F(t) = \sum_{i=1}^n \sum_{j=1}^m P_{i,j}(t) dA(i, j) \quad (4.2)$$

Here  $F(t)$  is the surface integrated contact force (binder or die cavity) at time  $t$ . The constants  $n$  and  $m$  represent the number of divisions into which the die surface is partitioned for numeric integration. The term  $dA(i, j)$  is the area of the surface element at location  $(i, j)$  on the die surface, and  $P_{i,j}(t)$  is the contact pressure acting on the same area element at time  $t$ . It is noted that Eqn. 5 is valid for planar surfaces. For curved surfaces,  $dA(i, j)$  will represent the component of the surface element area at  $(i, j)$ , on a

plane whose normal vector is the direction in which the punch travels. For the calculation of press force from experimental measurements, n and m were taken to be 50. Thus, the total number of area elements involved was 2,500. Figures 4.25(a) and 4.25(b) show the net binder and die cavity forces calculated in this manner.

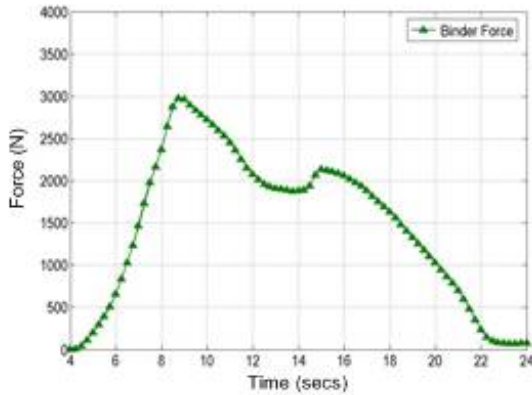


Figure 4.25(a) - Integrated binder force

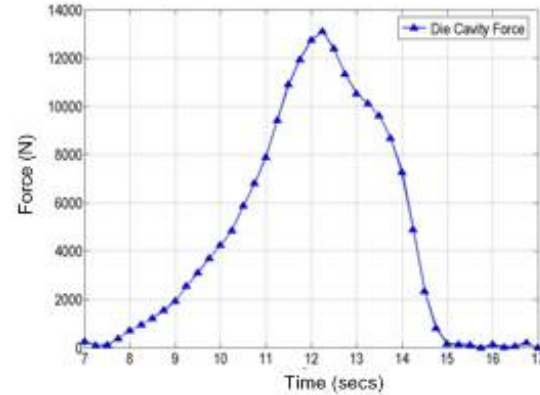


Figure 4.25(b) - Integrated punch force

The global accuracy of the sensing-estimation technique has been estimated by comparing the sum of the binder and die cavity region contact forces with the load cell measured press force. Figure 4.26 shows the load cell measured press force against the sum of the binder and punch forces as estimated by the surface integration. There is a significant difference in the two during the punch down stroke however there is negligible difference during the return stroke. This is contributed to the fact that the plastic deformation of sheet metal workpiece occurs during the down stroke creating large frictional forces on the side walls of the die cavity. These frictional forces by virtue of being parallel to the side wall are a component of the net press force, but on the same time are not measurable by the embedded contact pressure sensors. Installing shear force sensors into the side walls may enable the inclusion of frictional force into

the calculation however as indicated in the literature review previous research in this topic has met with significant difficulties [13].

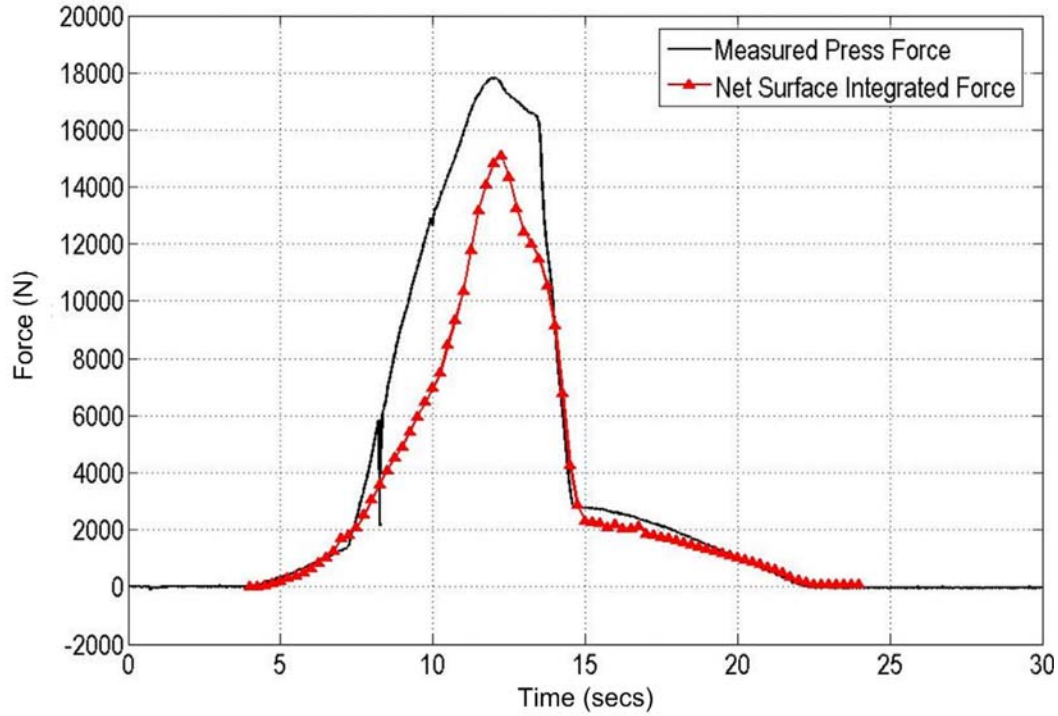


Figure 4.26 - Comparison of press force with net surface integrated force

#### 4.4.4 Contact Pressure Surfaces – Corner Failure

In order to demonstrate the feasibility of using contact pressure surfaces for process defect detection the case of a corner failure defect is presented here. For large panel depths the formed product become inherently susceptible to corner failures, in addition corner defects can also be caused by uneven binder contact pressure distribution. The test case presented here is of a panel with a single corner defect formed during repeated testing on the test bed. The defective product and the crack formation are shown in Figure 4.27. Examining the contact pressure surfaces for the binder contact region (Figure 4.28(b)) reveals little deviation from the binder contact pressure surfaces for a normal process. The contact pressure surfaces of the die cavity contact region (Figure

4.28(a)) exhibit a form similar to the normal process case however, there is an important distinction. The die cavity contact pressure surfaces for the defective panel are much larger in magnitude in comparison to the normal case. Specifically, the vicinity of the panel corner in which the crack developed has elevated contact pressures during the instants the press is at the bottom of its stroke. This region of elevated contact pressure was present in the formation of defect free panel stampings too however in that test the contact pressure was much smaller as compared to the defective case.

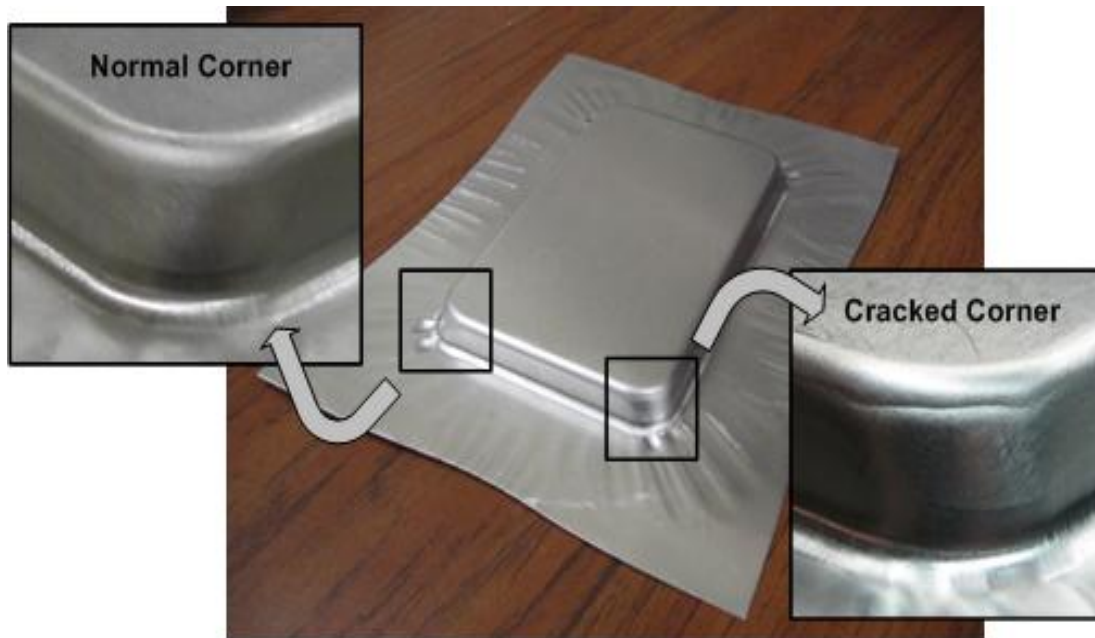


Figure 4.27 - Image of panel with corner defect

The differences between the normal and defective product case are further evaluated by calculation of the minimum, mean and maximum contact pressure parameters. Figure 4.29(a) and 4.29(b) show the value and POA of contact pressure extremes on the binder during the formation of the defective panel. The decrease in binder contact pressure during increasing die cavity contact pressure is much more rapid as compared to the normal panel formation case (Figure (4.28(a))), this could be the affect of the comparatively larger die cavity contact pressure. There is no discernable effect of the

crack formation on the POA chart. Figure 4.30(a) shows the variation in contact pressure extremes within the die cavity during the defect formation. It is seen that the maximum contact pressure in the die cavity is almost 104% greater in magnitude as compared to a normal panel forming case. In addition, at T=13.5 seconds the contact pressure at different points within the die cavity ranges from 1 MPa to 13 MPa i.e. a range of 12MPa which is a 200% increase from the 3.9MPa range observed for normal processes.

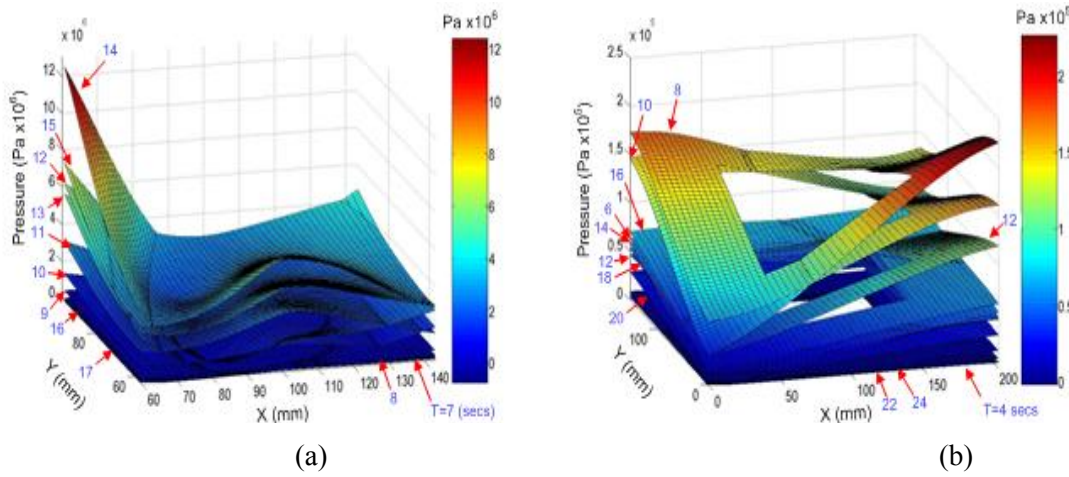


Figure 4.28 - Contact pressure surfaces for sensors within die cavity (a) and on binder (b)

The presence of the spike in maximum contact pressure (at T=14 seconds) during the end of the punch stroke corresponds to the formation of the crack. Once the stress in the corner formation exceeds the yield strength of the material, the resistance of the sheet metal to further deformation is negligible. The sudden decrease in the local resistance to the punch motion allows the punch to come into further contact with the die surface leading to a momentary increase in the maximum contact pressure. Figure 4.30(b) shows the spatial variation in the points of action (POA) of the contact pressure extremes within the die cavity. In comparison to a normal process the POA of mean contact pressure are sparsely distributed and are shifted towards the defective corner. The POA of maximum contact pressure are on the corner and bottom edge. By indexing

the POA with their time of action it was determined that the POA for maximum contact pressure during the momentary spike in contact pressure is concentrated on the top left edge ( $X=60\text{mm}$   $Y=94\text{mm}$ ). From the preceding discussion it is concluded that corner failures can be detected based on the maximum contact pressure and the range of the contact pressure within the die cavity and the POA chart can localize the defect formation.

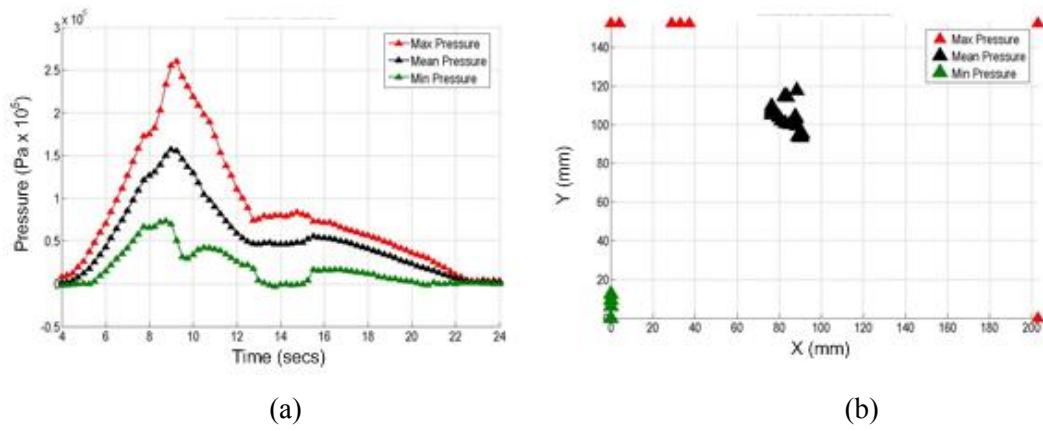


Figure 4.29 - Contact pressure extremes on binder (a) and point of action (POA) chart (b)

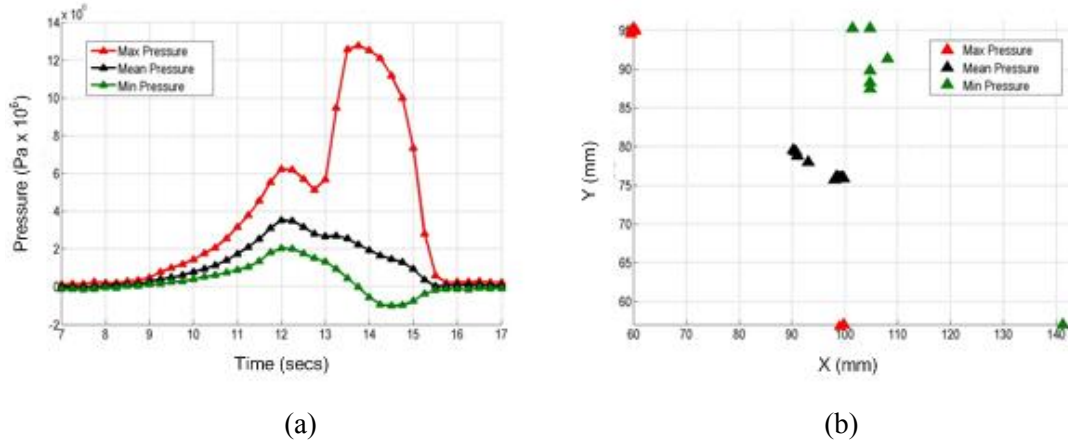


Figure 4.30 - Contact pressure extremes on die cavity (a) and point of action (POA) chart (b)

## CHAPTER 5

### MODELING OF WORKING STRESSES IN STAMPING DIES

#### 5.1 Impact of Embedding Sensors on Die Tool Failure

Embedding sensors under working surfaces of sheet metal stamping tools can cause degradation in the strength of the tools. This could lead to shortened tool life and change in the workpiece surface quality. In this chapter these effects are studied through an axisymmetric finite element model of the sensor cavity. The steady state von Mises stress distribution within the die structure is simulated for different surface loads to investigate the possibility of die failure. The affects of different embedding depths and sensor package materials have also been evaluated.

##### 5.1.1 Finite Element Model of Sensor Cavity

The 2-D axisymmetric model of the sensor used in the finite element simulations is shown in Figure 5.1(a). The model corresponds to the second kind of sensor packaging developed in this work. In the simulations the sensor is embedded into a die structure made of tool steel. This material has been chosen because it is widely used in construction of stamping dies and results based on it shall correspond well with the reality. The die structure has a radius of 30mm and a height of 25mm. The sensor is placed in a blind hole of radius 10mm drilled from the back of the die. The sensor has a radius of 7 mm but only its active sensing region having a radius of 4.75mm has been modeled here. In the figure shown, the blind hole is 23mm deep which results in an embedding depth of the sensor of 2mm. The sensor itself is 0.208mm thick and it is mounted over a support bar made also of tool steel having a 10 mm radius. In the center

of the support bar a set screw is mounted that screws into the die shoe. The purpose of the set screw is to control preload on the sensor. The physical properties used are listed in Table 5.1. Figure 5.1(b) shows the finite element mesh of the package design. The model has been meshed using the element “PLANE183” from the ANSYS element library. This is a higher order 2-D, 8-node element with quadratic displacement behavior which is well suited for modeling irregular meshes. The bottom of the die shoe is fully constrained and axisymmetric conditions are specified. The surface load pressure is applied to the upper surface of the die. Simulations are carried out for 25 MPa, 50 MPa, 75 MPa, and 100 MPa. These surface loads are typical of small, mid range, and large stamping presses. In addition simulations have been run for different embedding depths (2 mm and 4 mm) and for different material properties of the sensor (polystyrene vs. steel). The numeric convergence of the finite element model is achieved by successive mesh refinements. The criterion for numerical convergence is for the sensors measurement of two successive mesh refinements to be within 1% difference. During mesh refinements the element size of the sensor is held constant while the element size for all other components is reduced by 50%. The sensor measurement is found by integrating the surface pressure on the sensing element.

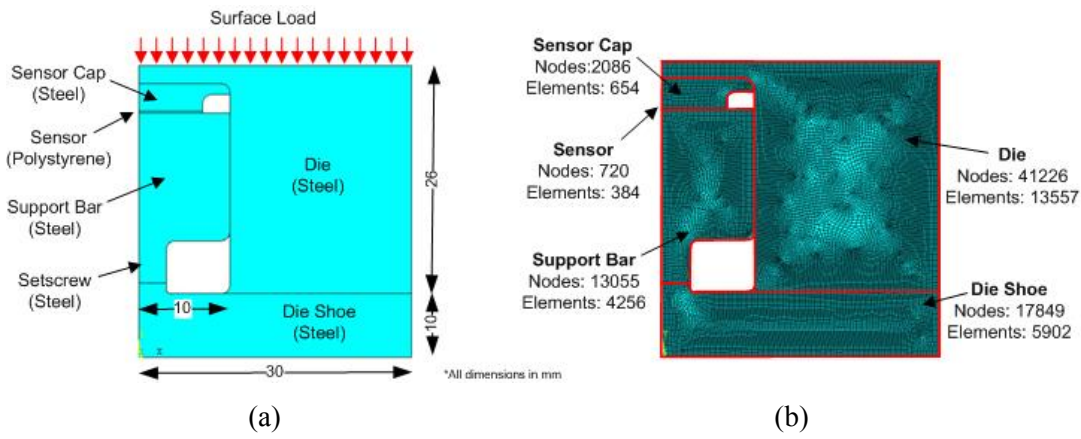


Figure 5.1 – Model of sensor installation and FE mesh

Table 5.1 – Material properties used in sensor cavity simulations

Part	Material	Density (kg/m <sup>3</sup> )	Poisson's Ratio	Elastic Modulus (GPa)	Yield Strength (MPa)
<b>Sensor</b>	Polystyrene	1050	0.33	4	-
<b>All Other Parts</b>	A2 Tool Steel	7750	0.30	190	900

### 5.1.2 Analysis of Stress Distribution in Die Cavity

Figure 5.2 shows the von Mises stress distribution in the die cavity structure for the four different surface loads. The embedding depth in these cases is 2 mm. For each case the design safety factor is calculated as:

$$\text{Safety Factor} = \frac{\sigma_{\text{Steel}}}{\sigma_{\text{Max}}} \quad (5.1)$$

Here,  $\sigma_{\text{Steel}}$  is the yield strength of die steel and  $\sigma_{\text{Max}}$  is the maximum stress experienced at any point by the die structure. The safety factor can have a value of 1 or greater than one. A factor of 1 implies that induced stress is equal to ultimate strength of the material and failure is imminent. The choice of a safety factor is highly dependent on the desired tool life as well as the die designer's personal experience. For the purpose at hand a safety factor of 1.8 and bigger is considered safe. Based on a safety factor of 1.8 if any point in the die structure has a stress of over 495 MPa it is considered to be likely to yield at that point.

Figures 5.2(a) and 5.2(b) corresponding to 75 MPa and 100 MPa surface loads show a maximum stress of 526 MPa and 701 MPa respectively. Based on the said criteria both of these are susceptible to failure. This indicates that installing sensors 2mm below the working surfaces may cause die failure for surface loads over 50 MPa. Figure 5.3

shows the same information for the case of a 4 mm sensor embedding depth. By studying the stress distributions for different loading cases it can be said that the increase in embedding depth reduces the intensity of the stress concentration on the corner. The case of the 100 MPa surface load lies on the boundary of the condition with a factor of 1.8. 100 MPa surface loads are only possible for very large stamping presses typical of armor or hull plate production.

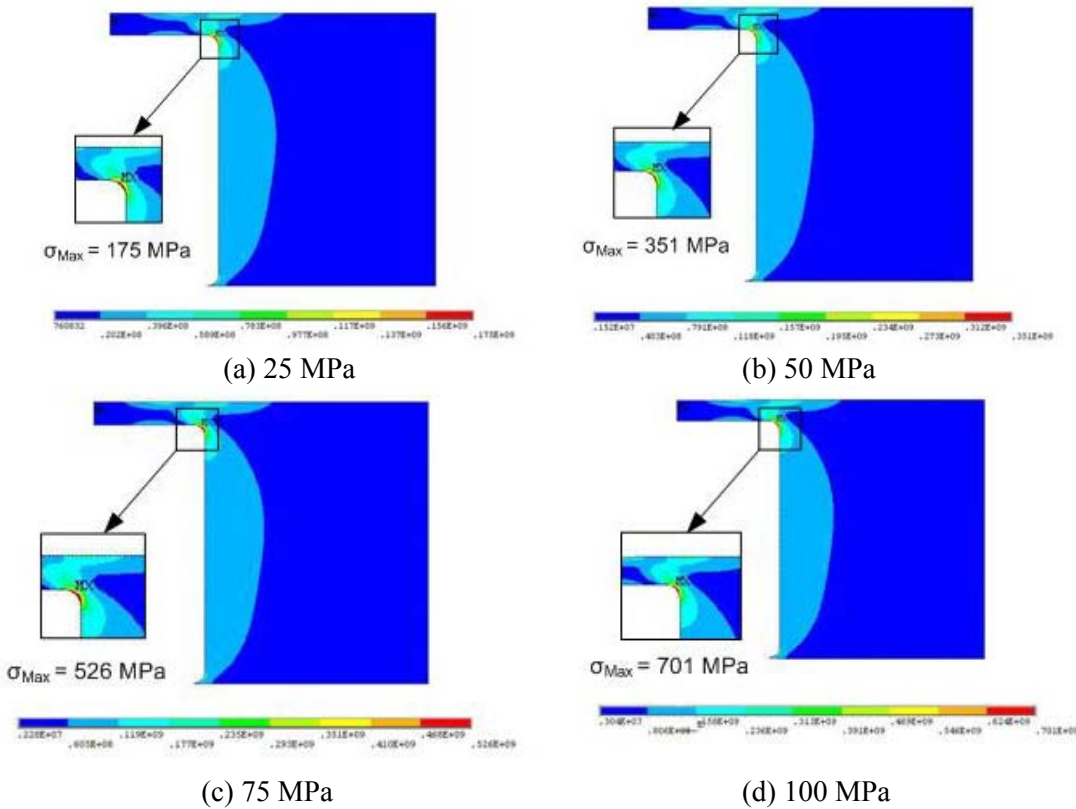
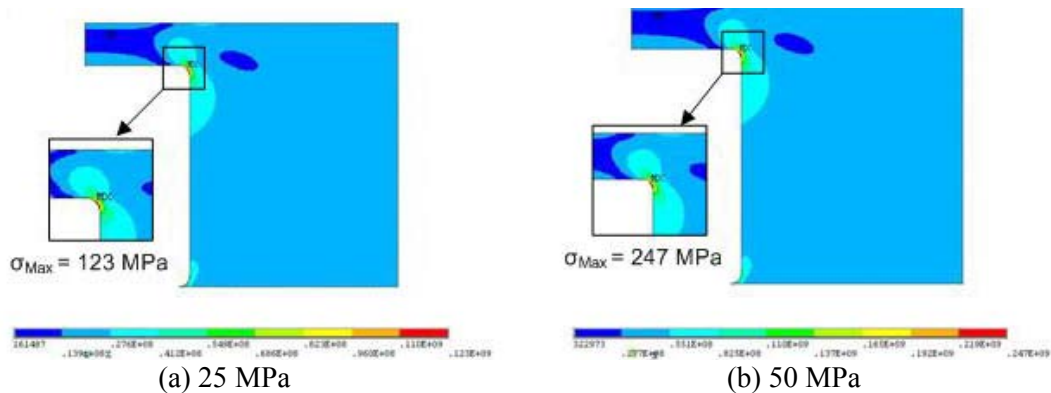


Figure 5.2 – Maximum von Mises stress in 2mm deep die cavity



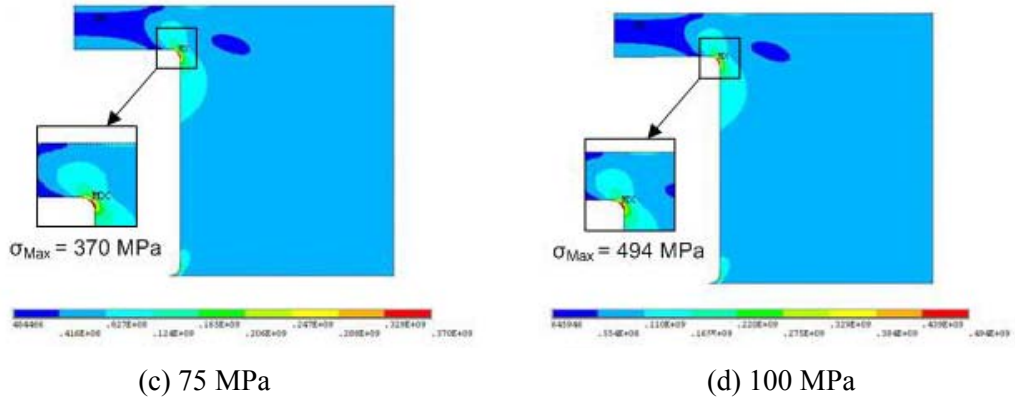


Figure 5.3 – Maximum von Mises stress in 4mm deep die cavity

### 5.1.3 Effect of Rigidity of Sensing Element

Increasing the embedding depth of the sensors beyond 4 mm is not viable because the concomitant loss of sensitivity is too large (over 85% as compared to 2mm depth).

In order to embed sensors in large stamping dies having surface loadings of 75 MPa and higher, the effect of sensor rigidity on die strength has been studied. From the experience gained from the experiments conducted on the different sensor packages it is apparent that the rigidity of the sensor package is directly related to the sensitivity of the embedded contact pressure measurements as well as the strength of the die cavity. To evaluate these effects quantitatively, finite element simulations have been carried out in which the material for the sensing element is steel instead of polystyrene. Figure 5.3 shows the von Misses stress distribution in the die for 25 MPa, 50 MPa, 75 MPa, and 100 MPa surface loads. The maximum stress in the die is much less as compared to simulations having the polystyrene sensing element. However using the same failure criteria as before, the die is found to be susceptible to failure for 75 MPa and 100 MPa loads. Figure 5.5 shows the same information for the 4 mm sensor embedding depth. It is seen that the die can operate safely at surface loads up to 100 MPa with sensors embedded 4 mm below the surface. The results are summarized in Table 5.2.

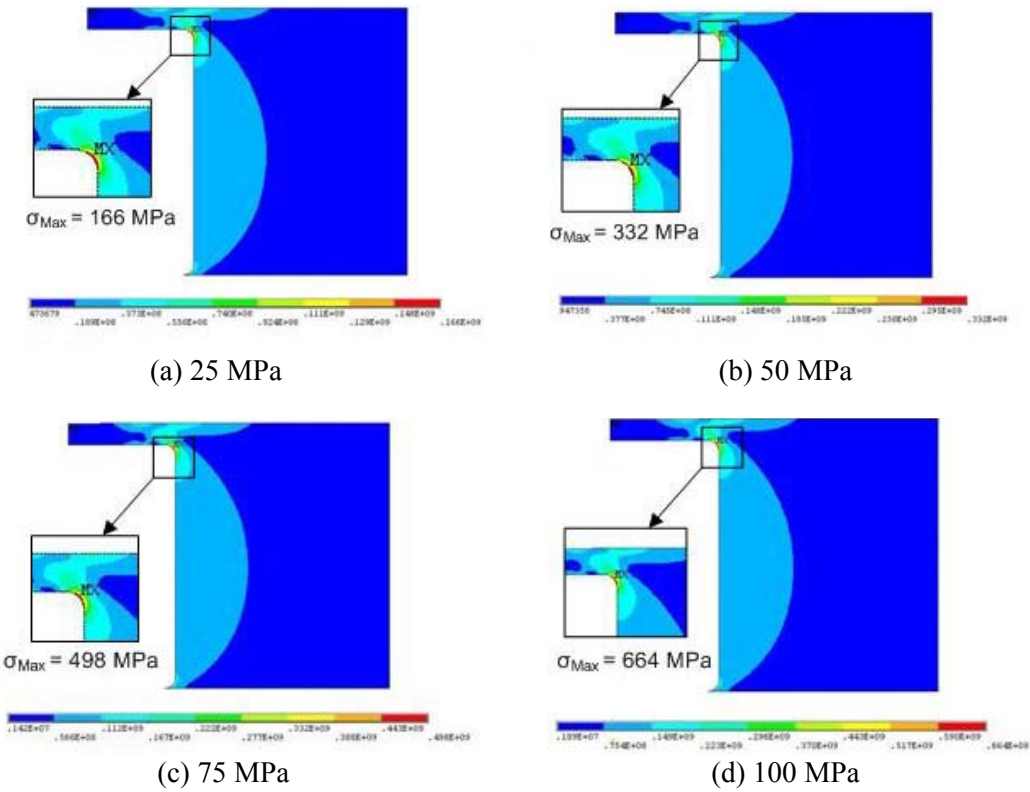


Figure 5.4 – Maximum von Mises stress in 2mm deep die cavity

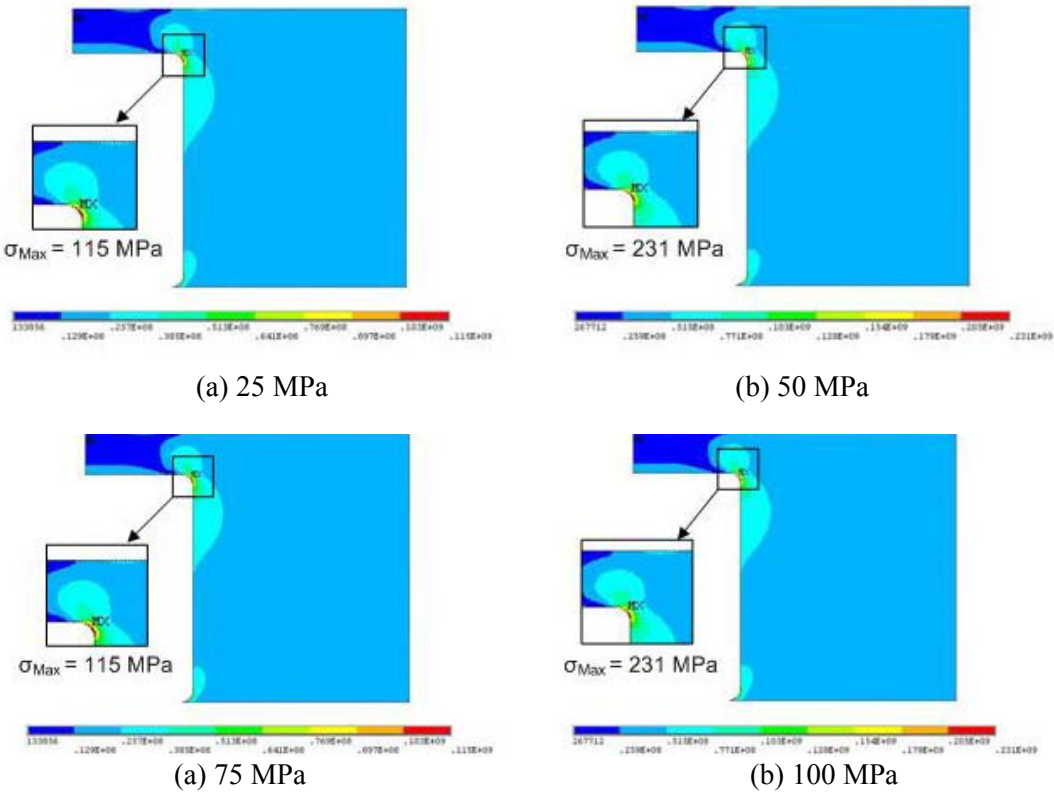


Figure 5.5 – Maximum von Mises stress in 4mm deep die cavity

Table 5.2 – Safety factor for different surface loads and embedding depths

Sensor Material	Depth	25 MPa	50 MPa	75 MPa	100 MPa
Polystyrene	2 mm	5.00	2.56	1.69	1.28
	4 mm	7.14	3.70	2.43	1.80
Steel	2 mm	5.55	2.70	1.80	1.35
	4 mm	7.69	3.85	2.56	1.96

LEGEND       Safe       Possible Failure

#### 5.1.4 Fatigue Life Analysis of Sensor Cavity

During its life cycle the die is loaded and unloaded many thousand times this makes it very susceptible to fatigue failure. The inspection of the safety factor can only provide qualitative assistance in designing the sensor cavity structure against fatigue failure. For a quantitative approach the expected life of the die with respect to fatigue failure in the sensor cavity corner (which as seen before has the maximum stress concentration) has been predicted in terms of number of loading and unloading cycles. This section presents the mathematical analysis used for the life expectancy prediction and the results obtained [29].

The first step in the estimation of fatigue life is the calculation of the materials endurance limit ( $S'_e$ ), the prime mark indicates that the limit is for a rotating beam tensile specimen of the material. For Steel with ultimate tensile strength less than 1460 MPa this can be calculated by the following expression:

$$S'_e = 0.506 \overline{S_{ut}} \text{LN}(1, 0.138) \quad \overline{S_{ut}} \leq 1460 \text{ MPa} \quad (5.2)$$

Here  $\overline{S_{ut}}$  is the mean ultimate tensile strength for the material and  $\text{LN}(1, 0.138)$  is a unit lognormal variate with a mean of 1 and a standard deviation of 0.138. The next step

is the calculation of endurance limit for the sensor cavity corner in question ( $S_e$ ). It is evaluated by the Marin equation [30]:

$$S_e = k_a k_b k_c k_d k_e S'_e \quad (5.3)$$

Where  $k_a$  = surface condition modification factor

$k_b$  = size modification factor

$k_c$  = load modification factor

$k_d$  = temperature modification factor

$k_e$  = miscellaneous effects modification factor

$S'_e$  = rotary beam endurance limit

In the current application, as the strength is being evaluated at room temperature, the loading is normal to die surface, and there are no miscellaneous effects hence:

$$k_b = k_d = k_e = 1 \quad (5.4)$$

The surface condition modification is evaluated by the expression:

$$k_a = a \bar{S}_{ut}^b \text{LN}(1, C) \quad (5.5)$$

Here, the condition of the die and sensor cavity surfaces decides the values of constants a, b, and C. For smooth ground surface these values are:

$$a = 1.58 \quad b = -0.86 \quad C = 0.120 \quad (5.6)$$

Considering the die surface to be axially loaded load modification factor is known to be:

$$(k_c)_{\text{axial}} = 1.23 \bar{S}_{ut}^{-0.0778} \text{LN}(1, 0.125) \quad (5.7)$$

On putting together all the given data the value of endurance limit for the sensor cavity corner is found to be:

$$S_e = 292.55 \text{LN}(1, 0.224) \text{ MPa} \quad (5.8)$$

The physical significance of this value is that if the cyclic loading of the die induces a corner stress of less than 292.55 MPa than the die will probably fail due to reasons

other than fatigue. In order to use the endurance limit to predict fatigue life expectancy for surface loading which induces corner stresses exceeding the endurance limit it is necessary to evaluate the fatigue strength coefficient ( $\sigma'_F$ ). In the present application this can be done using the SAE approximation for steels [31]:

$$\sigma'_F = S_{ut} + 345 \text{ MPa} \quad (5.8)$$

The calculated value of 1245 MPa for the fatigue strength coefficient allows the calculation of intermediate variables  $a$ ,  $b$ , and  $f$  using the following equations:

$$b = -\frac{\log(\sigma'_F / S_e)}{\log(2 \times 10^6)} \quad (5.9)$$

$$f = \frac{\sigma'_F}{S_{ut}} (2 \times 10^3)^b \quad (5.10)$$

$$a = \frac{f^2 S_{ut}^2}{S_e} \quad (5.11)$$

Physically  $f$  is fatigue strength corresponding to  $10^3$  cycles of operation. By using Eqn. 5.9 through 5.11 the values of  $a$ ,  $b$ , and  $f$  were determined to be:

$$b = -0.10 \quad f = 0.647 \quad a = 1158.59 \text{ MPa} \quad (5.12)$$

The life expectancy for a given loading condition provided that the failure occurs due to fatigue in the sensor cavity corner is estimated based on the intermediate variables by the following expression:

$$N = \left( \frac{\sigma_a}{a} \right)^{1/b} \quad (5.13)$$

Here  $\sigma_a$  is the amplitude of the stress acting at the point of interest. If  $\sigma_{\max}$  and  $\sigma_{\min}$  are the maximum and minimum stresses at the point of interest,  $\sigma_a$  can be determined as:

$$\sigma_a = \left| \frac{\sigma_{\max} - \sigma_{\min}}{2} \right| \quad (5.14)$$

For the case at hand as there is no reversal of surface loading  $\sigma_{\min}$  is zero and  $\sigma_a$  becomes half of  $\sigma_{\max}$ . A fully analytic determination of fatigue life involves the calculation of stress concentration factors to improve the estimation of stresses in corners or notches. In the present method the stress concentration has been accurately determined using the Finite Element model of the sensor cavity. Hence the need for stress concentration factors has been eliminated. Table 5.3 lists the life expectancy (in number of product stamped) for the various sensor cavity conditions previously discussed. The three color codes classify the life expectancy in terms of the standard terminology used for fatigue life. 1 to  $10^3$  load cycle life is called low cycle life. If a failure occurs before  $10^6$  cyclic loads the part is said to have a finite life, else it is said to have an infinite life. The cases found to be likely to suffer failure using the safety factor (Table 5.3) are seen to have low cycle life expectancy. The life expectancy is seen to increase with higher embedding depth as well as for sensors having higher rigidity.

Table 5.3 – Life expectancy (Number of product stamped)

S. Material	Depth	25 MPa	50 MPa	75 MPa	100 MPa
Polystyrene	2 mm	$1.6 \times 10^8$	$1.5 \times 10^5$	$2.6 \times 10^3$	X
	4 mm	$5.5 \times 10^9$	$5.1 \times 10^6$	$9.0 \times 10^4$	$4.7 \times 10^3$
Steel	2 mm	$2.7 \times 10^8$	$2.6 \times 10^5$	$4.6 \times 10^3$	X
	4 mm	$1.0 \times 10^{10}$	$1.0 \times 10^7$	$1.7 \times 10^5$	$1.0 \times 10^4$

LEGEND



Infinite  
Life



Finite Life



Low  
Cycle

## 5.2 Effect of Die Material on Embedded Sensor Measurements

The Finite Element model of the die cavity developed in the previous section has been used to study the effect of different embedding materials on the sensitivity of embedded force sensors. Specifically, it is desired to estimate sensor measurements for various surface loads in the case of AL6061 which was used in the experimental study and Tool Steel which is a material commonly used in the fabrication of sheet metal stamping dies.

Simulations were carried out for determining the contact pressure distribution on the sensing element in the case of 2 mm and 4 mm embedding depths during different surface loads. The contact pressure distribution was integrated over the area of the sensing element to calculate the force acting on the sensor. Figure 5.6 shows the simulated sensor measurements for 2 mm and 4 mm embedding depths and the effect of different die materials as well. It is seen that for a given depth and die material there is a linear relationship between the applied surface contact pressure and the force acting on the sensing element. Further more there is a definable relationship between the forces acting on two sensors embedded at the same depth in different mediums. In context of the stamping test bed this means that the experimental measurements can be used to estimate the sensor readings for a similar setup constructed of steel.

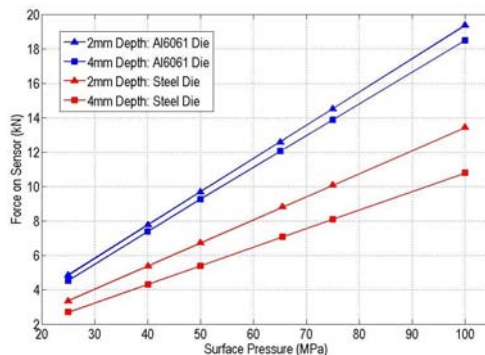


Figure 5.6 – Simulated sensor measurements

## CHAPTER 6

### CONCLUSION

#### **6.1 Summary**

The ultimate goal of this work is to improve the observability and diagnosability of the stamping operation through tooling integrated sensing. The focus of this thesis is the evaluation of contact pressure distribution on stamping dies from spatially distributed sensor readings by use of numerical surface techniques. Towards this end, the thesis examines the issues involved in embedding sensors under stamping tooling surfaces, using the embedded sensors to accurately estimate the contact pressure distribution, and in the possible applications of the contact pressure estimates in defect detection.

Chapter 1 first established a background on the stamping operation this was followed by a review of the state of knowledge in sensing technology for stamping operations. Relevant past work in the fields of embedded sensing, and Spatio-Temporal contact pressure reconstruction has also been discussed. Based on the information presented, the motivation and potential benefits of an embedded contact pressure sensing in stamping operations are presented.

At an initial data gathering stage Finite Element Models of a stamping operation were created to estimate contact pressure distributions on the workpiece-die interface. This information is presented in Chapter 2. The elements, materials, and constraints used are discussed and justification is presented for the assumptions made. Numerical convergence of the workpiece-die contact pressure field is shown as proof of model

reliability. The chapter discusses the contact pressure distributions determined by the 2D and 3D simulations and their impact on the design of embedded sensor packages.

Chapter 3 presents the mathematical background for Bezier Surface and Thin Plate Spline based surface generation. The defining equations for Bezier Surface method are also presented in a Matrix formulation for computational purpose. Based on the contact pressure distributions evaluated by Finite Element models in Chapter 2, the accuracy of contact pressure estimation by the two techniques is discussed. The study indicates that the Thin Plate Spline based surface generation method can estimate contact pressure distributions more accurately as compared to Bezier Surface method.

Chapter 4 presents the design and calibration of the two sensor packages developed for testing. The effect of embedding depth on the sensitivity of the package as evaluated by experiments has been presented. It is found that for a given embedding depth the sensitivity to different surface loads is linear however sensitivity was found to decrease nonlinearly with increased embedding depth. Contact pressure estimation was carried out on experimental measurements from an array of force sensors mounted flush on the surface of an impact plate. The validity of the contact pressure surface was evaluated by comparing the net contact force (measured externally) with the contact force estimated by integration of the contact pressure surface over the contact region. The effect of slide parallelism defect was recreated by introducing angular deviations in the contact surface alignments and measuring the concomitant contact pressure profile. Chapter 4 also presents the design of a panel stamping test bed instrumented with an array of force sensors. It was used to measure the contact pressure profile during stamping of aluminum sheets. The results show the possibility of predicting corner failure defects.

The effect of embedding sensors on die strength has been evaluated using Finite Element models of the sensor cavity in Chapter 5. The effect of embedding depths and rigidity of sensing element on die strength has been studied. The FEA results have been used to predict the life of the die against fatigue failure. Results indicate that with higher sensor rigidity and embedding depths it is possible to minimize the weakening of sensor cavities on the die strength. The same Finite Element is used further to investigate the scalability of experimental results based on a aluminum (AL6061) die punch setup (reported in Chapter 4) to a tool steel setup. It is determined that the Aluminum based experimental results are directly related to the expected results from a Tool Steel die.

## **6.2 Intellectual Contribution**

Significant progress has been made on a number of issues leading towards the ultimate goal of improving the observability of the stamping process. The intellectual contribution and broader impact of this research is summarized below:

- 1) A new sensing methodology has been proposed for stamping process monitoring by means of an array of tooling embedded force sensors. The availability of information of local forming events by means of distributed sensing provides a new means of carrying out defect detection and process monitoring. Such distributed sensing systems overcome the limitations of traditional sensing systems such as tonnage and acceleration which are focused on spatially aggregate parameters.
- 2) The new sensing method is based on the evaluation of spatially continuous pressure surfaces from discrete sensor measurements. Towards this purpose the possibility of using numerical surface generation methods in estimating contact pressure distribution on working surfaces of stamping dies has been evaluated. With the aid of Finite Element models it has been shown that interpolative surface generation methods estimate contact pressure distributions more accurately as compared to approximate surface generation methods. The potential impact of these results goes well beyond the scope of stamping process monitoring and is pertinent to any application requiring accurate estimation of a spatially continuous variable from discrete measurements.
- 3) A stamping test bed embedded with an array of force sensors has been designed, fabricated, and experimentally tested. The test bed can reproduce a number of stamping defects, such as slide non-parallelism, shut height variations, die misalignment, and variations in binder pressure distribution. Experiments conducted on the test bed show

that slide parallelism defects and corner failures are accompanied by changes in the contact pressure distribution over the workpiece-die contact. Furthermore these pressure distributions have an observable pattern which has potential applications in defect detection. Even more importantly the results point towards the possibility of predicting the onset of defects based on the evaluation of contact pressure surfaces for operations leading up to the stamping operation in which a defect develops.

4) A Finite Element model of the stamping process has been developed for analyzing the contact pressure distribution during a stamping operation. It has been utilized for evaluating the accuracy of different numerical surface generation methods. Analyzing the contact pressure within a stamping setup by FE modeling and comparing them with contact pressure distributions determined from sensors embedded in actual stamping dies can provide insights into making FE models more realistic and hence increase the confidence that die designers put in them. Specifically, contact pressure sensing can improve the effectiveness of current contact modeling techniques.

5) Defect detection based on spatio-temporal decomposition of contact pressure surfaces into maximum, minimum, and mean pressure based parameters has also been studied in this work. Slide parallelism and corner failure defects were found to affect the magnitude and position of maximum contact pressure. Most stamping defects are expected to affect these parameters in some similar manner. This indicates that the analysis of contact pressure surface based parameters can be useful in detecting the formation of many types of stamping defects. Theoretically by tracking gradual changes, over many stamping cycles, in the position and magnitude of these parameters it would even be possible to predict the formation of such defects beforehand.

### 6.3 Future Work

In addition to the results obtained during the course of the dissertation work, some other aspects of the present research topic came to light. These aspects listed below will be the avenue of continued research on this topic.

#### 6.3.1 Sensor Package

During the experimental and simulation studies conducted, two possible improvements in the sensor packaging and installation have come to light. The first improvement came into attention during the experimental calibration of the sensor package and the need was reaffirmed by the Finite Element Simulations conducted in Chapter 5. It was found that having a sensing element with high rigidity (large Elasticity modulus) will be more sensitive embedded applications. In addition it will reduce the build up of stress concentrations in the sensor cavity corner. The second improvement has to do with the shape of the sensor cap. As seen in Chapter 5 stress distributions in all the sensor cavity simulations have a common attribute which is the build up stress concentration on the corner of the die cavity. The implementation of a hemispherical top cap will eliminate this stress concentration. These two possibilities will be examined in the future extension of this work.

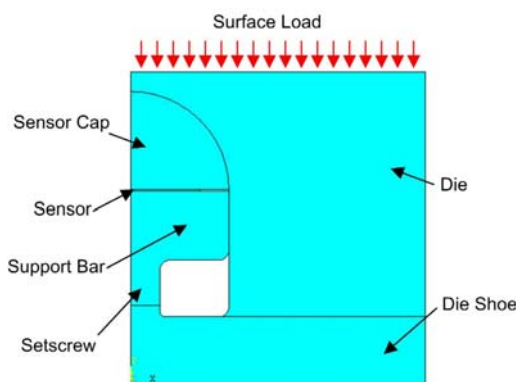


Figure 6.1 – Concept sketch for hemispherical top cap

### **6.3.2 Self Energized Wireless Sensing**

A major constraint in embedding sensors under working surfaces of stamping dies is the design and fabrication of pathways for wires connecting the die embedded sensors to a data acquisition board. Because of the nature of stamping dies there will be significant costs involved in the machining of these pathways in addition to the weakening effect of the pathways on die strength. For these reasons a self energized sensor with wireless communication would be highly desirable in such scenarios. The design of one such sensor [17] for measuring polymer melt pressure in injection molding process consists of a stack of piezoelectric discs to generate electrical charges in response to polymer melt exerted contact pressure. A threshold modulator releases the charges accumulated to a secondary ultrasound transmitter when the voltage on a parallel capacitor exceeds a predetermined quantity. The charge pulse in turn generates a train of ultrasound pulses that travel through the mold to a receiver mounted on the outside of the mold. By counting the number of “pings” from the received ultrasound pulse trains, the melt pressure can be reconstructed in a mechanically digitized form. Much research will be required before a similar idea can be developed for stamping operation monitoring. The sensor will need to be suited for measuring larger loading at higher loading rates as compared to the injection molding design this will involve the development of a package for the piezo stack with very high stiffness. Designs for measuring force unloading as well as loading will also need to be investigated. The key considerations in the design of a wireless sensor would be power output of the stack, transmission losses as the ultrasonic pulse travels through the die material, and the response time of the sensor.

### **6.3.3 Computational Efficiency of Surface Generation Methods**

There are two topics pertaining to the generation of Thin Plate Spline based contact pressure surfaces that need further investigation. The first among them is the effect of number of grid points on the overall utility of contact pressure surfaces for die design, process planning and defect detection. The second topic is the investigation of computational load caused by introduction of additional grid points. The optimum number of grid points for robust defect detection while insuring the on-line applicability of the scheme bears investigation. A possible method for testing the robustness of the pressure surface with regards the number of constitutive data points can be based on the evaluation of error in estimating the net press force.

### **6.3.4 Structured Defect Detection**

The thesis presents experimental results on the effect of slide parallelism and corner defects. The experimental test bed designed can be used in a similar fashion to investigate other common stamping failures such as flange wrinkling and workpiece thickness variation. A comprehensive database of failure related contact pressure surfaces can be built to aid in future work on the subject.

The most important extension of this work would be the design of a structured method for detecting the formation of defects based on gradual or rapid changes in the contact pressure distribution variation in comparison to pressure variations expected in a defect free process. Such a spatio-temporal parameter based method may be able to predict the formation of defects before they actually form, thus having a significant impact on the sheet metal stamping industry.

## APPENDIX: ELEMENT FORMULATION

**Element Formulation:** BELYTSCHKO-LIN-TSAY, BELYTSCHKO-WONG-CHIANG

**Element:** SHELL163\*

The 3D Finite Element models used in this work utilize the SHELL163 element having the Belytschko-Lin-Tsay element formulation from the ANSYS-LSDYNA explicit elements library. This particular element formulation type has been chosen because it is much more computationally efficient in comparison to other shell element formulations in its class. For instance for a five through the thickness integration points the Belytschko-Lin-Tsay element formulation requires 82% less number of mathematical operations in comparison to the popular Hughes-Liu element. Though the formulation does not pass the patch test testing has shown that it yields results comparable to those from the Hughes-Liu formulation.

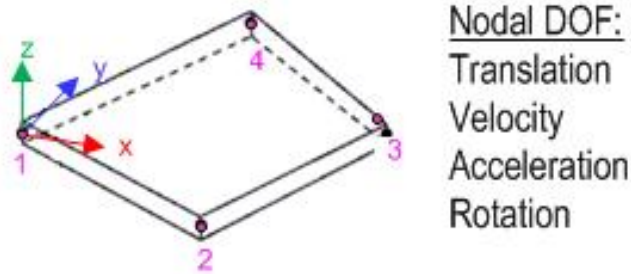


Figure A – SHELL163

The efficiency of the Belytschko-Lin-Tsay element is a result of the mathematical simplifications concomitant of two kinematic assumptions made in its formulation. These assumptions are:

Co-rotational formulation

Velocity Strain formulation

\*ANSYS-LSDYNA Theoretical Manual

The co-rotational formulation avoids the non-linear mechanics complexities by embedding an element coordinate system that deforms with the element, into the element itself. The velocity strain formulation aids in the constitutive evaluation, as the conjugate stress is the more familiar Cauchy stress.

### **Co-rotational Coordinates<sup>[1]</sup>**

The procedure for constructing the co-rotational coordinate system in terms of three unit vectors  $(\hat{e}_1, \hat{e}_2, \hat{e}_3)$  is demonstrated here. First the diagonals  $r_{31}$  and  $r_{42}$  are determined from the node positions (Figure B). The first unit vector is determined as being normal to the diagonals as:

$$\hat{e}_3 = \frac{s_3}{\|s_3\|}$$

Here,  $S_3$  is determined by the cross product of the of the element diagonals:

$$s_3 = r_{31} \times r_{42}$$

The second elemental direction is established approximately along the element edge between nodes 1 and 2 according to the following equations:

$$s_1 = r_{21} - (r_{21} \cdot \hat{e}_3) \hat{e}_3$$

$$\hat{e}_1 = \frac{s_1}{\|s_1\|}$$

The final unit vector is obtained as the cross product of the first two unit vectors to determine the orthogonal coordinate system.

$$\hat{e}_2 = \hat{e}_3 \times \hat{e}_1$$

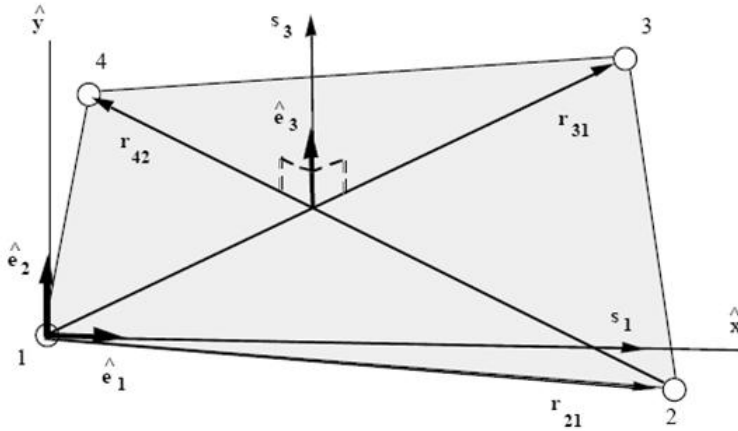


Figure B – Element coordinate system<sup>[1]</sup>

The transformation matrix between global and local element coordinate system is definable as:

$$\{A\} = \begin{pmatrix} A_x \\ A_y \\ A_z \end{pmatrix} = \begin{pmatrix} e_{1x} & e_{2x} & e_{3x} \\ e_{1y} & e_{2y} & e_{3y} \\ e_{1z} & e_{2z} & e_{3z} \end{pmatrix} \begin{pmatrix} \hat{A}_x \\ \hat{A}_y \\ \hat{A}_z \end{pmatrix} = [\mu] \{\hat{A}\}$$

Here,  $\{A\}$  is global coordinate vector,  $\{\hat{A}\}$  is the vector position of the same point in the elemental coordinate system, and  $e_{ix}, e_{iy}, e_{iz}$  are the global components of the element coordinate system.

### **Velocity- Strain Displacement Relations<sup>[1]</sup>**

The displacement and velocity on any point on the shell is partitioned into a midsurface velocity and an angular velocity vector according to the Mindlin theory of plates and shells as given in the following equation:

$$v = v^m - \hat{z} e_3 \times \theta$$

Here,  $v^m$  is midsurface velocity,  $\theta$  is the angular velocity vector, and  $\hat{z}$  is the distance along the fiber direction (thickness) of the shell element. The co-rotational components of the strain rate are given by:

$$\hat{d}_{ij} = \frac{1}{2} \left( \frac{\partial \hat{v}_i}{\partial \hat{x}_j} + \frac{\partial \hat{v}_j}{\partial \hat{x}_i} \right)$$

These two equations jointly give the velocity strain relationships which are evaluated at the quadrature points through the shell thickness.

### Shape Functions<sup>[1]</sup>

The formulation uses bilinear nodal interpolation to define midsurface velocity, angular velocity and element coordinates according to isoparametric representation. The shape functions are:

$$N_1 = \frac{1}{4}(1-\xi)(1-\eta)$$

$$N_2 = \frac{1}{4}(1+\xi)(1-\eta)$$

$$N_3 = \frac{1}{4}(1+\xi)(1+\eta)$$

$$N_4 = \frac{1}{4}(1-\xi)(1+\eta)$$

The parameters  $\eta$  and  $\xi$  are zero at the center of the element. The midsurface velocity, angular velocity and the elements coordinates are then given by:

$$v^m = N_I(\xi, \eta) v_I$$

$$\theta^m = N_I(\xi, \eta) \theta_I$$

$$x^m = N_I(\xi, \eta) x_I$$

Here, subscript I indicate summation over all the elements nodes. The nodal velocities are obtained from differentiating the nodal coordinates against time and the stress field is calculated from the strain field.

## BIBLIOGRAPHY

- [1] Suchy, I., “*Handbook of die design*”, 2<sup>nd</sup> Edition, Mc Graw Hill, New York, 2006.
- [2] American Society of Tool and Manufacturing Engineers, “*Die design handbook*”, Mc Graw Hill, New York, 1965.
- [3] Koyama, H., Wagoner, R.H., and Manabe, K., “*Workpiece holding force in panel stamping process using a database and FEM-assisted intelligent press control system*”, Journal of Materials Processing Technology, Vol. 152, pp. 190-196, 2004.
- [4] Koyama, H., Manabe K., and Yoshihara, S., “*FEM-assisted fuzzy adaptive workpiece holder control approach for sheet stamping process*”, Manufacturing Engineering Division, American Society of Mechanical Engineers, Vol. 11, pp. 805-810, 2000.
- [5] Ahmetoglu, M.A., Altan, T., and Kinzel, G.L., “*Improvement of part quality in stamping by controlling workpiece-holder force and contact pressure*”, Journal of Materials Processing Technology, Vol. 33, Issue 1-2, pp. 195-214, 1992.
- [6] Blumel, K.W., Hartmann, G., and Lubeck, P., “*Variations of the stamping process*”, 15<sup>th</sup> Biennial Congress of The International Deep Drawing Research Group, pp. 9-16, Dearborn, Michigan, 1988.
- [7] Doolan, M.C., Kalyanasundaram, S., Hodgson, P., and Cardew, H.M., “*Identifying variation in sheet metal stamping*”, Journal of Materials Processing Technology, Vol. 115, pp. 142-146, 2001.
- [8] Shi, J., and Jin, J., “*Press tonnage signal decomposition and validation analysis for transfer or progressive die processes*”, ASME Journal of Manufacturing Science and Engineering, Vol. 127, No. 1, pp. 231-235, 2002.
- [9] Du, R., and Xu, Y.S., “*A review on the sensing and on-line monitoring of sheet metal stamping operations*”, Proceedings of The 5<sup>th</sup> International Conference on Frontiers of Design and Manufacturing, pp. 412-420, Dalian, 2002.
- [10] Breitling, J., Wallace, D., and Altan, T., “*Investigations of different loading conditions in a high speed mechanical press*”, Journal of Materials Processing Technology, Vol. 59, Issue 1-2, pp. 18-23, 1996.
- [11] Zhang, G.C., Ge, M., Tong, H., Xu, Y., and Du, R., “*Bispectral analysis for on-line monitoring of stamping operation*”, Engineering Applications of Artificial Intelligence, Vol. 15, pp. 97-104, 2002.

- [12] Harry, Y.M., Maolin, Y., Huang, Y., and Du, R., “*Diagnosis of sheet metal stamping processes based on thermal energy distribution*”, Proceeding of the 2005 IEEE Conference on Automation Science and Engineering, pp. 191-196, Edmonton, 2005.
- [13] Li, M., Klamecki, B.E., and Weinmann, K.J., “*SN-gage and instrumented pin: to measure shear and normal tool forces in sheet metal forming*”, Transactions of North American Manufacturing Research Institution/Society of Manufacturing Engineers, Vol. 20, pp. 103-109, 1992.
- [14] Kernosky, S.K., Weinmann, K.J., Michler, J.R., and Kashani, A.R., “*Development of a die shoulder force transducer for sheet metal forming research*”, Journal of Manufacturing Science and Engineering, Vol. 120, pp. 42-48, 1998.
- [15] Du, H., and Klamecki, B.E., “*Force sensors embedded in surfaces for manufacturing and other tribological process monitoring*”, Journal of Manufacturing Science and Engineering, Vol. 121, pp. 739-748, 1999.
- [16] Hanchi, J., Li, M., and Klamecki, B.E., “*Sensing of interface loads in manufacturing processes*”, Tribological Aspects in Manufacturing, American Society of Mechanical Engineers, Vol. 2, pp. 203-216, 1991.
- [17] Zhang, L., Theurer, C.B., Gao, R., and Kazmer, D.O., “*A self-energized sensor for wireless injection mold cavity contact pressure measurement: design and evaluation*”, Journal of Dynamic Systems, Measurement, and Control, Vol. 126, pp. 309-318, 2004.
- [18] Du, R., Guo, W.Z., Xu, D., and Liasi, E., “*Snake skeleton graph: a new method for analyzing signals that contain spatial information,*” Transactions of the ASME, Journal of Dynamic System, Measurement and Control, Vol. 125, pp. 294-302, 2003.
- [19] Weili, X., Huibao, W., Yuying, Y., and Wang, Z.R., “*A simplified method of wrinkling simulation*”, Journal of Materials Processing Technology, Vol. 121, pp. 19-22, 2002.
- [20] Cao, J., and Boyce, M.C., “*Wrinkling behavior of rectangular plates under lateral constraint*”, International Journal of Solids and Structures, Vol. 34, No. 2, pp. 153-176, 1997.
- [21] Cao, J., and Wang, X., “*An analytical prediction of flange wrinkling in sheet metal forming*”, Journal of Manufacturing Processes, Vol. 2, No. 2, pp. 100-107, 2000.
- [22] Bezier, P.E., “*Numerical control mathematics and applications*”, John Wiley & Sons, London, 1972.

- [23] Gordon, W.J., and Riesenfeld, R.F., “*Bernstein-Bezier methods for the computer aided design of free-form curves and surfaces*,” Journal of the Association for Computing Machinery, Vol. 21, pp. 293-310, 1974.
- [24] Rogers, D.F., and Adams, J.A., “*Mathematical elements for computer graphics*”, 2<sup>nd</sup> Edition, McGraw-Hill, 1989.
- [25] Laurent P.J., Sablonnierre P., and Schumaker, L.L., “*Curve and surface design*”, 1<sup>st</sup> Edition, Vanderbilt University Press, 1999.
- [26] Farin, G., “*Curves and surfaces for computer aided geometric design*”, 4<sup>th</sup> Edition, Academic Press, 1997.
- [27] Wahba, G. “*Spline models for observational data*”, Society for Industrial and Applied Mathematics, Capital City Press, 1992.
- [28] Bookstein, F. L. "Principal warps: Thin Plate Splines and the decomposition of deformations." IEEE Transactions on Pattern Analysis and Machine Intelligence, Vol. 11, pp. 567-585, 1989.
- [29] Mischke, C.R., and Shigley, J.E., “*Mechanical Engineering Design*”, 6<sup>th</sup> Edition, Mc Graw-Hill, 2001.
- [30] Marin, J., “*Mechanical behavior of engineering materials*”, Prentice-Hall, 1962.
- [31] “*Fatigue design handbook*”, Society of Automotive Engineers, 1958.